OBSERVATIONS OF THREE BINARY X-RAY SOURCES: CYG X-1, CYG X-2, AND 4U1813+50 (AM HER)

Thesis by

William Charles Priedhorsky

In Partial Fulfillment of the Requirements

for the Degree of

Doctor of Philosophy

California Institute of Technology

Pasadena, California

1978

(Submitted 1977 December 20)

DEDICATION

To

My Parents,

Frank and Mary Lou Priedhorsky

and

To

My Wife and Daughter,

Barbara and Anna Beth

ACKNOWLEDGEMENTS

The contributions of many people made the flight of sounding rocket 26.038 possible. R. Rothschild, E. Boldt, S. Holt, P. Serlemitsos, C. Glasser, and F. Birsa of the Goddard Space Flight Center X-ray astrophysics group developed and built the payload, and advised on its modification and preparation for flight 26.038. W. Moore of Caltech freely contributed from his store of sounding rocket experience ideas for the modification of the payload. F. Cordova and I. Tuohy, also of Caltech, assisted in launch preparations at White Sands. The launch would not have been possible without the aid of the personnel of the Sounding Rocket Division of Goddard Space Flight Center. I would particularly wish to thank our long-suffering mission "mother", T. Collinson. S. Buchanan of Caltech, by the application of great patience and care, stretched polypropylene windows of exceptional quality. Special commendation must go to J. Meador, who as electrical engineer not only made the payload electronic systems perform flawlessly, but contributed long hours to the preparation of the whole payload from project initiation to launch.

I acknowledge helpful discussions of the rocket data with K. Thorne, S. Hatchett, M. Weisskopf, and F. Lamb. Analysis of the Cyg X-1 data was done in collaboration with G. Garmire, R. Rothschild, E. Boldt, S. Holt, and P. Serlemitsos.

I would like to thank my friend and colleague W. Krzeminski, who collaborated with me on the AM Her ground-based observations and analysis.

Our insight into that complex system was enhanced by discussions with D. Mikkelsen, J. Landstreet, S. Tapia, J. Ostriker, and P. Stockman.

My advisor G. Garmire provided advice and insight throughout my graduate career. At the same time, he allowed me sole responsibility for the flight of payload 26.038. The rocket project was thus a unique learning experience, sometimes arduous but always challenging.

My financial support came from Graduate Research Assistantships and a National Science Foundation Fellowship. Support for the research came from National Aeronautics and Space Administration grants NGL 05-002-207 and NGR 05-002-284 and National Science Foundation grant AST75-01398A01.

ABSTRACT

A large-area, rocket-borne pointed proportional counter observation of Cygnus X-1 was made to study its spectrum from 0.15 to 20 keV, and to investigate the possible energy dependence of its "shot-noise" variability. If the column density for X-ray absorption to Cyg X-1, N_X, is equal to the interstellar column density, N_H, deduced from the observed reddening E_{B-V} towards HD 226868, about half the flux in the band 0.6-1.5 keV is attributed to a steep low energy spectral component.

Data from this flight, and from two previous rocket experiments sensitive in the band 1.5 to 42 keV, showed no energy dependence in their "shot-noise" behavior. The ratio of the soft component of the spectrum to the flux from the power law region of the spectrum above 2 keV is constant through the shot noise variations. Autocorrelations of data from the three flights are consistent with an energy independent shot decay time. The fraction of time-averaged flux in the shots is less than 1, confirming the result of Sutherland, Weisskopf, and Kahn (1977). The lack of rounding of the auto-correlation at very small time delays indicates that the shots must have at least one sharp edge with characteristic time $\leq$ 0.01 second. Cross-correlation between flux in low and high energy bands suggests a time lag, in the sense that flux at high energies lags behind that at low energies, but is consistent with zero lag. Time-skewness calculations rule out a model of exponentially decaying shots. No millisecond bursts were seen in the 84 second observation.

An excess flux at low X-ray energies has been predicted by Comptonization models of the spectrum of Cyg X-1. The lack of spectral variability of the power-law spectrum through the shot noise variation is consistent with a Comptonized spectrum. The proportional variation of the excess soft flux sets some constraints on the origin of that flux in the context of models of Cyg X-1.

An observation of the X-ray source Cyg X-2 during the same flight yielded spectral and temporal data. The spectrum could be fit by optically thin bremsstrahlung with a temperature kT of 4.4 keV. An upper limit of 8% is set to the pulsed fraction of any periodic modulation with period P in the range 640 μsec < P < 10.24 sec. Cyg X-2 appears similar to other soft unpulsed galactic X-ray sources such as Sco X-1. We conclude from the lack of pulsations and the absence of any spectral structure at the iron K-edge that Cyg X-2 is not an intrinsically pulsed source (such as Her X-1) embedded in an optically thick scattering cloud.

Extensive optical multicolor photometric observations of the X-ray binary AM Her were made during the 1976 season. The data obtained suggest that the red component of the optical flux is closely related to the source of optical circular polarization in the system. We conclude from the periodic modulation of flux in the U through R bands, which is particularly well defined when plotted as color curves, that the primary and secondary minima are neither eclipses by a secondary star nor by a hot spot. We suggest that the primary minimum in the

visual light curve is the eclipse of a region of intense optical emission in the magnetic field near the surface of a degenerate dwarf by that dwarf itself.

TABLE OF CONTENTS

LIST OF FIGURES

Page

APPENDIX A

OBSERVATIONS OF THREE BINARY X-RAY SOURCES: CYG X-1, CYG X-2, and 4U1813+50 (AM HER)

INTRODUCTION

This thesis consists of three papers reporting observational studies of cosmic X-ray sources. The three sources appear to be compact objects in binary systems which produce X-rays by the liberation of gravitational energy from accreted matter. Each of the end-products of stellar evolution may be represented in this set of objects: AM Her contains a white dwarf, Cyg X-2 may contain a neutron star, and Cyg X-1 contains the leading candidate for a black hole. The observational studies reported in this thesis were conducted to study the accretion process near these compact objects.

Although the discovery of Sco X-1, the first detected X-ray source other than the sun, took place in 1962 (Giacconi et al. 1962), ten years elapsed before the first identification of an X-ray source (Cen X-3) as a member of a binary system (Schreier et al. 1972). Despite this lag in observational verification, it was not surprising that a compact object in a binary system might emit X-rays. A hydrogen atom falling onto the surface of a one solar mass white dwarf ($r \sim 10^9$ cm) or neutron star ($r \sim 10^6$ cm), or to the event horizon of a black hole ($r \sim 10^5$ cm) releases a gravitational potential energy of about 10^2, 10^5, or 10^6 keV respectively. It is thus not difficult for matter accreted onto a compact object to attain temperatures high enough that

it radiates in the X-ray band. If such a compact object is located in a binary system, where it can accrete matter lost to the secondary star by a stellar wind or Roche lobe overflow, a luminous X-ray source may be created.

Proportional detectors sensitive to X-rays in the band 0.1-50 keV are not difficult to construct. They are sensitive, with an efficiency approaching 100%, to individual X-ray photons. Since the brightest X-ray sources produce fluxes at the earth greater than 1 photon cm^{-2} sec^{-1}, a detector of rather modest dimensions can make observations of high statistical significance. The birth of X-ray astronomy, however, was delayed until the space age by the fact that X-rays in the kilovolt band are absorbed at altitudes below 100 km. Though observations at energies above 20 keV can be made from high-flying balloons, X-ray detectors sensitive to flux below 20 keV, where most of the energy from observed sources is emitted, must be flown in a rocket or satellite vehicle. This thesis reports X-ray observations of two binary sources made in a rocket experiment.

Cyg X-1 is a bright X-ray source in the constellation Cygnus located 3° from the galactic plane. It has been identified with HD226868, a ninth magnitude OB supergiant. Spectroscopic observations indicate that HD226868 is a single line spectroscopic binary, and that the mass of the (optically) invisible secondary is greater than the theoretical upper limits for white dwarf or neutron star masses. If we identify the unseen secondary with the X-ray source, and assume that the X-rays are produced by mass accretion onto a compact object, we conclude that

the X-ray source must be a black hole. Current theoretical models show that the observed X-ray spectrum can be produced by emission from the inner part of an accretion disk about a black hole.

The X-ray flux from Cyg X-1 shows an apparently chaotic variation on a time scale of seconds. Though a hard power-law spectrum is observed from 2 keV < E < 100 keV, spectral data seem to indicate an additional component at lower energies. In Chapter 1, a proportional counter observation of the rapid "shot" variability of the flux in the low energy component and at higher energies is reported. We analyze the nature of the variability in the context of accretion disk models of Cyg X-1.

During the same rocket flight, an observation was made of Cyg X-2, a bright galactic X-ray source which appears to be typical of the rather bland class of unpulsed X-ray sources with soft spectra. In Chapter 2 we examine whether the observed X-ray spectrum and lack of pulsations are consistent with pulsed X-ray emission from a rotating neutron star, such as in the Her X-1 system, but masked by a cloud of matter optically thick to electron scattering.

Because of the cost of space experimentation, it is desirable to make maximum use of observations which can be made from the ground. For the six-figure price of a five-minute rocket flight, a medium-sized ground-based facility can be constructed which will last for decades. The variable star AM Her is an example of an X-ray system from which a great deal of data can be gathered via ground-based observations.

X-ray observations by the soft X-ray experiment on the SAS-C satellite indicated that AM Her was a likely candidate for the optical

counterpart of an X-ray source prominent in the 1/4 keV band (which later proved to be coincident with the 2-6 keV source 4U1813+50) (Hearn, Richardson, and Clark 1976). The suggestion that it was an X-ray source led us to the extensive photometric observations of AM Her reported in Chapter 3. Tapia (1976) discovered strong circular polarization in the optical band, which indicated that the primary (X-ray source) component of the AM Her system was a magnetized white dwarf. We suggest that the main part of the optical emission observed photometrically is cyclotron emission in the strong ($B \sim 10^8$ gauss) magnetic field near the surface of the white dwarf. If this interpretation is proved correct, studies of the optical variation of AM Her may serve as a probe of the accretion process near the X-ray source. AM Her would thus be unique in the class of X-ray sources, for optical emission from other sources is not dominated by flux from the vicinity of the compact object.

CHAPTER 1

EXTENDED BANDWIDTH X-RAY OBSERVATIONS OF CYGNUS X-1

I. INTRODUCTION

X-ray flux from the black hole candidate Cyg X-1 is characterized by variability on time scales which range from months to $\leqslant$ seconds (cf. Boldt et al. 1975). The long term changes involve profound variability of the X-ray spectrum. Observations can be classified, to first order, into high and low intensity states of flux in the band 2-6 keV. The high state shows a steep variable spectrum which may be characterized by a photon power law index α (where $dN/dE \sim E^{-\alpha}$) in the range $2 < \alpha \leqslant 5$ for $2 < E < 10$ keV (Schreier et al. 1971, Canizares and Oda 1977). The low state spectrum is flatter, with α in the range $1.4 < \alpha < 1.9$, and fits a single power law for the band $2 < E < 100$ keV (Rothschild et al. 1977, Canizares and Oda 1977, Matteson et al. 1975). High state spectra sometimes include a flat component reminiscent of the low state at $E < 10$ keV, but have at other times been observed to follow the steep power law to 100 keV (Matteson et al. 1975). UHURU observations by Oda et al. (1971) showed chaotic temporal variation on a time scale of seconds from Cyg X-1. Terrell (1972) showed that the variation could be modeled by a random shot-noise process. Rothschild et al. (1974) and Oda et al. (1974) have reported even more rapid variations on a 1 millisecond time scale.

Although the long-term variations of Cyg X-1 involve major spectral changes, the energy dependence of the shot-noise variability on a time scale $\sim$ seconds, particularly during the low state, is uncertain. Weisskopf, Kahn, and Sutherland (1975) and Rothschild et al. (1977)

report low state observations consistent with energy independence of the shot-noise variability. Oda et al. (1976) suggest that shots are suppressed at low energies during the high state but have the same relative amplitude at all energies during the low state. Canizares and Oda (1977) report a low state observation showing no average hardening or softening of the flux in shot-noise flares.

The purpose of this paper is to report an energy- and time-resolved observation of Cyg X-1, sensitive from 0.15-20 keV, undertaken in order to investigate the behavior of the flux at low X-ray energies. Data in the band 1.5-42 keV taken in two previous rocket flights (Rothschild et al. 1977) have also been reanalyzed to search for any energy dependence of the time signature.

It has been suggested (Garmire and Ryter 1975, Gorenstein 1976) that a steep component of the spectrum exists at energies $\leqslant$ 2 keV in the low state of Cyg X-1. That component may be related to the steep spectrum observed at E > 2 keV in the high state. Because of the poor energy resolution of proportional counter detectors at low energies, that component could mimic an anomalously low value of interstellar absorption.

The inferred X-ray luminosity of Cyg X-1 in the band $\leqslant$ 2 keV depends strongly on the interstellar photoelectric absorption assumed to the source. There is good reason to believe that the interstellar column density N_H in the direction of Cyg X-1 is 7×10^{21} cm^{-2}. Gorenstein (1975) and Ryter, Cesarsky, and Audouze (1975) have independently shown that there exists a proportional relationship between N_x (the column density of gas with Brown and Gould abundances required to fit the low

energy absorption of an X-ray source) and visual reddening for optically thin X-ray sources (which would be expected to show no internal absorption so that $N_x = N_H$). Ryter, Cesarsky and Audouze find $N_x/E_{B-V} = (6.8 \pm 1.6) \times 10^{21}$ cm^{-2} while Gorenstein finds $N_x = 2.22 \times 10^{21}$ cm^{-2} A_v, which, for $R = A_v/E_{B-V} = 3.1$, implies $N_x/E_{B-V} = 6.9 \times 10^{21}$ cm^{-2}. The extimated statistical and systematic error in this relationship is less than 25 percent. The validity of the N_x/E_{B-V} relationship is supported by the fact that for most binary sources (which may contain internal absorbing matter) the X-ray absorption N_x is greater than that expected from E_{B-V} (see Gorenstein 1975). Cyg X-1 is exceptional among binary sources if it shows N_x smaller than the N_H implied by reddening.

The reddening E_{B-V} to Cyg X-1 measured by ground-based optical observations is 1.1 mag (Margon, Bowyer, and Stone 1973; Bregman et al. 1973). Vacuum ultraviolet measurements by the ANS satellite indicate $E_{B-V} = 1.02$ for $R = 3.1$ (Wu, Van Duinen, and Hammerschlag-Hensberge 1975). Garmire and Ryter (1975) and Gorenstein (1976) conclude from these considerations that $N_H = 7 \times 10^{21}$ cm^{-2} in the direction of Cyg X-1.

The column density N_x determined in an X-ray observation is found by folding a distribution $dN/dE = C\ F(E)e^{-\sigma(E)N_x}$ through the detector response and fitting to the measured energy spectrum. $F(E)$ is a spectral form (power law, bremsstrahlung, etc.) while $e^{-\sigma(E)N_x}$ is the energy dependent absorption term, important only at the low end of the spectrum, (e.g., $\sigma(E)N_x \approx (E/1.2\ \text{keV})^{-8/3}$ for $N_x = 7 \times 10^{21}$ cm^{-2}).

Ideally, a source with no intrinsic photoelectric absorption will show $N_x = N_H$. However, an accurate estimate of N_x is only possible if the intrinsic spectrum F(E) can be correctly extrapolated to the low energy region. The energy resolution of proportional counters (at best ~ 30 percent at 1.5 keV) is insufficient to distinguish a break in the unabsorbed spectrum F(E) from an absorption effect, so that an effective $N_x \neq N_H$ is measured. If we know the interstellar value of N_H, as we have reason to believe for Cyg X-1, the measured column density N_x indicates an excess of flux at low energies with respect to F(E) if $N_x < N_H$ or a deficiency (possibly caused by circumstellar absorption if $N_x > N_H$.

Previous experiments have produced a range of values of N_x for Cyg X-1. Events of anomalously high absorption, with $N_x \leqslant 5 \times 10^{22}$ cm^{-2}, seem to be associated with gas streams within the system (Parsignault et al. 1975). At other times, N_x has been measured in the range 1.5×10^{21} cm^{-2} to 7×10^{21} cm^{-3} in both low and high states (Seward et al. 1972, Li and Clark 1974, Gursky et al. 1971, Stevens, Garmire, and Riegler 1972, Heise et al. 1975, Saba, private communication). The variability of N_x might be produced by a variable low energy excess.

Models to explain the hard (E > 2 keV) low-state X-ray spectrum of Cyg X-1 suggest the existence of a steep low energy component which, depending on its energy and flux, may or may not be observable from the earth because of low energy interstellar absorption. It is suggested that the hard power law spectrum observed at E > 2 keV results from

Comptonization of soft photons (E > 50 eV) in a marginally optically thin ($\tau \sim 1$), hot electron gas ($T_e \sim 10^9$ K) (Thorne and Price 1975; Coe, Engel, and Quenby 1976; Shapiro, Lightman, and Eardley 1976 (henceforth SLE); Eardley and Lightman 1976). Bremsstrahlung photons produced in the hot gas are insufficient to produce the observed Comptonized spectrum, hence another copious source of soft photons is required. That source may be optically thick thermal cyclotron radiation of maximum energy $E_s \lesssim 5$ eV in the hot cloud (Eardley and Lightman 1976), soft X-rays from a cooler region of the accretion disk surrounding the hot inner cloud, or radiation from high-density, low temperature regions within the hot gas. Eardley and Lightman (1976) suggest that the soft photon source which feeds the Comptonized spectrum during the low state increases in intensity during the high state to produce the steep high state spectrum in the region 2-10 keV.

This investigation was undertaken to attempt to detect the low energy component of the spectrum of Cyg X-1, and to compare its time variation to that of higher energy flux. The large flux and rapid variability of Cyg X-1 allow us to compare the temporal behavior of this source in different energy bands during a brief (in this case, 84 seconds) rocket exposure. Possibly one may be able to conclude from the behavior of a low energy excess something about the origin of the source photons for the power law spectrum.

In the remainder of this paper, we assume that the true column density N_H is 7×10^{21} cm^{-2}. Any smaller measured N_x thus implies a low-energy excess in the source.

II. EXPERIMENT DESCRIPTION

An X-ray astronomy payload prototypical of the Goddard-Caltech-Berkeley-JPL HEAO A-2 experiment was launched by an Aerobee 200 vehicle (flight 26.038) from White Sands Missile Range at 0855 UT 1976 May 11. The payload was that described by Rothschild et al. (1974) with the following modifications. The previously used xenon detector was converted into a propane counter with a thin polypropylene window coated with carbon for a total thickness of 130 $\mu g\ cm^{-2}$, and was regulated at 20 cm Hg absolute pressure during the flight. A new slat collimator was used with a 3° x 3° (FWHM) field of view and 510 cm^2 maximum effective area. This low energy detector (LED) was sensitive to X-rays in the range 0.15-3 keV. The previously used argon detector was fitted with an 870 $\mu g\ cm^{-2}$ aluminized mylar window, a similar 3° x 3° (FWHM) collimator with 550 cm^2 effective area, and a gas flow system that was sealed at launch with an absolute pressure of 83.6 cm Hg. This medium energy detector (MED) was sensitive to X-rays from 0.8 to 20 keV.

The attitude of the rocket was controlled by a STRAP-IV (Shrewsberry et al. 1973) pointing system. The pointing program consisted of attitude reference updates on two bright stars, a 20-second exposure to Cyg X-2, 8 seconds of sky containing no known sources, and 150 seconds of exposure to Cyg X-1. The detector system pointed to within 25' of Cyg X-1 during its exposure and the total drift was less than 5'. Hence, aspect-induced modulation of the signal was not significant. Pointing error and misalignment of collimator panels reduced the effective area exposed to

Cyg X-1 to 429 and 500 cm^2 respectively for the LED and MED.

High voltage breakdown in the second of five layers in the MED commenced 88 seconds into the Cyg X-1 exposure. Consequently, only the first 85 seconds of data are used in the subsequent analysis.

III. DATA AND SPECTRAL ANALYSIS

No statistically significant flux above background was detected in the 0.15-0.28 keV band during the exposure to Cyg X-1. Figure 1 shows the combined counting rate for X-rays in three broad energy bins (0.6-1.5 keV, 1.5-3.0 keV, and 3.0-20 keV) from both detectors for the 85 second span of useful Cyg X-1 data. The apparent temporal variability characteristic of Cyg X-1 is far in excess of statistical variation, and indeed is one of the distinguishing features of Cyg X-1. Data obtained from Cyg X-2 during the same flight are consistent with Poisson statistics for a constant source.

Pulse height information for each X-ray event was digitized into 128 equally spaced energy channels which spanned 0.15-3.5 keV for the LED and 0.8-24 keV for the MED. Data from the Cyg X-1 exposure were summed and corrected for background to form raw source spectra for each detector. An independent spectral analysis of the data from each detector was made.

The MED data were fit to a spectrum of the form

$$\frac{dN}{dE} = I_o E^{-\alpha} e^{-N_x \sigma(E)} \text{ photons/cm}^{-2} \text{ sec}^{-1} \text{ keV}^{-1} ,$$

Figure 1

Counting rate obtained during May 1976 Cyg X-1 pointed observation for 0.6-1.5 keV, 1.5-3.0 keV, and 3.0-6.0 keV. A non-source background of 4.2, 2.0, and 1.8 cts/0.1024 second has not been subtracted.

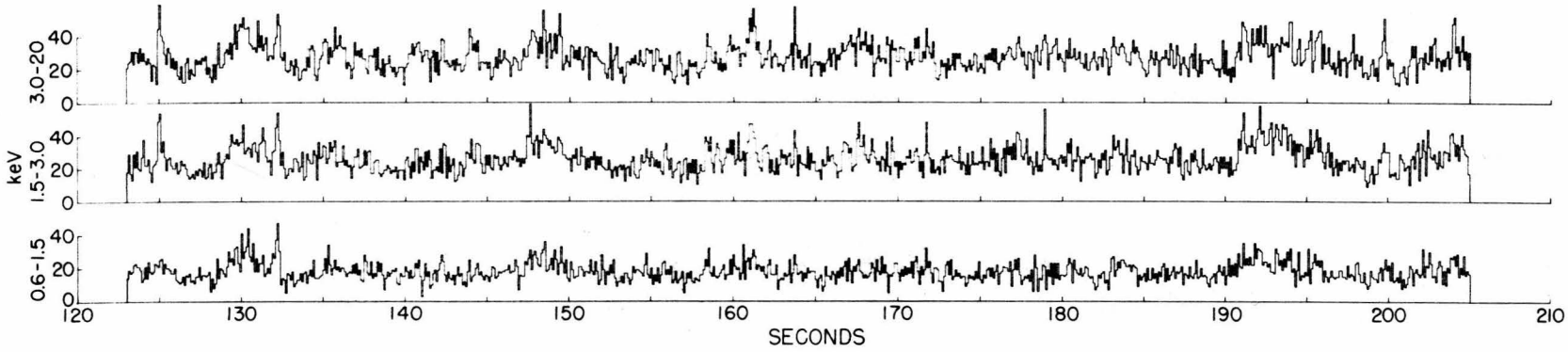
keV
3.0-20
1.5-3.0
0.6-1.5
40
20
0
120
130
140
150
160
170
180
190
200
210
SECONDS

Figure 1

where $\sigma(E)$ is the interstellar absorption cross section of Brown and Gould (1970). For the MED spectrum, the power law index α, X-ray absorption N_x, and intensity I_o were free parameters. Best fit (reduced $\chi^2 = 1.22$ for 103 d.o.f.) parameters were $I_o = 1.22 \pm 0.15$, $\alpha = 1.40 \pm 0.07$, $N_x = 2.4 \pm 1.2 \times 10^{21}$ cm^{-2} (90 percent confidence errors derived from increase in χ^2 of 6.25) (Lampton, Margon, and Bowyer 1976). The smaller number of independent spectral points measured by the LED prevent the accurate determination of α and N_x at the same time. Instead, I_o and α were constrained to the values determined by the argon detector, then from the LED data, N_x was found to be $3.4 \pm 0.9 \times 10^{21}$ cm^2 (90 percent level of confidence, including errors in argon detector spectrum, error in the area ratio of the two counters, and statistical errors). Values of N_x measured by both detectors are in agreement and are significantly less than the assumed N_H. This indicates an excess flux at low energy. Figure 2 shows an incident spectrum of $\alpha = 1.40$ and $N_x = 7.0 \times 10^{21}$ cm^{-2}, that spectrum folded through the response of the two detectors, and the two observed source spectra. Note the excess in observed flux below $\sim$ 2 keV for both detectors.

In order to estimate the shape of the low energy excess, the best fit single power law spectrum with N_x constrained to 7.0×10^{21} cm^{-2}, folded through the detector response function, was subtracted from the observed spectrum. The residual flux was then fit to a spectral form (again with $N_x = 7 \times 10^{21}$ cm^{-2}). Best power law fits for the excess low energy flux were $I_o = 2.15 \pm 0.3$ cts cm^{-2} sec^{-1} keV^{-1}

Figure 2

Spectrum of Cyg X-1 obtained during May 1976 observation. The solid line is an incident spectrum of the form $dN/dE = E^{-\alpha}\ e^{-\sigma(E)N_x}$ photons $cm^{-2}\ sec^{-1}\ keV^{-1}$, with $\alpha = 1.40$ (the best fit value from MED data) but N_x constrained to the best estimate of interstellar column density, $7.0 \times 10^{21}\ cm^{-2}$. Dashed curves are the resultant raw spectra expected in the two detectors. The points shown are the actual background corrected spectra. Note the excess flux at low energies.

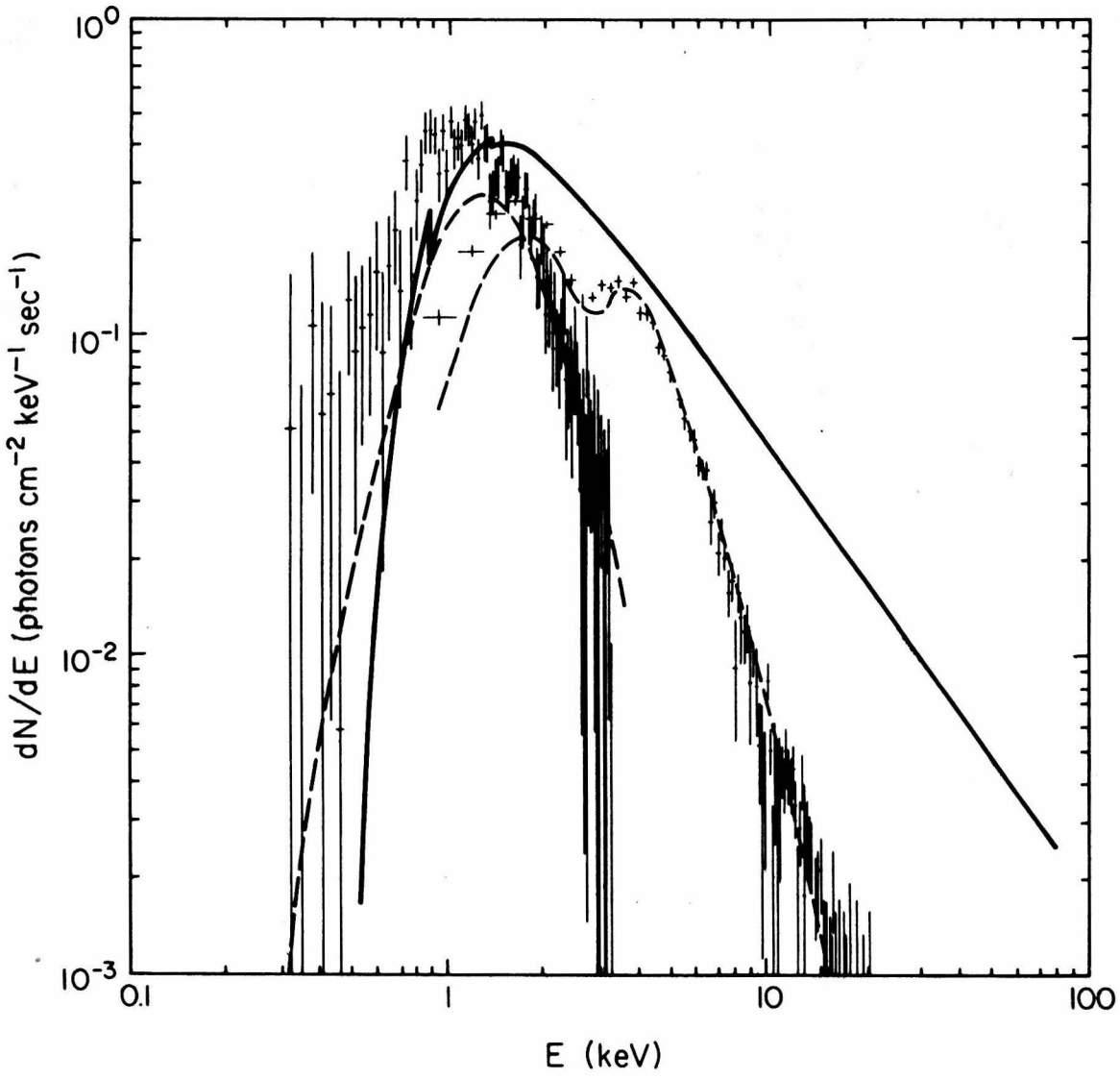

Figure 2

$\alpha = 5.1 \pm 0.4$ for the LED data, and $I_o = 2.6 \pm 0.4$ cts cm^{-2} sec^{-1} keV^{-1}, $\alpha = 4.8 \pm 0.5$ for the MED data (all errors are 90 percent confidence level). The LED and the MED excess could also be fit to a thermal spectrum $dN/dE = I_o e^{-E/kT} e^{-N_x \sigma(E)}$ with kT = 0.29 ± 0.07 keV and 0.35 0.13 keV respectively (I_o for a thermal fit is strongly dependent on the chosen value of kT, as the observed spectral data is from a steeply falling portion of the spectrum). For the LED and MED, I_o is in the range 70 ± 60 and 25 ± 10 cts cm^{-2} sec^{-1} keV respectively. The low energy excess thus represents a very steep spectral component. It does fall within the upper portion of the range of spectral index ($2.6 < \alpha \leq 5.1$) seen by UHURU (Schreier et al. (1971)) at E > 2 keV when Cyg X-1 was in the "high" state. It must be noted that the existence of a low energy excess depends on the assumption of $N_H = 7.0 \times 10^{21}$ cm^{-2}. A single component power law spectrum with $N_H = N_x \approx 3 \times 10^{21}$ cm^{-2} is also consistent with the data.

If we assume $N_H = 7 \times 10^{21}$ cm^{-2}, we can calculate the amount of the observed flux at low energy that is associated with the soft excess. In the energy bands 0.6-1.0 keV and 0.6-1.5 keV, approximately 60 and 40 percent respectively of the observed photons are in excess of those expected. The low energy excess flux forms only 9 percent of the total observed photon flux.

The temporal behavior of the low and high energy flux is analyzed in the next section.

IV. TEMPORAL ANALYSIS

a) Hardness Ratio

A hardness ratio $R_i \equiv s_{i,TOT}/s_{i,LO}$ was calculated to examine if there was any variation of ratio of the low energy flux to the rest of the flux on the time scale of the shot noise variability. $s_{i,TOT}$ and $s_{i,LO}$ are the counts (corrected for background) during bin number i in the energy ranges 0.6-20 keV and 0.6-1.0 keV. Using 82 1.024 second time bins, or rebinning into 820 0.1024 second bins, R showed a scatter that was consistent with Poisson counting statistics and a constant value of R. Thus no observable energy dependence of temporal behavior on a time scale 1-0.1 seconds was noted.

In order to search with good sensitivity for a systematic trend of hardness with intensity, the 0.1024 second bins were sorted into several intensity steps. The number of counts in a bin ranged from 31 to 154, after subtracting a nonsource background of ~ 8 cts/bin. The mean hardness R for each intensity step was then calculated (see Figure 3). It can be seen that there is no systematic trend of hardness with intensity. The data are consistent with a constant R (χ^2 = 12.68 for 11 d.o.f.) and constrain the slope a_1 of a linear relation $R = a_1 s_{TOT} + a_o$ to $-0.012 \pm .027$ (90 percent confidence). Note that if s_{LO} was constant, R would show the linear relation $R = (1/s_{LO})\, s_{TOT}$, so for $s_{LO} = \overline{s_{LO}} = 4.4$ cts/bin, $a_1 = 0.23$. Hence, s_{LO} is not constant and it is apparent that the rapid variations seen in Cyg X-1 occur with equal amplitude across the energy response of this experiment.

Figure 3

Hardness ratio $R \equiv \frac{s_{TOT}}{s_{LO}}$ versus observed intensity, s_{TOT}, where the channels LO and TOT are 0.6-1.0 keV and 0.6-20 keV. All 0.1024 second bins falling in the intensity step s_{TOT}-5 cts/bin to s_{TOT}+5 cts/bin are averaged to obtain a mean hardness for that step.

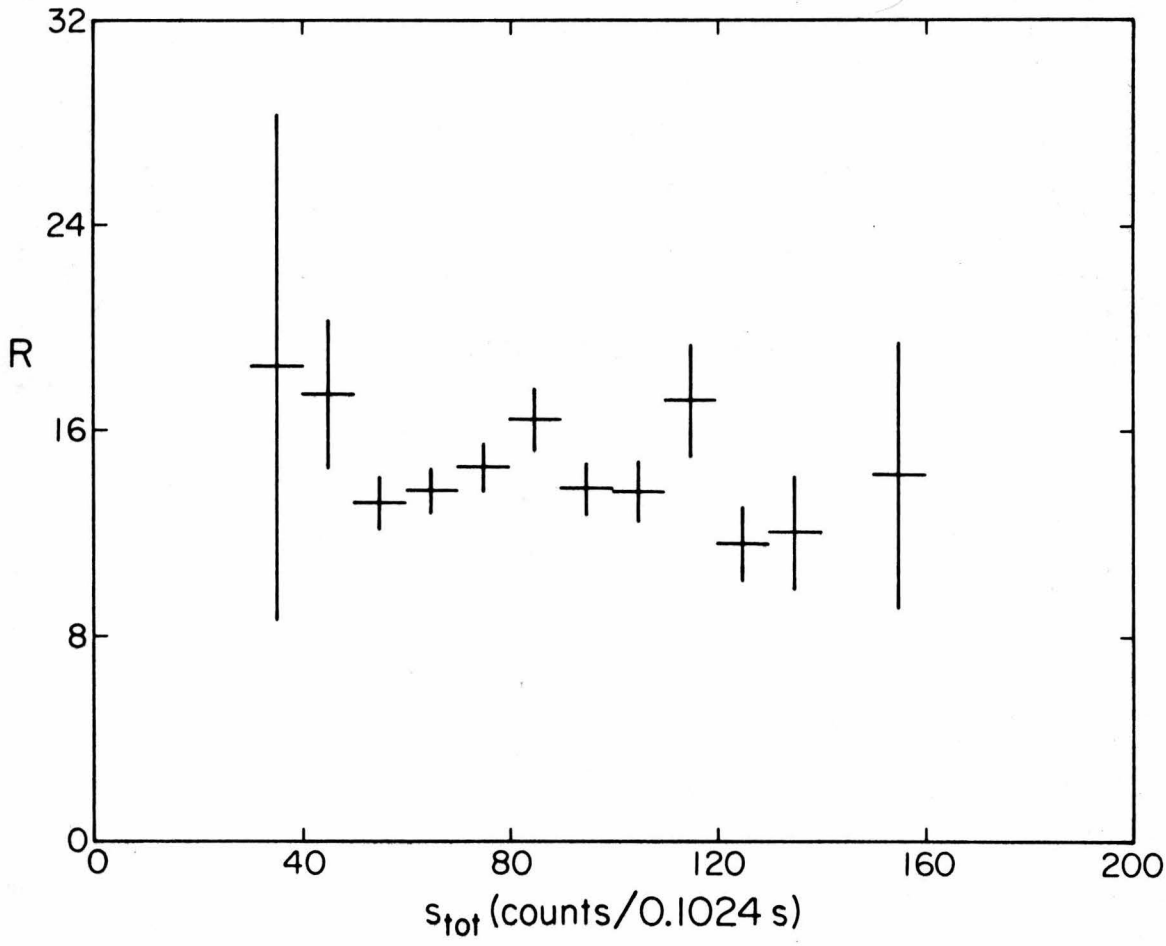

Figure 3

In order to further characterize the short-term time variability of the source, a shot-noise analysis similar to that of Sutherland, Weisskopf, and Khan (1977, henceforth SWK) was performed on the data. This analysis was done for each of several broad energy bins to check for energy dependence of the shot-noise parameters.

b) Autocorrelations

Autocorrelation functions were used to determine the coherence time of the shots. The partially unbiased autocorrelation $\tilde{\rho}_u$ as defined by SWK (1977) was calculated for each of four 20.99 second segments of the data:

$$\tilde{\rho}_u = \frac{\tilde{R}_{u'}}{\tilde{R}_o} \qquad (1)$$

$$\tilde{R}_{u'} = \frac{1}{N} \sum_{i=1}^{(N-u)} (s_i - \bar{s})(s_{i+u} - \bar{s}) + \frac{(N-u)}{N^2(N-1)} \sum_{i=1}^{N} (s_i - \bar{s})^2 .$$

The array s_i is the counting rate summed into N bins, the autocorrelation delay u is in integer bins, $\bar{s}$ is the mean counting rate, and the data were summed into 0.1024 second bins. The four values determined for each point of the autocorrelation ρ_u were averaged to determine a value and estimated error. Autocorrelations for the energy bins 0.6-1.5 keV, 1.5-3.0 keV, 3.0-6.0 keV, and 6.0-20 keV are shown in Figure 4. The first twenty points (excluding u = 0) of each autocorrelation were fit to the

Figure 4

Mean autocorrelations for May 1976 Cyg X-1 data in the energy bins 0.6-1.5 keV (a), 1.5-3.0 keV (b), 3.0-6.0 keV (c), and 6.0-20.0 keV (d). Delay τ is in units of 0.1024 seconds. Errors are 1σ errors estimated from scatter of the autocorrelations calculated from four 20.99 second data sets. Also shown is the best fit autocorrelation (equation [1]) expected for exponential shots.

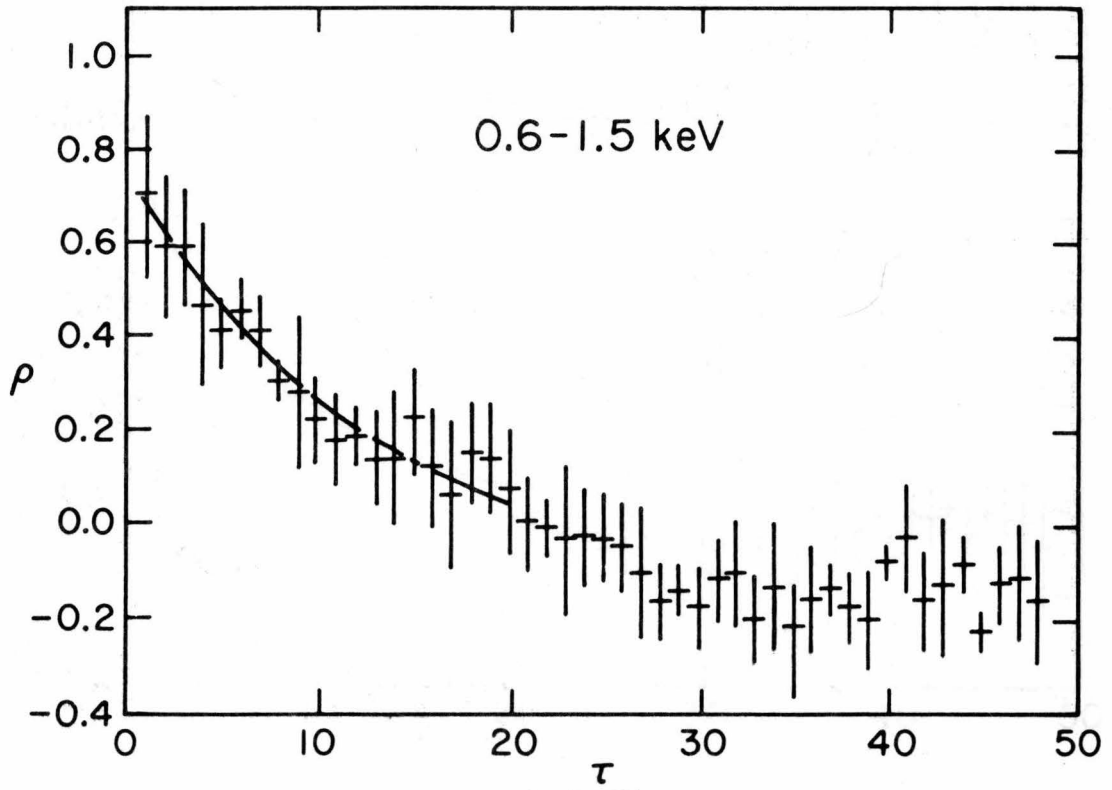
0.6-1.5 keV
ρ
τ
1.0
0.8
0.6
0.4
0.2
0.0
-0.2
-0.4
0
10
20
30
40
50

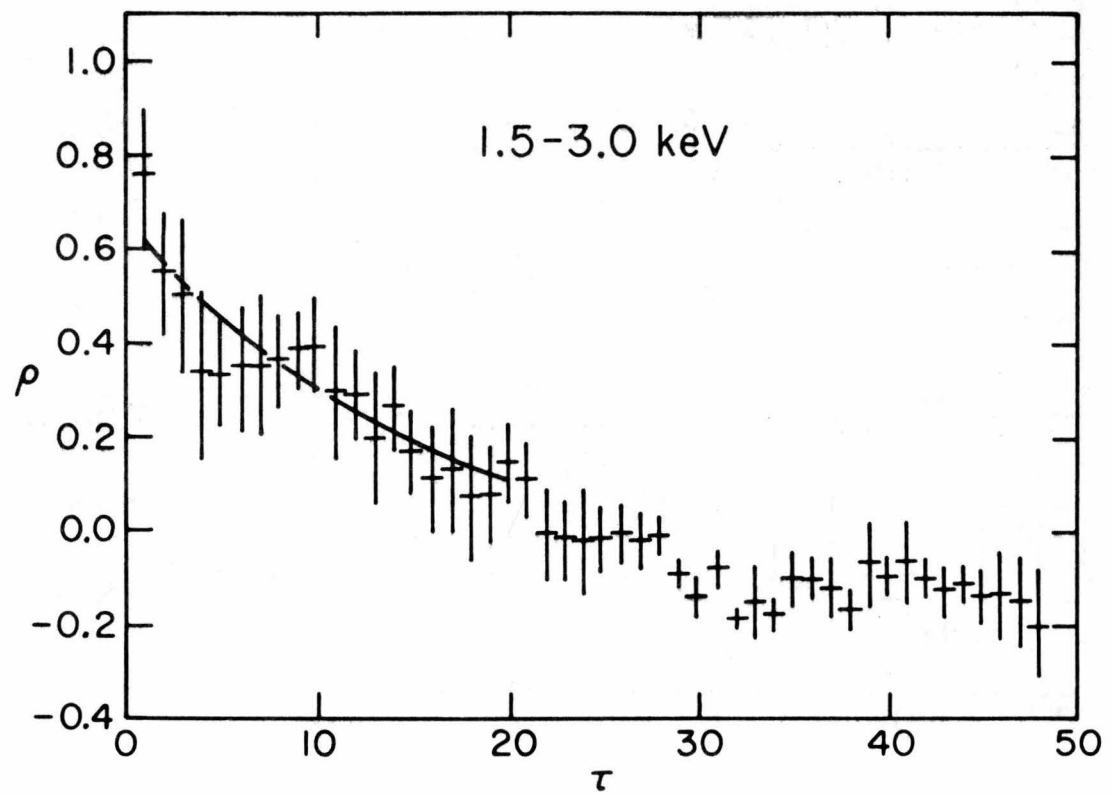
1.5-3.0 keV
ρ
τ
1.0
0.8
0.6
0.4
0.2
0.0
-0.2
-0.4
0
10
20
30
40
50

Figure 4 a&b

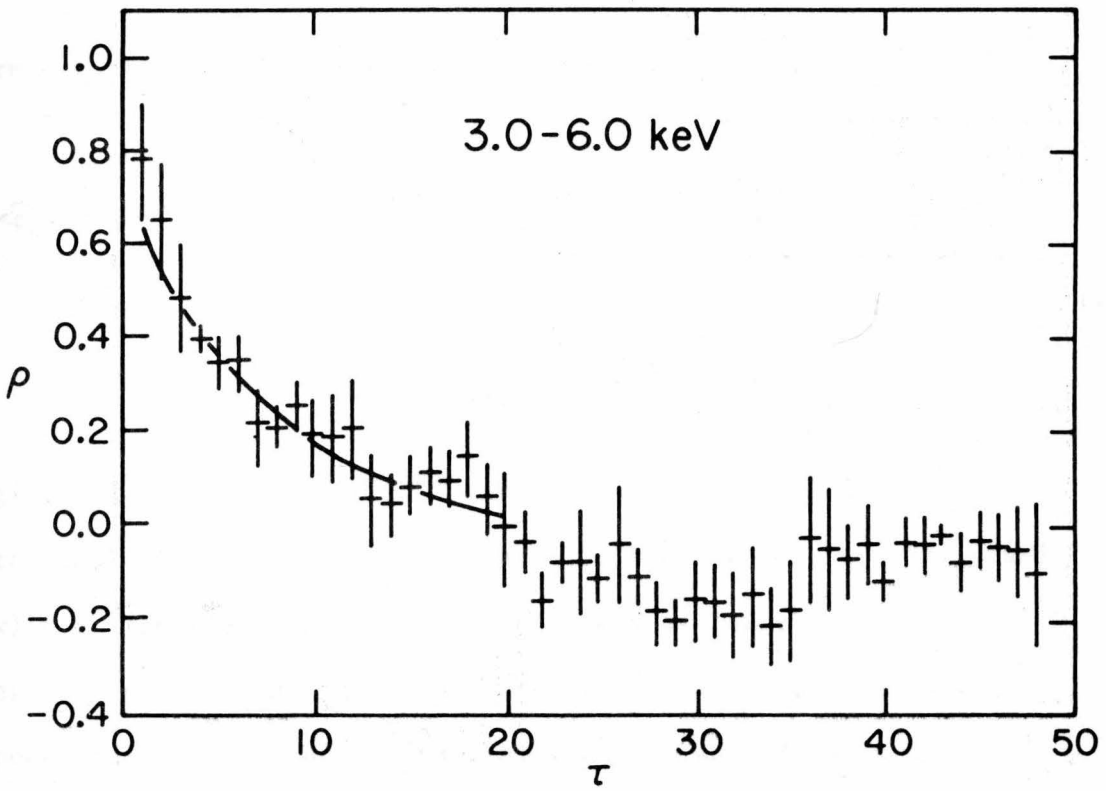
3.0-6.0 keV
1.0
0.8
0.6
0.4
0.2
0.0
-0.2
-0.4
ρ
0
10
20
30
40
50
τ

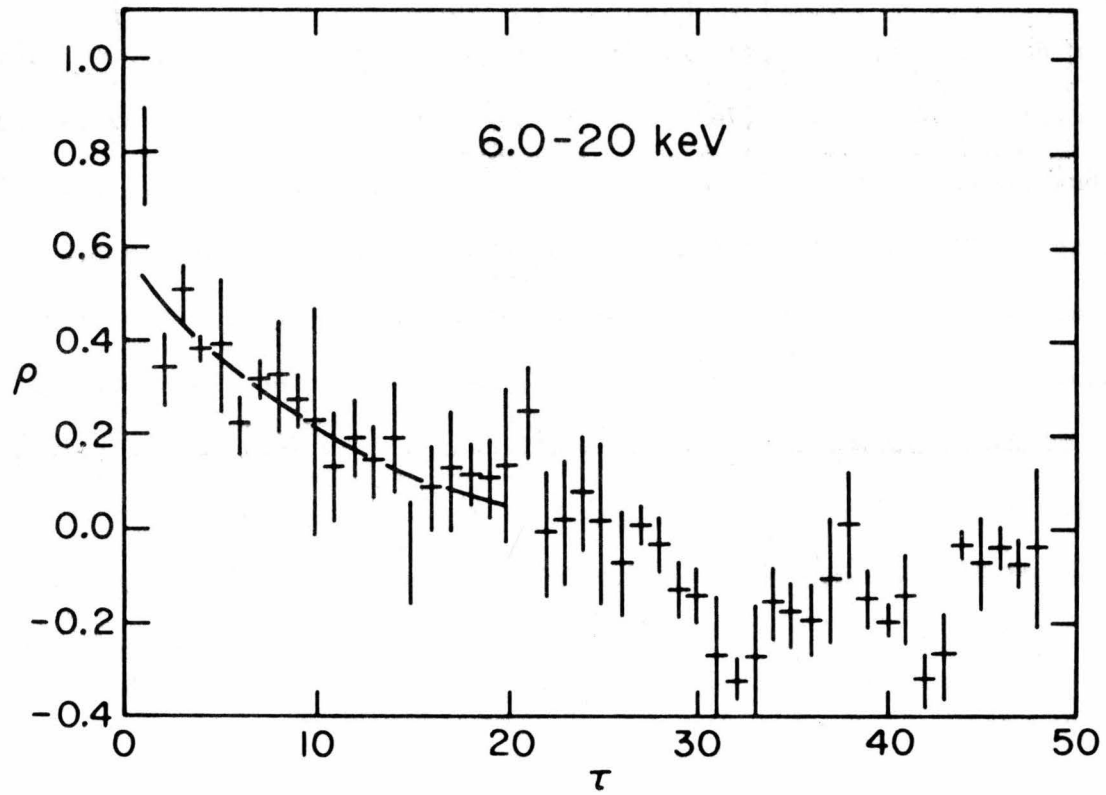
6.0-20 keV
1.0
0.8
0.6
0.4
0.2
0.0
-0.2
-0.4
ρ
0
10
20
30
40
50
τ

Figure 4 c&d

form expected for random exponential shots of decay time τ_o:

$$\langle \tilde{\rho}_u \rangle = C \frac{(N-u)}{N} \left[\frac{e^{-(u-1)x} g(x)}{2} - \frac{1}{(N-u)} \left[1 - \frac{1}{Ng(x)} \right] \left[1 + \frac{1}{N} \frac{(N-u)}{(N-1)} \right] + \frac{1}{N(N-u)} \left(u - \frac{1-e^{-ux}}{g(x)} \right) \right] \quad (2)$$

neglecting terms of order e^{-Nx} and $1/N^3$. N is the number of bins in a data sample, T is the bin width (here 0.1024 second), $x = T/\tau_o$, and $g(x) = e^{-x}(1-e^{-x})$. Note that in the limit of large N, $\langle \tilde{\rho}_u \rangle = e^{-\tau/\tau_o}$, where $\tau = uT$, so that the autocorrelation of a signal consisting of exponential shots is an exponential with the same decay time.

The best fit curves to the autocorrelations are also shown in Figure 4. Decay times τ_o for the four energy bins and for the combined data are respectively 1.2 ± 0.5 sec (0.6-1.5 keV), 1.8 ± 1.0 sec (1.5-3.0 keV), 1.0 ± 0.4 sec (3.0-6.0 keV), 1.3 ± 0.6 sec (6.0-20 keV), and 1.2 ± 0.6 sec (all photons E > 0.6 keV)(all errors are 1σ). This result is consistent with decay time independent of energy. The best fit autocorrelations fall below 1 at u = 0, even though the u = 0 term has been corrected to first order for counting statistics. This may indicate that the autocorrelation falls more steeply than exponentially at small time delay, so that an exponential is not the best possible fit to the autocorrelation.

c) High Time Resolution Autocorrelations

An autocorrelation of scaler data, which summed all X-ray events in the two detectors, was performed with time bins of 1.28 ms to examine the behavior of the autocorrelation at very small delay times. Data from a previous flight of the payload were similarly analyzed. The experiment configuration during two previous flights, October 1973 and October 1974, included one sealed detector filled with argon-methane and one with a xenon-methane mixture. Windows for both detectors were 1 mil aluminized Mylar, so that the energy response was shifted to higher energies in the earlier flights (Rothschild et al. 1977).

The two "fast" autocorrelations are shown in Figure 5. There is no evidence of an upturn at small time delay which might indicate time structure faster than that of the shot noise, such as millisecond bursts. Such an upturn may not be expected from the suggested millisecond bursts because of the low burst rate, $\sim 0.06\ \mathrm{sec}^{-1}$ (Rothschild et al. 1977), but the lack of an upturn argues against the existence of a large population of millisecond bursts too small to be individually detectable. The lack of a downturn of the autocorrelation at small time delay also tells something about the shape of the shots. It can be shown that for any function f(t), the autocorrelation $\rho(\tau)$ can be expanded in a Taylor series about $\tau = 0$,

$$\rho(\tau) = \frac{1}{\int_{-\infty}^{\infty} f^2(t)dt}\left(\int_{-\infty}^{\infty} f^2(t)dt - \tau \int_{-\infty}^{\infty} f(t)f'(t)dt - \frac{1}{2}\tau^2 \int_{-\infty}^{\infty} f(t)f''(t)dt + O(\tau^3)\right);$$

Figure 5

(a) Autocorrelation function for May 1976 (flight 26.038) data calculated from scaler data in 1.28 ms bins. (b) Same for data from flight 26.037 (October 1974). Errors are 1σ.

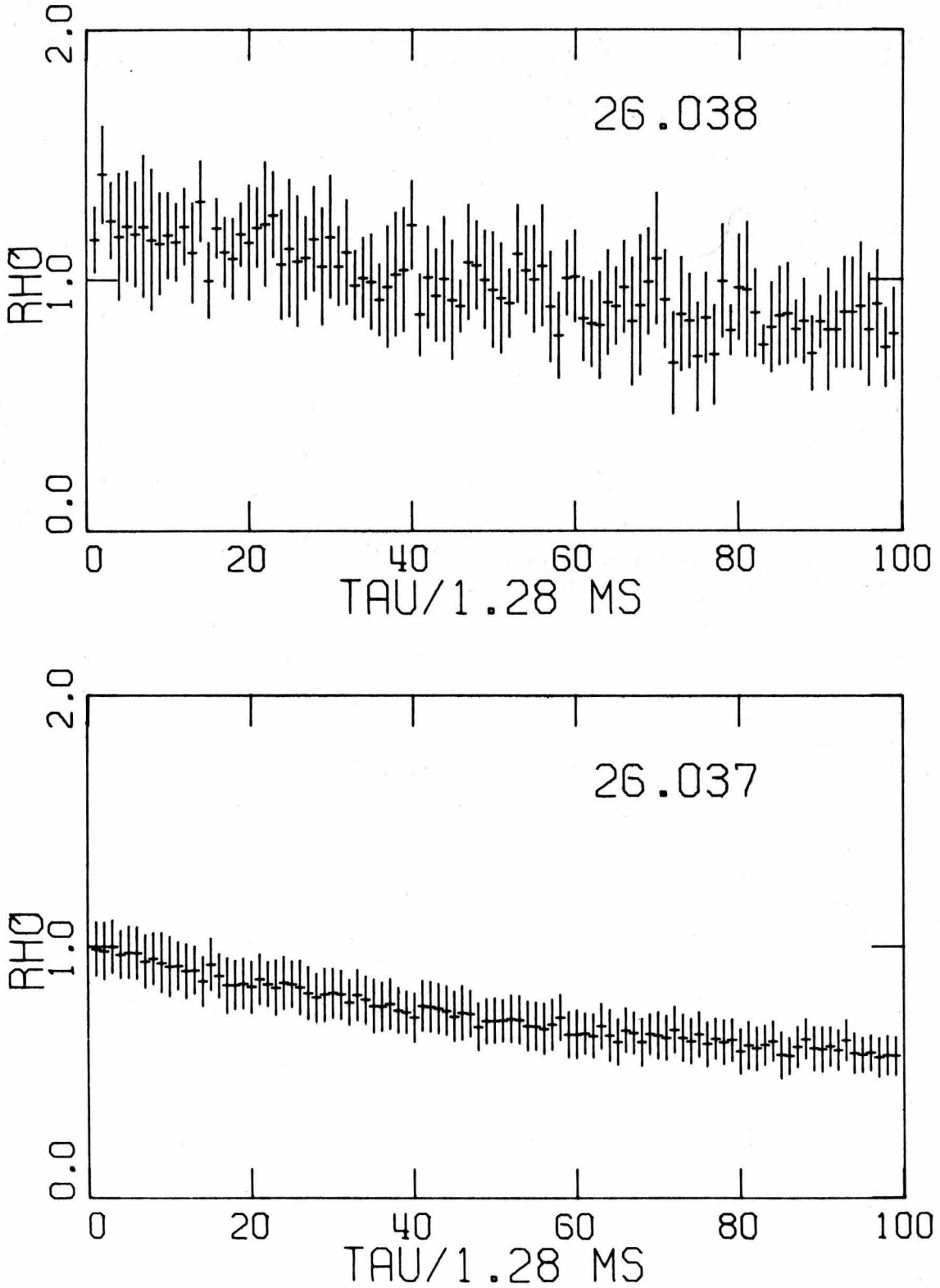
26.038
RHO
2.0
1.0
0.0
0
20
40
60
80
100
TAU/1.28 MS
26.037
RHO
2.0
1.0
0.0
0
20
40
60
80
100
TAU/1.28 MS

Figure 5 a&b

as suggested by F. Lamb (private communication). For any continuously differentiable function f(t), the linear term is zero, so that the autocorrelation has zero slope at $\tau = 0$. The autocorrelation $e^{-\tau/\tau_o}$ ($\tau \geq 0$) of an exponential shot has a finite slope at zero time delay because the shot has zero rise time and is thus discontinuous at $t = 0$. The apparent sharpness of the observed autocorrelations near $\tau = 0$ thus implies a sharp edge to the function f(t). For example, a signal composed of shots with a finite exponential rise of characteristic time τ_1 and decay time τ_o has, in the limit of small bin size and long data set length,

$$\rho(\tau) = \frac{\tau_o e^{-\tau/\tau_o} - \tau_1 e^{-\tau/\tau_1}}{(\tau_o - \tau_1)} \quad . \tag{4}$$

When fit to equation (4), the "fast" autocorrelations were consistent with $0 < \tau_1 < 11.5$ ms (October 1974) and $0 < \tau_1 < 19$ ms (present flight) at a 90 percent level of confidence. Similarly, for the assumption of triangular shots with rise-time from half power τ_1 and fall time to half power τ_o, the autocorrelations indicated $0 < \tau_1 < 20$ ms (October 1974) and $0 < \tau_1 < 32$ ms (present flight). The lack of downturn at low time delay of the autocorrelation thus indicates the presence of shots with a rapid rise time, or, since the autocorrelation is time-symmetric, rising shots with a rapid fall time.

d) Cross-correlations

Cross-correlations between data in the low energy band (0.6-1.5 keV) and in the high energy bands (3.0-20 keV) taken during the present flight were calculated to look for any energy dependent time delay in the data. The cross-correlation function was defined:

$$CC(u) = \frac{\frac{1}{(N-1-|u|)} \sum_{i=\max(1,1+u)}^{\min(N,N+u)} (s_{i,LO}-\bar{s}_{LO})(s_{i-u,HI}-\bar{s}_{HI})}{\frac{1}{(N-1)} \sum_{i=1}^{N} (s_{i,LO}-\bar{s}_{LO})(s_{i,HI}-\bar{s}_{HI})}, \qquad (5)$$

where $s_{i,LO}$ and $s_{i,HI}$ are the counting rate in low and high energy channels. $\bar{s}_{LO}$ and $\bar{s}_{HI}$ are the average values of $s_{i,LO}$ and $s_{i,HI}$. $N-|u|$ terms are summed in the summation, as $|u|$ terms are lost to "overhang" in the cross-correlation. Cross-correlations were calculated for each of the four data sets, then averaged in the same way as the autocorrelations. Ten 20.99 sec Cyg X-1 data sets from both previous flights of the payload were also analyzed to cross-correlate data in the bands 1.5-3.0 keV and 12.0-42.0 keV. Results of the cross-correlations are shown in Figure 6.

For exponential shots with equal decay times in the high and low energy bands τ_o and lag between shots $\Delta\tau$ (in the sense that $\Delta\tau > 0$ implies that the shots at low energy lag behind those at higher energy), a cross-correlation normalized at $u = 0$ has the form:

Figure 6

(a) Cross-correlation between counts in the bins 0.6-1.5 keV and 3.0-20 keV for Cyg X-1 data obtained during flight of May 1976. (b) Cross-correlation between counts in the bins 1.5-3.0 keV and 12 keV for Cyg X-1 data obtained during flights of October 1973 and October 1974. Delay τ is in units of 0.1024 second. Error bars are 1σ.

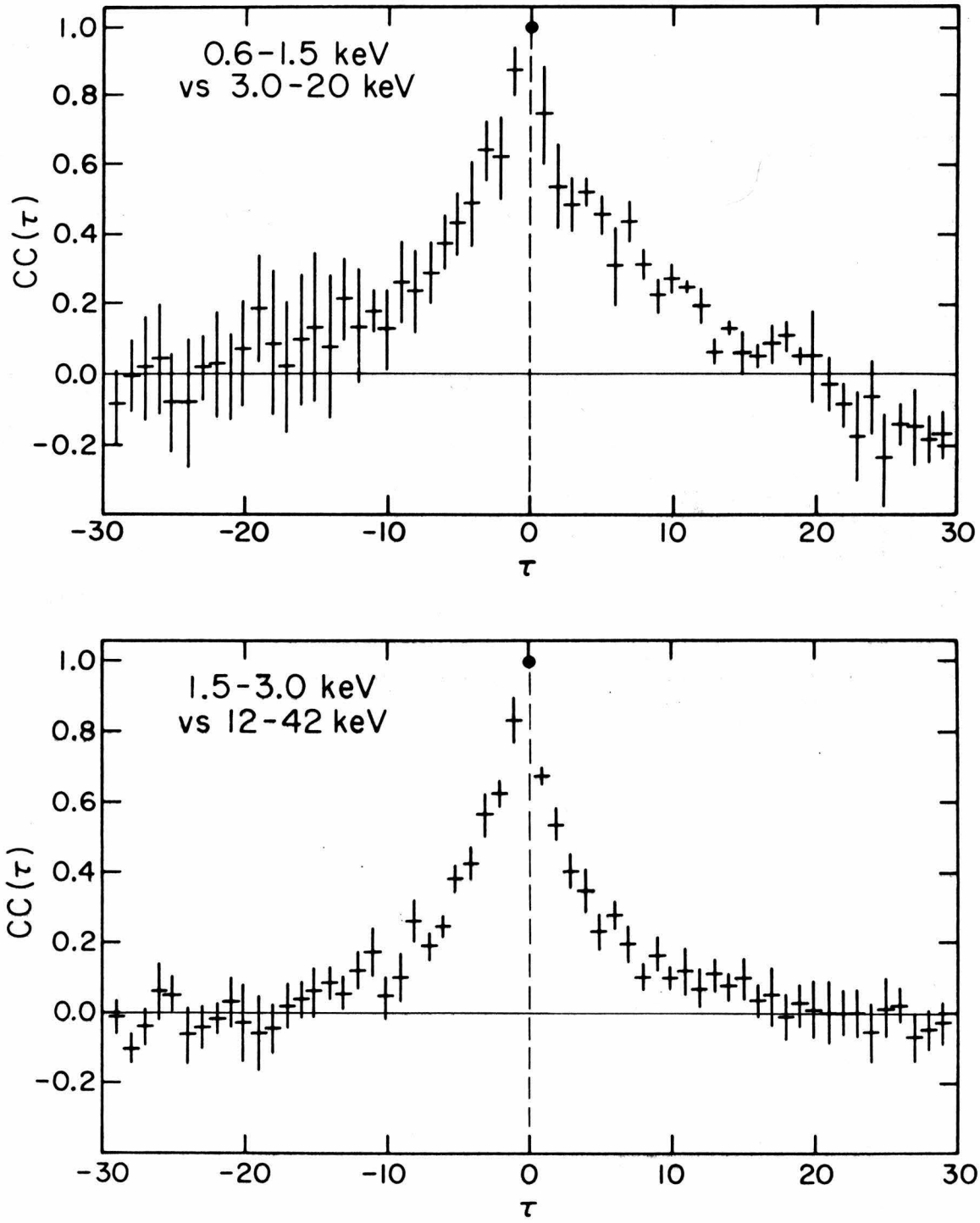

Figure 6 a&b

$$\langle CC(u) \rangle = e^{\left|\frac{\Delta\tau}{\tau_o}\right|} e^{-\left|\frac{\tau-\Delta\tau}{\tau_o}\right|} \qquad (6)$$

in the limit of large data set length N. Since the cross-correlations, particularly those of the data of October 1973 and October 1974, seemed to show some asymmetry, they were fit to (6) to determine the significance of any offset. The following limits on the offset (at 90 percent confidence level) were derived: October 1973 and October 1974, 1.5-3.0 keV vs 12.0-42.0 keV, -0.041 sec $< \Delta\tau < -0.004$ sec; present flight, 0.6-1.5 keV vs. 3.0-20.0 keV, -0.031 sec $< \Delta\tau < 0.026$ sec.

The data of the October 1973 and October 1974 flights suggest that the high energy flux lags the low energy flux. For all three flights, any time lag has absolute value $|\Delta\tau| < 40$ msec.

e) Shot Parameters

Energy-binned data of the three flights were fit to the exponential shot model worked out by SWK in another attempt to detect an energy dependence of the rapid variabilities. In that model, identical exponential shots of zero rise time, decay time τ_o sec, and peak counting rate h cts/sec occur at a rate λ sec^{-1}. They comprise a fraction f of the time averaged flux, the rest of which is constant. The shot parameters were calculated as follows:

τ_o was derived from the best fit of the autocorrelation to (2).

$$hT = \frac{3}{2}\frac{\langle M_{3s}\rangle}{\langle V_s\rangle} \quad , \tag{7a}$$

$$\lambda\tau_o = \frac{8}{9}\frac{\langle V_s\rangle^3}{\langle M_{3s}\rangle^3} \quad , \text{ and} \tag{7b}$$

$$f = \frac{4}{3}\frac{\langle V_s\rangle^3}{\langle M_{3s}\rangle\langle s\rangle} \quad . \tag{7c}$$

$\langle M_{3s}\rangle$, $\langle V_s\rangle$, and $\langle s\rangle$ are the third moment, variance, and counting rate per bin corrected for binning, photon statistics, finite data set length, and background (SWK). The shot parameters were calculated for each 20.99 second data set, then averaged to determine the value and error of the true shot parameters. The values calculated are tabulated in Table 1. The large errors quoted are mainly due to scatter in the third moment M_3, which is not well determined by the relatively short runs of data used.

The parameters derived are similar to those derived from UHURU data on Cyg X-1 by SWK. It is clear that not all of the flux is in shots. There is a significant difference in shot fraction, decay time, and rate between the present flight and the two earlier flights. Though photons detected in the xenon-argon detector configuration of October 1973 and October 1974 had a substantially higher mean energy than in the later flight, it is difficult to ascribe the difference in shot parameters between the flights to an energy dependence, because of the lack of

energy dependence of these parameters within each set of data. The results listed in Table 1 are consistent with shot parameters on each flight being energy-independent.

f) Time-skewness

Since the autocorrelation function is time symmetric, the exponential autocorrelation, eq. (2), of a signal composed of rising exponential shots with zero rise time is identical to that of a signal of rising exponential shots with zero fall time. In order to separate these possibilities, the time-skewness function of the data was calculated,

$$TS(u) = \frac{1}{T^3} \frac{1}{N-1-|u|} \sum_{\max(1,1+u)}^{\min(N,N+u)} (s_i\, s_{i-u}^2 - s_i^2\, s_{i-u}) \qquad (8)$$

as suggested by Katz (private communication). Note that $TS(\tau) = -TS(-\tau)$ and $TS(0) = 0$. In the limit of small bin size T/τ and large data set length N the expected value of time-skewness for the exponentially falling shot signal defined above is:

$$TS(\tau) = \frac{\lambda h^3 \tau_o}{3} e^{-\tau/\tau_o} (1-e^{-\tau/\tau_o}) \qquad (9)$$

For rising exponential shots, $\langle TS(\tau) \rangle$ is of opposite sign.

The time-skewness function evaluated at $1 \leq u \leq 48$ ($0.10 \text{ sec} \leq \tau \leq 4.92 \text{ sec}$) was calculated for each 20.99 sec data set of the data from the three flights and averaged. Data of all energies were summed

to improve statistics. Mean time-skewness functions are shown in Figure 7. The expected time-skewness for falling exponential shots with λ, h, and τ_o as calculated above are also shown.

The two mean time-skewness functions were fit to the form $TS(\tau) = Ce^{-\tau/\tau_o}(1-e^{-\tau/\tau_o})$ in order to compare the expected and observed time-skewness. For the shot-noise parameters calculated for the data from the present flight, we expect $0.97 \times 10^6 < C < 9.3 \times 10^6$, while the calculated time-skewness allows $-0.71 \times 10^6 < C < 0.25 \times 10^6$ (1σ error) for $\tau = 1.20^s$. Similarly, for the earlier data, we expect for falling exponential shots $2.2 \times 10^7 < C < 14 \times 10^7$ while the calculated time-skewness implies $-0.29 \times 10^7 < C < -0.14$ for $\tau_o = 0.68$ seconds. Though the time-skewness functions calculated look more like those expected for rising exponentials than for falling exponentials, they are consistent with neither. The absolute value of the time-skewness is rather smaller than expected, which would seem to indicate that the actual shots are more time-symmetric than exponential ones.

This discrepancy between shot-noise parameters and the time-skewness is not surprising considering the ad hoc nature of the shot assumption: that the observed signal consists of shots of identical size and shape. If the signal is composed of shots with a distribution of parameters, the relation between the autocorrection, time-skewness, and other calculable quantities can be quite different. Consider a signal composed of randomly occurring rectangular shots of constant height h and width T distributed such that: probability that T is in

Figure 7

(a) Time-skewness function calculated for 0.6-20 keV data from flight 26.038 (May 1976). (b) Same for 1.5-42 keV data of October 1973 and October 1974 (flights 13.010 and 26.037). Error bars are 1σ. Delay τ is in units of 0.1024 second. Shaded region is the 1σ range of time-skewness expected for falling exponential shots with shot parameters as derived from the data.

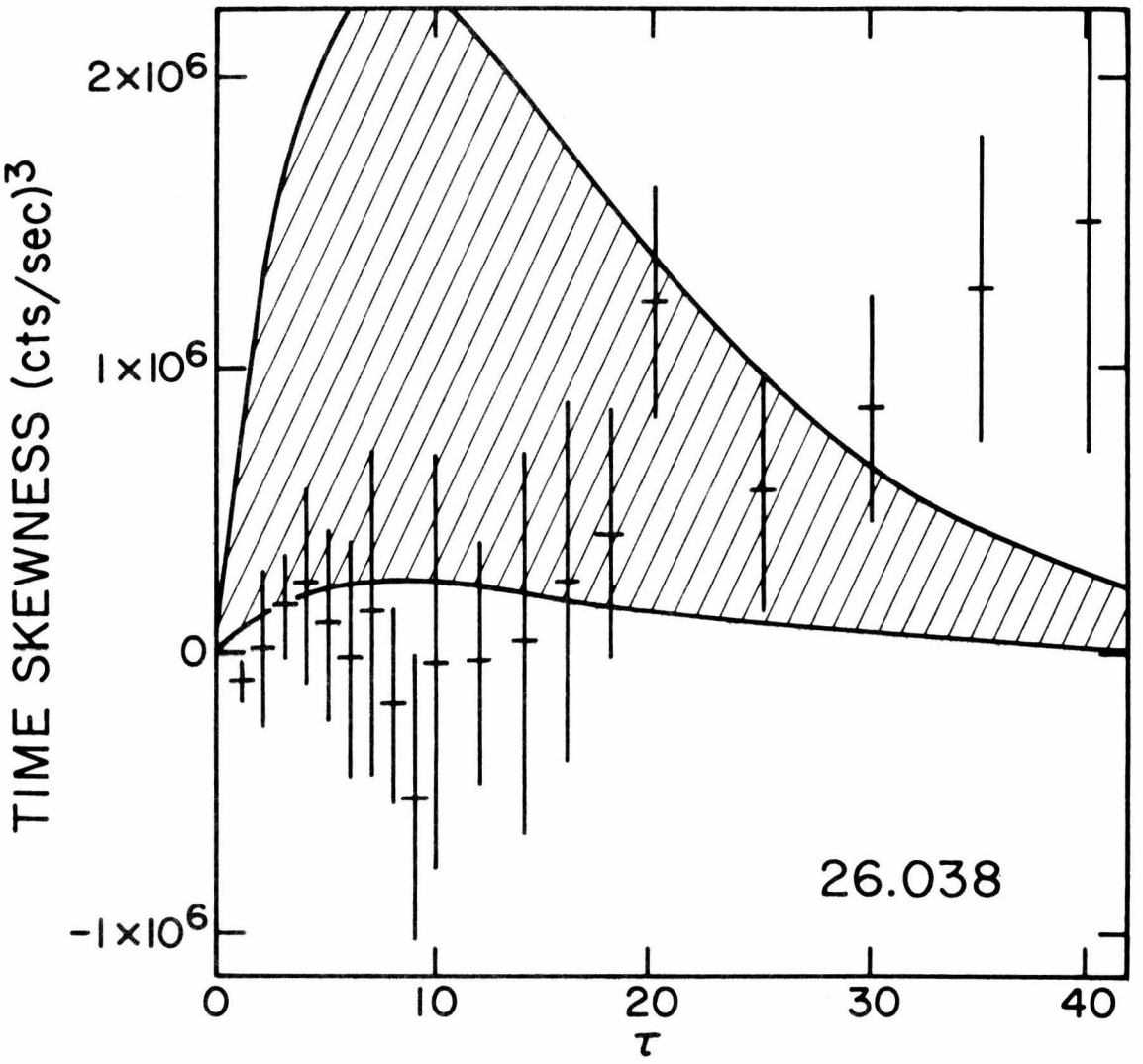

Figure 7a

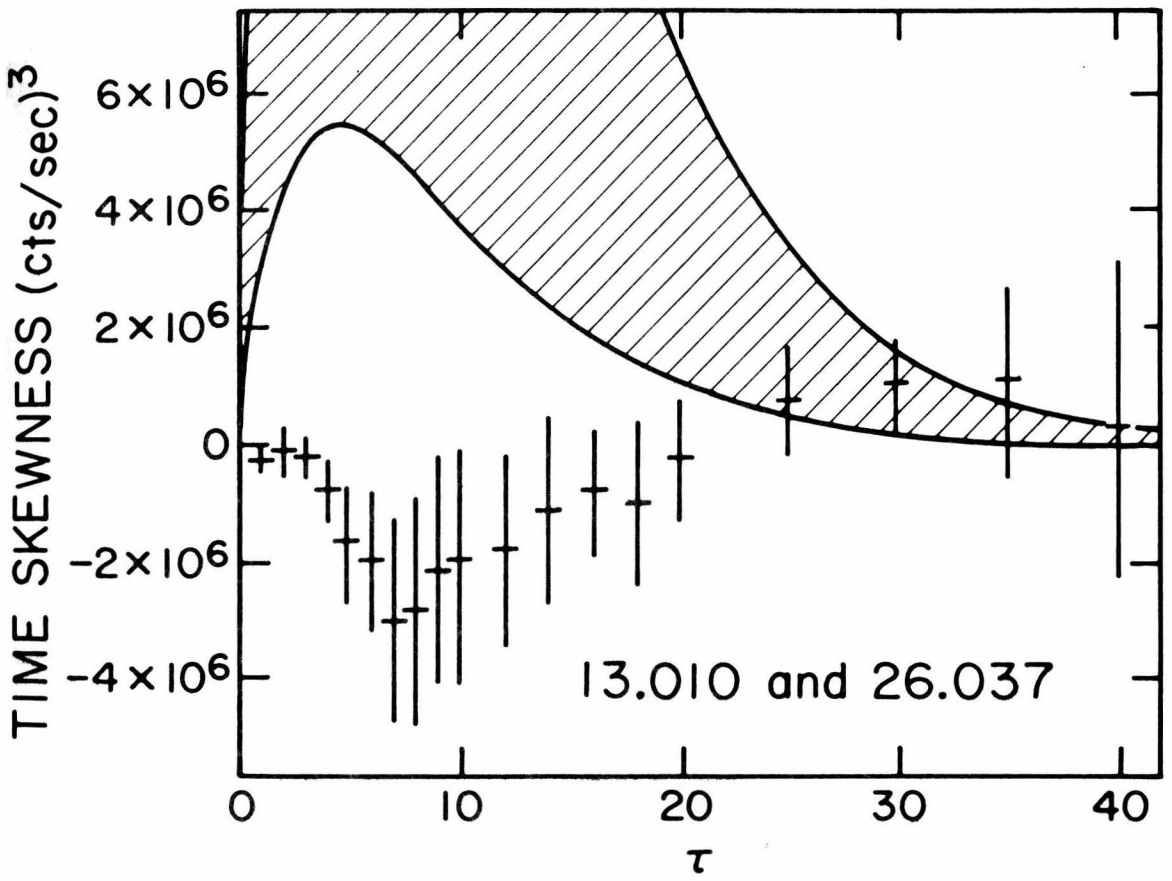
TIME SKEWNESS (cts/sec)^3
6×10^6
4×10^6
2×10^6
0
-2×10^6
-4×10^6
13.010 and 26.037
0
10
20
30
40
τ

Figure 7b

the range T to T + dT $\equiv \frac{d\lambda}{dT}\, dT = \lambda_o \frac{T}{\tau_o} e^{-T/\tau_o}\, dT$.

The autocorrelation of this signal is identical to that for exponential shots,

$$\rho(\tau) = e^{-\tau/\tau_o}. \qquad (11)$$

However, since each square shot is time-symmetric, the time-skewness of the signal vanishes.

A purely exponential distribution of rectangular shots $\frac{d\lambda}{dT} = \lambda_o e^{-\tau/\tau_o}$ produces an autocorrection $\rho(\tau) = e^{-\tau/\tau_o} - \tau/\tau_o\, E_1(\tau/\tau_o)$ which falls more steeply than an exponential. This distribution of shots, too, may provide a satisfactory fit to the calculated autocorrelations, which indeed deviate from an exponential fit in the sense that they are too steep at small time delays. Consideration of an exponential distribution of rectangular shots could prove to be informative in testing specific physical models. For example, consider the hypothesis that the rapid variability ($\lesssim$ 1s) of Cyg X-1 arises from statistically independent and distinct "hot" spots and that, apart from possible millisecond blips (e.g., due to the eclipse of the disturbance by a blackhole (Sunyaev (1972)), the observed radiation to be associated with each spot is essentially constant during the lifetime of that spot (i.e., they are not flare-like). Furthermore, consider that the probability per unit time for a spot to disappear (e.g., cross the event horizon) is also independent of time and that the spots are otherwise identical (i.e., same height). This very simple model of temporal homogeneity for the spots leads to rectangular "shots"

distributed such that $d\lambda/dT = \lambda_0 e^{-\tau/\tau_o}$.

If the description of the shots includes a distribution of shot frequency over parameter space, the problem of shot description is quite underdetermined. The exponential shot model is probably still useful, not in a literal sense, but to assign some characteristic values to a rapidly varying signal.

g) Millisecond Bursts

A search was made for millisecond bursts as described by Rothschild et al. (1974) over 84 seconds of exposure to Cyg X-1. None were seen when less than one spurious burst was expected by chance. This method would not have detected bursts similar to those previously seen if the total detector counting rate was half or less of that for the Oct. 1973 flight (Rothschild et al. 1974). In this flight the exposed effective area and detector counting rate were 75 percent of that flight. If the bursts are not soft (minimum energy > 2 keV), then less than half of the area of the Oct. 1973 flight was available for burst detection, and it is not surprising that none were detected. Another possibility is that the statistics of small numbers conspired against us. That is, the burst rate from the two earlier flights was .057 sec^{-1} (13 bursts in 230 sec exposure) so that we would expect a mean of 4 1/2 bursts in 84 sec. However, if the bursts are randomly distributed, there is a 1 percent chance of no bursts in 84 sec. A third possibility is that burst visibility is orbital phase dependent. The May 1976 flight occurred at orbital phase 0.82, while the earlier flights both were at phase 0.17.

V. CONCLUSION

The most striking feature of the data is the absence of energy dependence of the temporal variation of Cyg X-1. Cyg X-1 is thus different from the X-ray pulsators Her X-1 and Cen X-1, which show a decreasing pulsed fraction at lower energies (Shulman et al. 1975; Long, Agrawal, and Garmire 1975). Explanation of the low energy excess of Cyg X-1 as the emission from an extended region separate from the high energy source, as in the pulsators, is thus not tenable.

The stability of the power-law spectrum of Cyg X-1 through the shot-noise variation, as evidenced by constant hardness ratios, and the lack of energy dependence of shot-noise parameters, suggest that the spectrum has a Comptonization origin. SLE propose a model in which the hot inner accretion disk produces the power-law spectrum by Comptonization of soft photons. In this model the inner disk is quite uniform in temperature and optical depth. Thus, each region of the inner disk contributes roughly the same spectrum as the entire source, so that a flare which emphasized one region would have the mean spectrum. The Comptonized spectrum is buffered against changes in the source luminosity, so that the variations in intensity over seconds of a factor of 2-3 seen in Cyg X-1 would not be expected to affected the spectrum. The power-law spectrum would thus be little affected either by local flares or overall brightenings of the inner disk. A Comptonized spectrum is thus suggested on the basis of the stability of the power-law portion of the spectrum alone.

When combined with the conclusion that there is an excess flux above the power-law spectrum at low energies, the lack of energy dependence of the shot-noise variability indicates a soft X-ray component in a constant ratio to the power-law flux. That source must be modulated by the same mechanism as the hard X-rays. Our understanding of the shot noise variability is confused by the fact that it does not occur on time scales typical of the inner accretion disk. From the SLE model, characteristic timescales of the hot "two-temperature" region responsible for the power-law spectrum can be calculated. Assuming black hole mass $M_{hole} = 10\ M_{\odot}$, mass accretion rate $\dot{M} = 7 \times 10^{17}$ g sec^{-1} and viscosity parameter α, the following times are characteristic at a radius $r = 10\ \frac{GM}{c^2}$, inside the hot inner region:

$$\text{light-crossing time} = r/c \sim 5 \times 10^{-4} \text{ sec},$$

$$\text{Kepler time} = 2\pi r^{3/2}\ (GM_{hole})^{-1/2} \sim 10^{-2} \text{ sec},$$

$$\text{electron thermal time} = \frac{3/2\ kT_e \Sigma}{m_p F} \sim 5 \times 10^{-5} \text{ sec},$$

$$\text{and drift time} = v_r/r \sim 6 \times 10^{-3}\ (\frac{\alpha}{0.1})^{1/6} \text{ sec},$$

where Σ is the disk surface density, v_r is the radial velocity, and F is the luminosity per unit surface area from each side of the disk. The shot decay time $\tau \sim 1$ sec observed in this and other experiments is uncharacteristic of the time scales expected for flares and instabilities in the inner region. During one shot decay time, the contents of the hot inner region are replaced several times.

If we assume that the excess flux observed at low energies is the tail of the distribution of soft photons that feed the power law spectrum, certain constraints can be set on the origin of the soft flux. If cyclotron radiation from the expected equipartition magnetic field in the inner disk of $B \approx 10^7$ gauss is optically thick up to the 50th harmonic, as suggested by Eardley and Lightman (1976), any cyclotron photons should have a maximum energy of 5 eV. The energy of the observed soft flux thus rules out thermal cyclotron radiation in the inner disk as a source. The spectral data allow an origin for the soft flux from bremsstrahlung from the thin disk outside the inner region, or from cool dense condensations within the inner region.

Instability on a time-scale of seconds may occur in the cool disk outside the hot region. It might be expected that resulting changes in the soft flux might be reflected by proportional changes in the power law spectrum, as the number of soft photons Comptonized changes. However, SLE have shown that the temperature of the inner region will be adjusted in order to radiate the energy produced in that region. This adjustment will take place on a thermal time scale. Variability in the soft flux on a time-scale of seconds thus could not modulate the power law flux. In the context of a Comptonization model, the small thermal time scale of the electrons implies that a soft-hard X-ray proportionality is also a proportionality between the soft X-ray flux and the energy flux into the electrons.

An increase in the soft flux from the cooler regions outside the inner disk, that was caused by a change in the mass flow rate through the disk, might be followed by an increase in power-law luminosity, as the extra flow reached the inner region. A lag of order the drift time through the portion of the cool region responsible for the soft flux would be expected between the brightening at low and high energies. However, the drift time is of order tens of seconds (Novikov and Thorne, 1972) while the lag indicated by the cross-correlations is not more than 40 ms. There thus appears to be no mechanism to couple variations in the inner disk and the region exterior to it on a shot-noise time scale. We suggest that the soft and hard X-rays must originate in the same region (the soft flux coming perhaps from cool condensations inside the inner region).

The time lag suggested by cross-correlation data is in the sense expected for a Comptonized spectrum: high energy flux lags low energy flux. In the Comptonization region, cool photons increase in energy by a factor $\frac{\Delta E}{E} = \frac{4kT_e}{m_e c^2}$ per Compton collision time $t_c = \frac{r_{hot}}{c\tau_{es}}$. An increase in intensity at high energy E_{HI} should lag the increase at lower energy E_{LO} by a delay ΔT of order $\Delta T \sim \frac{\ell n(\frac{E_{HI}}{E_{LO}})}{\ell n(\frac{\Delta E}{E})} t_c$, since $\frac{\ell n(\frac{E_{HI}}{E_{LO}})}{\ell n(\frac{\Delta E}{E})}$ collisions are required to bring photons from the low band up to the high band. Similarly, if the un-Comptonized soft flux is observed,

a delay $\Delta T \sim \frac{\ell n(\frac{E_{HI}}{E_s})}{\ell n(\frac{\Delta E}{E})} t_c$ should be observed, where E_{HI} is high energy band observed and E_S is the mean energy of the soft source (not necessarily the energy of the tail of the soft flux being observed). One expects, for the SLE model parameters above, ΔT(0.6-1.5 keV vs > 3.0 keV) $\sim 0.4\ \ell n(\frac{4.0\ keV}{E_S})\ t_c \sim 2 \times 10^{-4}$ s for E_s = 50 eV (the factor 0.4 represents the fraction of soft flux seen in the 0.6-1.5 keV band). Similarly, ΔT(1.5-3.0 keV vs 12-42 keV) $\sim \ell n(\frac{15\ keV}{2.5\ keV})\ t_c \sim 1 \times 10^{-4}$ s. The time lag ΔT(1.5-3.0 keV vs 12-42 keV) of 22 ± 18 ms suggested by the cross-correlation data from the first two flights would imply a Comptonization region much different from that of the SLE model. For similar electron temperature and optical depth, a hot region ~ 200 times the extent of the SLE two-temperature region, with $r_{hot} \sim 3 \times 10^8$ cm, would be required. This result would support a coronal model of Cyg X-1, in which the X-ray flux is produced by Comptonization in a hot corona extending above the accretion disk (Price and Liang, 1975; Bisnovatyi-Kogan and Blinnikov, 1977; Piran, 1977).

The time-skewness calculation indicates that the variability of Cyg X-1 is the result neither of rising nor of falling identical exponential shots. The sign of the time-skewness rules out any distribution of falling shots. We concur with Canizares and Oda (1977) that there is a fundamental distinction between the activity of Cyg X-1 and to astrophysical burst phenomena, which shows a fast rise and slower decay. There is thus no obvious analogy to be made between Cyg X-1 and the X-ray bursters.

The lack of time skewness cannot be the result of shots which rise and fall gently ($\tau_{up} \approx \tau_{down} \approx 1$ second), as an upper limit to rise or fall time is set by the sharpness of the autocorrelation at small τ. A distribution of square shots with similar rapid rise and fall times may be allowed. We are led to the conclusion that the shot-noise variability is the result of a distribution of shots with different parameters. There is therefore no decay time common to all the shots which might be interpreted as a reverberation time. This result is not surprising, as a characteristic time of order the shot time would be long even for a coronal model.

The upper limit to shot rise or fall time set by the "fast" autocorrelations implies a time scale $\lesssim 0.01$ sec in variability of Cyg X-1. That time is among the fastest measured for an astrophysical event, but it may be allowed in a "slow", extended corona model of Cyg X-1. Further data would be valuable to extend this analysis to look for time scales of the order expected from present "compact" models such as that of Shapiro, Lightman, and Eardley. Refinement of the autocorrelation at small time delays may indicate the characteristic time of the shot edges. The time lag of high energy flux suggested by these data, if confirmed by cross-correlations of a more extensive data set, would require an emission region in Cyg X-1 larger than expected by present theory.

TABLE 1
SHOT NOISE PARAMETERS FOR CYG X-1

	May 1976				
	0.6-1.5 keV	1.5-3.0 keV	3.0-6.0 keV	>6.0 keV	All Data
Decay Time τ_o (sec)	1.2 ±0.5	1.8 ±1.0	1.0 ±0.4	1.3±0.6	1.2 ±0.6
Shot Fraction f	0.26±0.15	0.41±0.11	0.27±0.37	*	0.38±0.06
Shot Rate $\lambda(sec^{-1})$	0.6 ±0.2	1.3 ±0.6	1.7 ±0.5	*	1.2 ±0.5
Detected Counts Per Shot $h\tau_o$	40±50	160±90	40±25	*	270±140
Shot Rise Time τ_1 (seconds, 90% confidence range)	---	---	---	---	$0<\tau_1<0.019$
Shot Lag $\Delta\tau$ between 6-20 keV and 0.6-1.5 keV bands (seconds, 90% confidence range)	---	---	---	---	$-0.031<\Delta\tau<0.026$

	October 1973 and October 1974			
	1.5-3.0 keV	3.0-12.0 keV	>12.0 keV	All Data
Decay Time τ_o (sec)	0.77±0.14	0.65±0.10	0.68±0.13	0.68±0.09
Shot Fraction f	0.36±0.18	0.66±0.13	0.42±0.10	0.63±0.14
Shot Rate $\lambda(sec^{-1})$	3.0 ±1.3	3.2 ±1.2	1.3 ±0.4	3.8 ±1.1
Detected Counts Per Shot $h\tau_o$	44±16	124±40	25±10	285±95
Shot Rise Time τ_1 (seconds, 90% confidence range, October 1974 data only)	---	---	---	$0<\tau_1<0.012$
Shot Lag $\Delta\tau$ between 12-42 keV and 1.5-3.0 keV bands (seconds, 90% confidence range)	---	---	---	$-0.041<\Delta\tau<-0.004$

All errors are 1σ.

*Number of counts in bin insufficient to determine parameters.

CHAPTER 2

A ROCKET OBSERVATION OF CYG X-2

I. INTRODUCTION

The primary scientific purpose of Aerobee flight 26.038 was a time resolved proportional counter observation of Cyg X-1 at low and medium X-ray energies (see Chapter 1). To verify experiment performance, it was felt desirable to make a short pointed observation of another cosmic X-ray source during the mission. The second source was chosen to be one for which variation on a time scale of seconds would not be expected, in order to show that the chaotic variability expected from Cyg X-1 was not a detector artifact. The source thus chosen for a 20-second observation was Cyg X-2.

Cyg X-2 appears to be similar to Sco X-1, the brightest persistent X-ray source in the kilovolt band (c.f., Peimbert et al. 1968). Both sources appear to be members of the class of unpulsed X-ray sources with soft spectra ($\langle E \rangle < 10$ keV), in contrast to the X-ray pulsators which show hard spectra (Maraschi et al. 1977). Other sources for which a soft spectrum and lack of pulsations have been demonstrated include the bright X-ray transient A0621-00 (Bradt and Matilsky 1975), and several bright galactic center X-ray sources, including GX5-1, GX9+1, GX17+2, GX340+0, and GX349+2 (Gorenstein, Giacconi, and Gursky 1967; Cruddace et al. 1972; Rappaport et al. 1971; Rappaport, Bradt, and Mayer 1971). Most of the still unidentified galactic sources seem to fall in this class.

Understanding of the hard X-ray pulsators is facilitated by the wealth of periodic phenomena detectable in these systems. Most of the pulsators have been identified as binaries from X-ray eclipse, Doppler shift, and optical identification data. The hard X-ray pulsators are understood to be binary systems consisting of a normal star, usually of early type, and a neutron star rotating at the pulsator period, which accretes matter to produce X-rays. In contrast, analysis of the unpulsed X-ray sources has been frustrated by the lack of a phenomenological "handle". Among the sparse data about periodic behavior of these sources is a 0.79-day period of Sco X-1 seen in optical emission line radial velocities (Cowley and Crampton 1975), and a reported 11.2-day X-ray modulation of Cyg X-2 (Holt et al. 1976).

Though it is thought to be similar to Sco X-1, observations of Cyg X-2 have been limited in comparison to observations of its alleged compatriot (see Arons and Rothschild 1975). The preference for Sco X-1 is the result of the factor of $\sim$ 30 difference in flux between the two sources (Giacconi et al. 1974). Because of its brightness, observation of Sco X-1 was not difficult even with the spinning rocket payloads of the early days of X-ray astronomy, while to obtain good counting statistics on Cyg X-2, a slowly scanning or pointed detector is required.

The observation of Cyg X-2 during flight 26.038 was undertaken in hopes of finding some spectral or time signature which might be amenable to analysis. The high time resolution and pointed observation allow searches for fast periodicity which had not been previously undertaken. Failure to detect pulsations from Cyg X-2 would serve to secure its place in the class of soft unpulsed galactic X-ray sources.

II. OBSERVATIONS

A 20-second pointed observation of Cyg X-2 was made just prior to the extended observation of Cyg X-1 (see Chapter 1) during Aerobee flight 26.038. The detector payload is described in Appendix A. Approximately 24,000 counts above background were detected from Cyg X-2 during the pointing, so that spectral and temporal analysis of the data could be done with good statistical accuracy.

Spectral information from the two detectors were analyzed separately. Data from the MED were fit to a hydrogen bremsstrahlung spectrum $\frac{dN}{dE} = \frac{C}{E} e^{-E/kT} e^{-\sigma n_x}$, with C = 2.9 photons cm^{-2} sec^{-1} keV^{-1}, kT = 4.4 ± 0.4 keV, and n_x in the range 0.0-0.8 x 10^{21} atoms cm^{-2}, with 90% degree of confidence. That the fit was satisfactory is indicated by a minimum χ^2 of 0.96 per degree of freedom. The raw spectral data and best fit bremsstrahlung spectrum, folded through detector efficiency and broadening, are shown in Figure 1. Because of the low value of source absorption, most of the observed low energy absorption is from the detector window.

The most significant spectral constraint set by the LED data came from the 1/4 keV detector band, where a low value of n_x would produce a detectable flux. Data in the 1/4 keV band are confused by irregularities in the low energy diffuse background. A difference in background between the background region scanned in transit between Cyg X-2 and Cyg X-1 and the vicinity of Cyg X-2 seems to be the cause of a negative 1/4 keV signal (corrected for background) from Cyg X-2. Preliminary HEAO A-2 data suggest the presence of several soft X-ray sources in the region of Cyg X-1, which may also serve to confuse the 1/4 keV background measurement. If we assume an upper limit to the flux in the 1/4 keV band from

Figure 1

Medium energy detector spectrum of Cyg X-2 derived from a 20 second observation during flight 26.038. The points are the pulse height analyzed raw spectrum of Cyg X-2. Vertical error bars represent 1σ counting statistics. The stepped curve through the points is the best fit incident spectrum $dN/dE = 4.4\ e^{-E/(4.4\ keV)}\ e^{-\sigma n_x}$, where $n_x = 0.1 \times 10^{21}$ hydrogen atoms cm^{-2}.

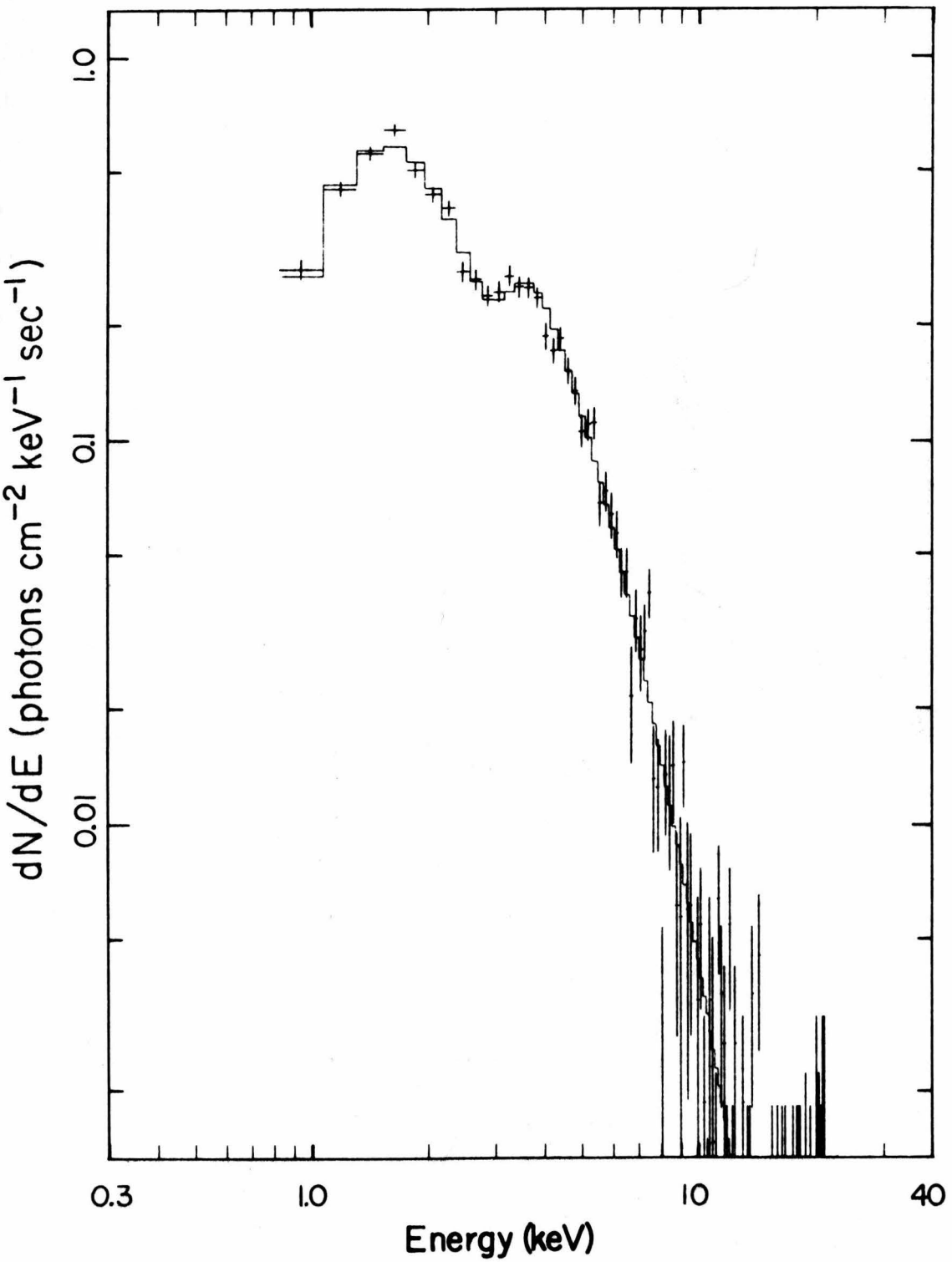

Figure 1

Cyg X-2 of three times the difference in flux measured at Cyg X-2 and the background region, the absorbing column density n_x must be not less than 0.4×10^{21} atoms cm^{-2}. Observations by the low energy detectors of the HEAO A-2 experiment, which scan the region of Cyg X-2 repeatedly, and can thus better establish the 1/4 keV background at the source, may substantially lower this upper limit on the 1/4 keV flux from Cyg X-2.

Though Cyg X-2 is clearly variable on a time scale of days (Holt et al. 1976), no evidence for fast variability was evident during the pointed observation. Scaler data (the sum of all counts between thresholds in the LED and MED) summed in 1.28 ms bins showed a distribution consistent with Poisson counting statistics for a constant source. An array of 32768 320 μsec bins of scaler data was transformed by a fast Fourier transform (FFT) to search for possible periodicities. Any periodic modulation of Cyg X-2 of pulsed fraction $f > 8\%$, where flux $I(t) = I_0 (1 + f \cos \frac{2\pi t}{P})$, would have been detected at a confidence level greater than 99% for any period in the range searched. We thus conclude that the flux from Cyg X-2 has a mean pulsed fraction less than 8% for 640 μsec < P < 10.24 sec in the X-ray band observed in this experiment.

III. DISCUSSION

The thermal bremsstrahlung spectrum of Cyg X-2 measured during this flight agrees well, except for intensity, with previous measurements by Bleach et al. (1972)($C = 1.4 \pm 0.3$ photons $cm^{-2} sec^{-1} keV^{-1}$, $kT = 4.5 \pm 0.7$ keV,

$n_x < 2 \times 10^{22}$ atoms cm^{-2}), and Stevens, Garmire, and Riegler (1972) ($C = 1.4 \pm 0.4$, $n_x = 0.8 \pm 0.4 \times 10^{21}$ atoms cm^{-2}, with kT assumed equal to 4.5 keV). The factor of two intensity difference between the three rocket observations can be explained by the day-to-day variations seen by the Ariel V All-Sky Monitor experiment (Holt et al. 1976). The X-ray spectrum of Cyg X-2 is thus similar to Sco X-1, which typically has $kT \geq 5.5$ keV (Culhane et al. 1975). The spectrum measured on this flight, as well as the observed lack of pulsation, serves to confirm the similarity of the Cyg X-2 and Sco X-1 systems.

It has been suggested by Elsner and Lamb (1976) and by Maraschi, Treves, and van den Heuvel (1977) that the soft unpulsed X-ray sources generate energy by the same process as the hard X-ray pulsators, i.e., by mass accretion onto a neutron star. X-ray pulsation at the neutron star period would be suppressed if the neutron star has no magnetic field to channel the accretion flux, or if the magnetic field was aligned with the neutron star axis of rotation. Even if the rotating neutron star had an offset magnetic field, pulsations could be suppressed if the flux from the neutron star had to emerge from an optically thick cloud about it. Compton scattering within the cloud would smooth the time variation of the flux from the neutron star. Transfer of energy $\langle \Delta E/E \rangle = - E/m_e c^2$ per collision, from high energy photons to cooler electrons, could transform incident hard spectra into the softer spectra observed in the nonpulsed sources. The emergent spectrum from a cool electron cloud of optical depth τ_{es} is cut off at $E > E_{max}$, where $E_{max} = m_e c^2 / \tau_{es}^2$ (Illarionov and Sunyaev 1972), so that a

"pseudo-bremsstrahlung" spectrum cooler than the original spectrum can be generated. To produce a spectrum similar to that of Cyg X-2, we require E_{max} about 10 keV and thus τ_{es} about 7. In the remainder of this discussion we examine whether the picture of Cyg X-2 as a hard X-ray pulsator such as Her X-1, hidden in a cloud optically thick to Compton scattering, is consistent with observations.

A sharp X-ray pulse generated inside a region optically thick to Compton scattering is spread and delayed as it diffuses outward. For a spherical cloud of radius R and uniform density n, a pulse $I(t) = I_0\delta(t)$ is spread so that

$$I(t)_{emergent} = I_0 \frac{c}{\pi 5/2 R\tau_{es}} (2u)^{-5/2} e^{-1/2u} , \qquad (1)$$

in the diffusion approximation $\tau_{es} \gtrsim$ few (Canizares 1976). The dimensionless time u is in units of the typical photon escape time $u = ct/R\tau_{es}$, where $\tau_{es} = Rn\sigma_{es}$. If a sinusoidal signal $I(t) = I_0(1 + f \cos\omega t)$ is input at the center of the cloud, the emergent signal is smoothed and delayed so that

$$I(t)_{emergent} = I_0 \{1 + f\, A\left(\frac{R\tau_{es}\omega}{c}\right) \cos [\omega t - \Phi\left(\frac{R\tau_{es}\omega}{c}\right)]\} , \qquad (2)$$

so that the pulsed fraction of the flux is reduced by the factor A. The functions $A(R\tau_{es}\omega/c)$ and $(R\tau_{es}\omega/c)$ are shown in Figure 2. To reduce a signal originally 100% pulsed (f=1) to the < 8% modulation observed for Cyg X-2, we require $R\tau_{es}\omega/c > 21$, or

$$\frac{R_8\tau_{es}}{P_3} > 1 , \qquad (3)$$

Figure 2

Smoothing functions $A(\omega')$ and $\Phi(\omega')$, where $\omega' \equiv \frac{R\tau_{es}\omega}{c}$.

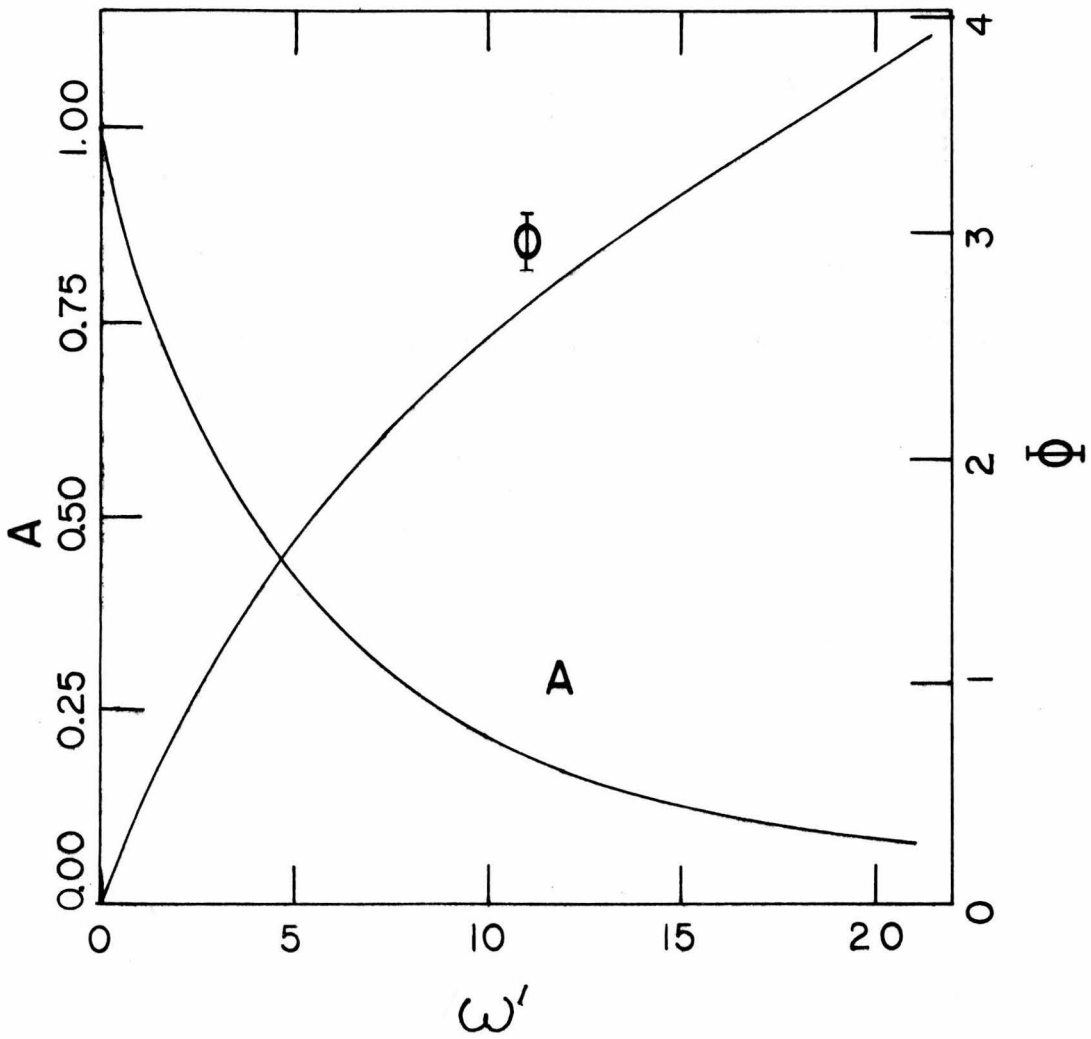

Figure 2

where $R_8 = R/10^8$ cm and $P_3 = P/10^{-3}$ seconds. A lower limit to the optical depth of the cloud $\tau_{es} \geq 2\text{-}3$ is set because unscattered photons would show the intrinsic pulsations attenuated by the factor $e^{-\tau_{es}}$.

The low value of low energy absorption observed in the spectrum of Cyg X-2 indicates that photoelectric absorption in the Compton scattering region must be suppressed below that expected for cool matter. The presence of X-ray flux at 1 keV indicates that oxygen, the predominant absorber at that energy, must be almost completely ionized. An even more severe constraint on the ionization state of the scattering region is set by the absence of a feature at the iron K edge (7.1 keV). There is no evidence in the spectrum obtained during flight 26.038 for emission or absorption at the iron edge. We may assume conservatively that the effective optical depth to photoelectric absorption by iron in the cloud

$$\tau_{eff} = \tau_{pe}\ (8\ \text{keV})\ \tau_{es} < 1, \tag{4}$$

where τ_{pe} is the optical depth to photoabsorption of the cloud, $\tau_{pe} = Rn\sigma_{pe}$.

The low value of photoelectric absorption thus required can be achieved only when most of the iron is completely stripped of electrons. We thus consider only the ionization states Fe XXVI and Fe XXVII, assuming that the abundance of other species is negligible. For matter with normal cosmic abundances,

$$\frac{\tau_{pe}(8\ \text{keV})}{\tau_{es}} = 0.50\ f\ , \tag{5}$$

where

$$f = \frac{n_{26}}{n_{26} + n_{27}}$$

(n_{26} and n_{27} are the number densities of Fe XXVI and Fe XXVII.) Equations (4) and (5) imply

$$f < \frac{2.0}{\tau_{es}^2} \quad . \tag{6}$$

Photoionization is the dominant mechanism of ionization in the region around an X-ray source (Hatchett, Buff, and McCray 1976). The equilibrium ratio n_{26}/n_{27} is determined by equating ionization and recombination rates

$$\frac{n_{26}}{4\ r^2} \int_{7.1\ \mathrm{keV}}^{\infty} \frac{L(E)}{E}\, \sigma(E)dE = n\ n_{27}\ \alpha$$

where L(E) is the X-ray source luminosity, $\sigma_{pe}(E)$ is the cross section to photoionization of Fe XXVI, and α is the recombination rate of Fe XXVII in $cm^3\ sec^{-1}$. The observed luminosity $L_{obs}(E)$ is softer and less ionizing than the flux in the inner regions of the scattering cloud, since the X-ray spectrum loses energy to the electrons as it propagates outward. An upper limit to the ionizing luminosity L(E) anywhere in the cloud can be estimated by assuming that the input spectrum has the same form as the spectrum of an X-ray pulsator. For Her X-1, $dN/dE \sim E^{-1}$ for 1 keV < E < 25 keV (Holt et al. 1974). We assume for Cyg X-2 an upper limit spectrum of $dN/dE = CE^{-1}$ normalized to the observed flux at 1 keV. For $\alpha = 2.0 \times 10^{-8}\ T^{-0.5}\ cm^3\ sec^{-1}$

(Allen 1973), equation (7) can be evaluated

$$\frac{n_{26}}{n_{27}} = 2.5 \times 10^{-32}\ nR^{2}L_{36}^{-1}T_{6}^{-1/2}\ , \tag{8}$$

where L_{36} is the observed source luminosity for E > 0.5 keV in units of 10^{36} ergs sec^{-1} (the flux observed in this experiment implies $L_{36} = 2.3(d/1\ kpc)^{2}$). Cathey and Hayes (1968) conclude that if the G-type star which produces the absorption lines in the optical spectrum of Cyg X-2 is a main sequence dwarf or a subdwarf, 570 pc < d < 940 pc. T_6 is the cloud temperature in units of 10^6 °K. Since $nR = 1.5 \times 10^{24}\ \tau_{es}$,

$$\frac{n_{26}}{n_{27}} = 0.068\ R_{8}\tau_{es}L_{36}^{-1}T_{6}^{-1/2}\ . \tag{9}$$

For the small value of f required by (6), f can be approximated by n_{26}/n_{27}, so that equations (6) and (9) can be combined

$$R_{8} < 30\tau_{es}^{-3}L_{36}T_{6}^{-1/2}\ . \tag{10}$$

The photoionization upper limit on scattering cloud radius (10) and the smoothing function lower limit on radius for a given pulsation period (3) can be combined to set an upper limit to the period of a pulsed X-ray source imbedded in the cloud:

$$P < 30ms\ (\tau_{es}^{-2}L_{36}T_{6}^{-1/2}). \tag{11}$$

A source of longer pulse period, embedded in a cloud small enough that iron could be substantially photoionized, would have to show observable pulsations.

The upper limit to P set by (11) is a factor of $25/\tau_{es}^{2}$ less than the period of the fastest known X-ray pulsator, SMC X-1. Serious theoretical objections exist to accretion onto such a rapidly rotating object (F. Lamb, private communication). It is thus not likely that Cyg X-2, and, by analogy, the other soft unpulsed X-ray sources, differ from the X-ray pulsators only by the presence of a scattering cloud about the neutron star. Pulsations of the neutron star may be intrinsically not present if there is not a strong magnetic field offset from the rotational axis channeling the accretion flow.

The lack of pulsations from Cyg X-2 observed in this experiment confirms the phenomenological identification of that source as a member of the class of soft unpulsed X-ray sources. The featureless spectrum observed places severe constraints on a model of those sources as "X-ray pulsators in a cloud." It appears likely that, if the non-pulsating sources contain neutron stars, they are intrinsically different, perhaps because of changes in the neutron star on an evolutionary time scale, from the hard X-ray pulsators found in early-type binaries.

CHAPTER 3

PHOTOMETRY OF AM HERCULIS: A SLOW OPTICAL PULSAR?

I. INTRODUCTION

AM Herculis, originally classified as a semiregular variable by Meinunger (1960), was found to have an old nova-like spectrum by Bond and Tifft (1974). Berg (1975) reported rapid photometric variability of the object. A bright variable soft X-ray source was discovered by Hearn, Richardson, and Clark (1976) near the position of the star. After the discovery by Cowley et al. (1976) of photometric and radial velocity variations, and by Tapia (1976) of linear polarization events, all showing a 3.1^h period, the identification of a modulation of the X-rays at the same period confirmed the identify of AM Her with the X-ray source (Hearn and Richardson 1977). Analysis of OSO-8 observations by Swank et al. (1977) revealed that the bulk of the observed system luminosity appears as hard X-rays in the 2-60 keV region. The early findings prompted independent observational research of the system by various groups. We present here results of multicolor photoelectric monitoring of the system during late spring, summer, and fall 1976.

II. OBSERVATIONS

Observations were made at the Mt. Wilson and Palomar Observatory 1.5 meter telescopes. All magnitudes presented here are based on differences between the variable and a comparison star, AM Her W, located approximately 9^s W and 80" N of AM Her. Mean magnitudes and colors of AM Her W are V = 12.20, U-B = 0.05, B-V = 0.58, and V-R = 0.54. Multicolor photometry was performed by sequential integrations in a three or four filter cycle. It was thus necessary to interpolate the raw counting rate for each filter to an intermediate time in order to reduce the

measurements to the UBV system or the UBVR system of Sandage (1973). Variability on time scales less than the filter cycle (30-40 s) has thus been smoothed out.

Figure 1 shows the V light curve for AM Her for seven telescope runs from 1976 May through November. Observations taken before 1976 October were acquired in one or two hour spans rather than through a full cycle. However, data can be phased together to form a composite light curve of each run. The period used was determined by fitting the times of minima of Berg (1976), Olson (1977), Szkody and Brownlee (1977), and the present data to a constant period. A least-squares fit leads to the period $P = 0.128928 \pm 0.000001$ days (one sigma error). The epoch used is that of the linear polarization event (Tapia 1977): HJD 2443014.765.

III. LIGHT AND COLOR CURVES, AND FLARES

The light curve shows periodic variability, including a deep, broad primary minimum centered at $\Phi = 0.56$ P and, in some cases, a secondary minimum at $\Phi = 0.11$ P (Fig. 1). These periodic effects become larger with increasing wavelength (Fig. 2). It can be seen that the system becomes bluer during both primary and secondary minima (Fig. 3). The secondary minimum is coincident with the X-ray eclipse observed by Hearn and Richardson (1977) during 1976 May 21-22. It also agrees very well with the phase ($\Phi = 0.03 - 0.24$ P) of a standstill in the circular polarization curve (Tapia 1977). The primary minimum is concurrent with another standstill ($\Phi = 0.45 - 0.66$ P) of the polarization curve, at which time the amount of circular polarization in the V band goes to a value near zero. No X-ray minimum has been observed at this phase.

Figures 1-4

V, R, B-V, and U-V magnitudes and colors of AM Her folded modulo P = 0.128928 d. Phase Φ = 0.00 is that of the linear polarization event (Tapia 1977): HJD 2443014.765.

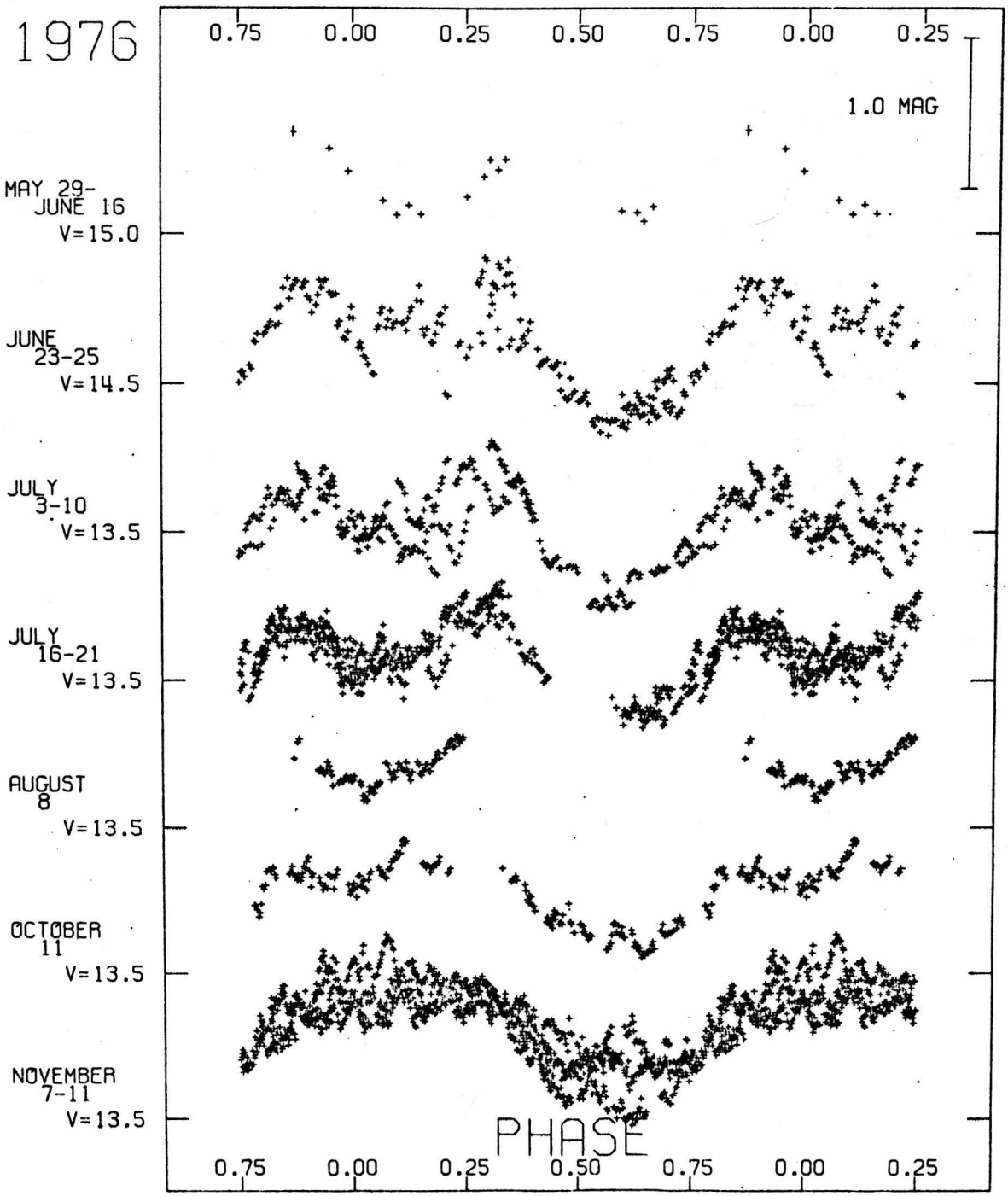
1976
0.75
0.00
0.25
0.50
0.75
0.00
0.25
1.0 MAG
MAY 29-
JUNE 16
V=15.0
JUNE
23-25
V=14.5
JULY
3-10
V=13.5
JULY
16-21
V=13.5
AUGUST
8
V=13.5
OCTOBER
11
V=13.5
NOVEMBER
7-11
V=13.5
PHASE
0.75
0.00
0.25
0.50
0.75
0.00
0.25

Figure 1

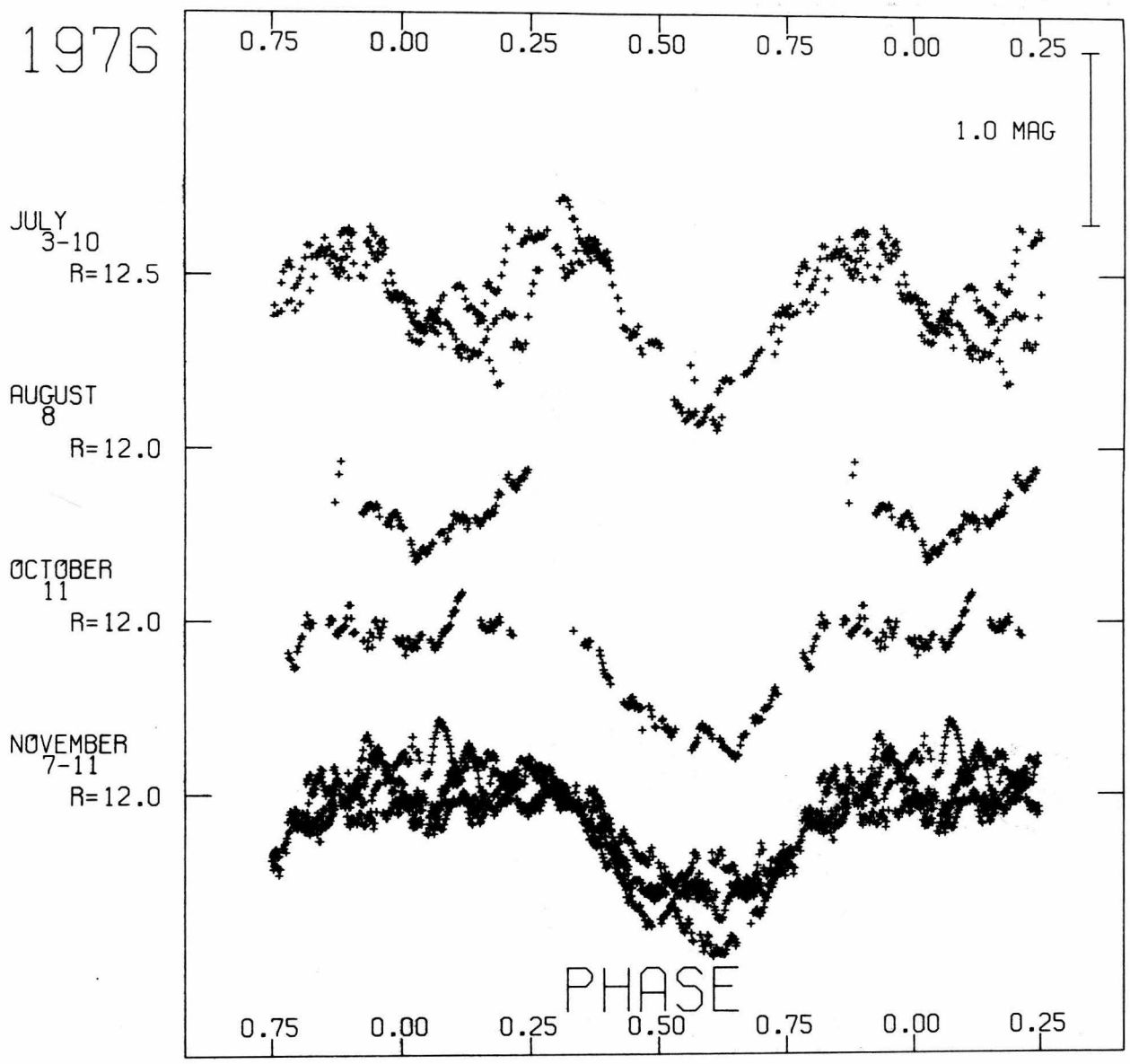
1976
0.75
0.00
0.25
0.50
0.75
0.00
0.25
1.0 MAG
JULY
3-10
R=12.5
AUGUST
8
R=12.0
OCTOBER
11
R=12.0
NOVEMBER
7-11
R=12.0
PHASE
0.75
0.00
0.25
0.50
0.75
0.00
0.25

Figure 2

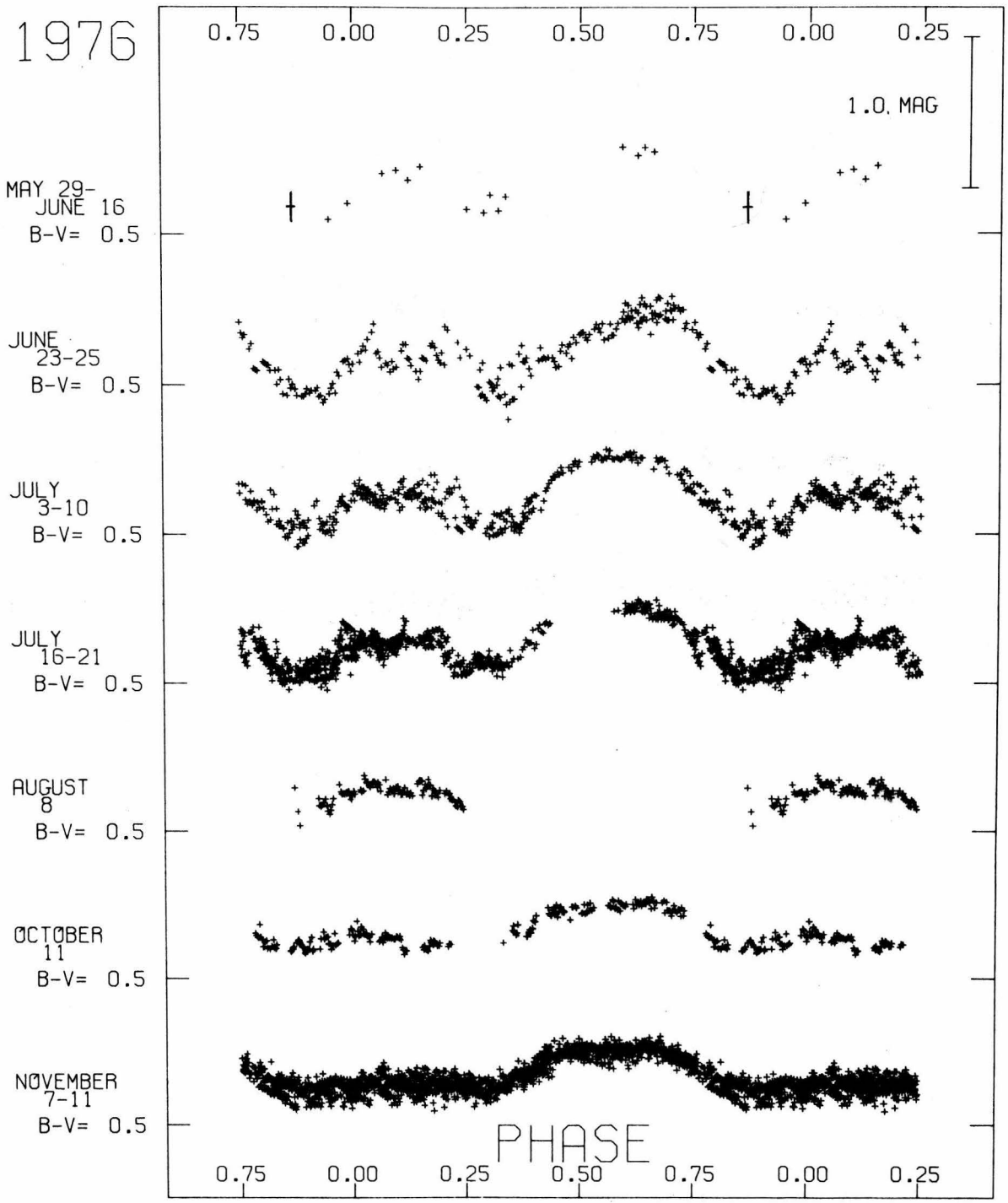
1976
0.75
0.00
0.25
0.50
0.75
0.00
0.25
1.0. MAG
MAY 29-
JUNE 16
B-V= 0.5
JUNE
23-25
B-V= 0.5
JULY
3-10
B-V= 0.5
JULY
16-21
B-V= 0.5
AUGUST
8
B-V= 0.5
OCTOBER
11
B-V= 0.5
NOVEMBER
7-11
B-V= 0.5
PHASE
0.75
0.00
0.25
0.50
0.75
0.00
0.25

Figure 3

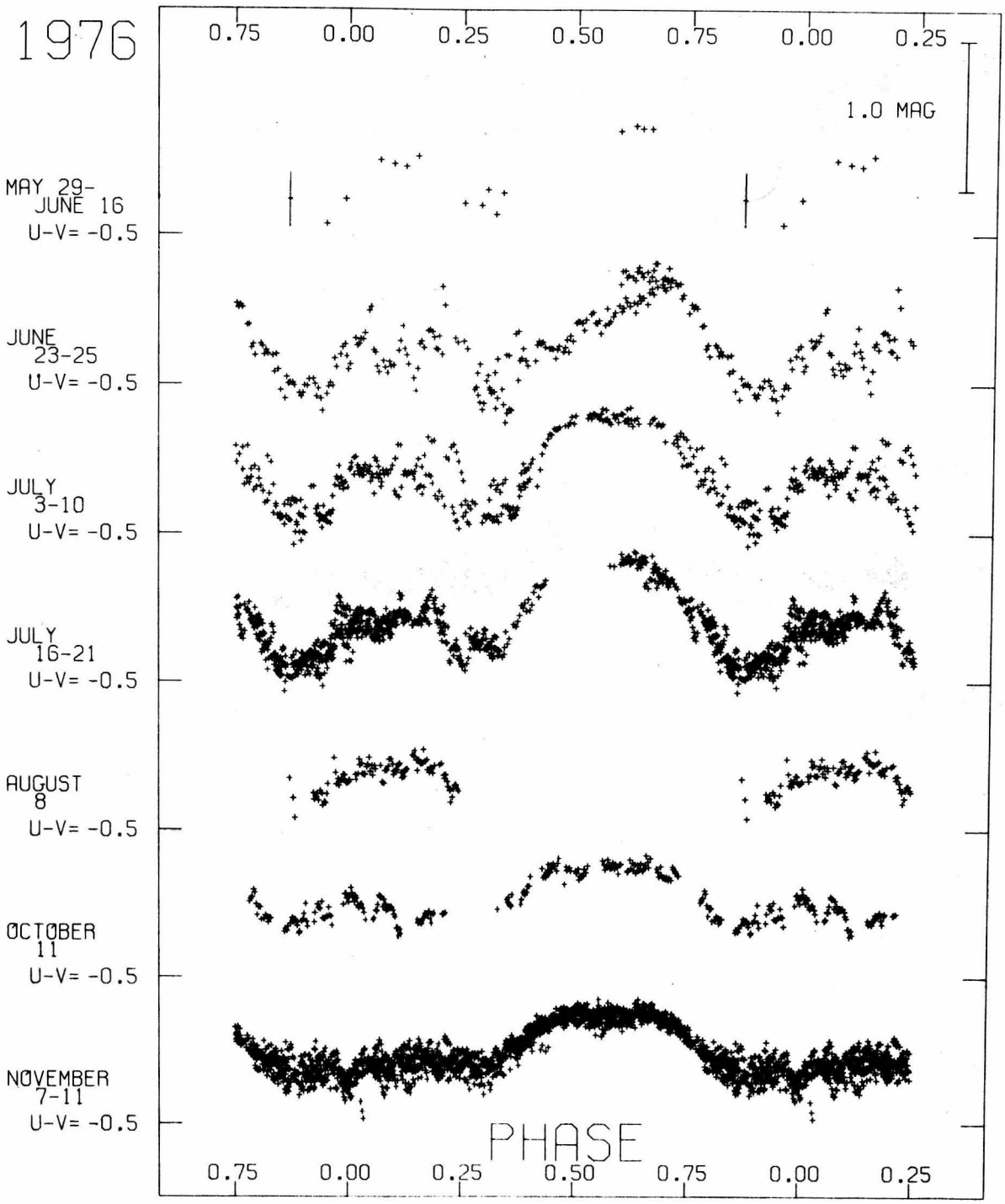
1976
0.75
0.00
0.25
0.50
0.75
0.00
0.25
1.0 MAG
MAY 29-
JUNE 16
U-V= -0.5
JUNE
23-25
U-V= -0.5
JULY
3-10
U-V= -0.5
JULY
16-21
U-V= -0.5
AUGUST
8
U-V= -0.5
OCTOBER
11
U-V= -0.5
NOVEMBER
7-11
U-V= -0.5
PHASE
0.75
0.00
0.25
0.50
0.75
0.00
0.25

Figure 4

The light curve of the system shows an evolution from 1976 May to November. There is a general increase in brightness in all spectral bands of about 1.5 - 2 magnitudes. The U-V color at the primary and secondary minima remains remarkable constant during the overall increase of magnitude of the system (Fig. 4). The B-R color becomes slightly bluer ($\lesssim$ 0.2 mag) between the July and November epochs.

The color curves (B-V and U-B versus phase) show substantially less scatter than the magnitude curves. Not only is there less flickering activity apparent in the colors, but the color variation repeats regularly from cycle to cycle as Berg has reported (Berg 1976). The regular shape of the color curves promises very accurate determination of the photometric period of AM Her as the epoch of observations is extended.

Soft X-ray observations with the SAS-3 satellite were made in 1976 May immediately before the first run of data and simultaneously in 1976 November with the last run of data (Richardson and Priedhorsky 1977). The later X-ray observations show an increase in flux over the May data by a factor of approximately 2 (Hearn 1977). During the course of the observations, the secondary minimum disappeared in the V and B-V data and became very reduced in amplitude in V-R. The lack of the secondary minimum is accompanied by the disappearance of the X-ray eclipse (Hearn, Richardson, and Clark 1977) and by disappearance of the secondary standstill (at $\phi \sim 0.14$ P) in the circular polarization (Michalsky, Stokes, and Stokes 1977).

AM Her shows rapid nonperiodic variability in all four wavelength regions. Some of the variability is sufficiently well defined to be measured as discrete flares. Typical flare behavior is shown in Figure 5.

Figure 5

Flare activity of AM Her compared with that of the cataclysmic variable AE Aqr. 6^h UT 1976 July 10 is $\Phi = 0.85$ P.

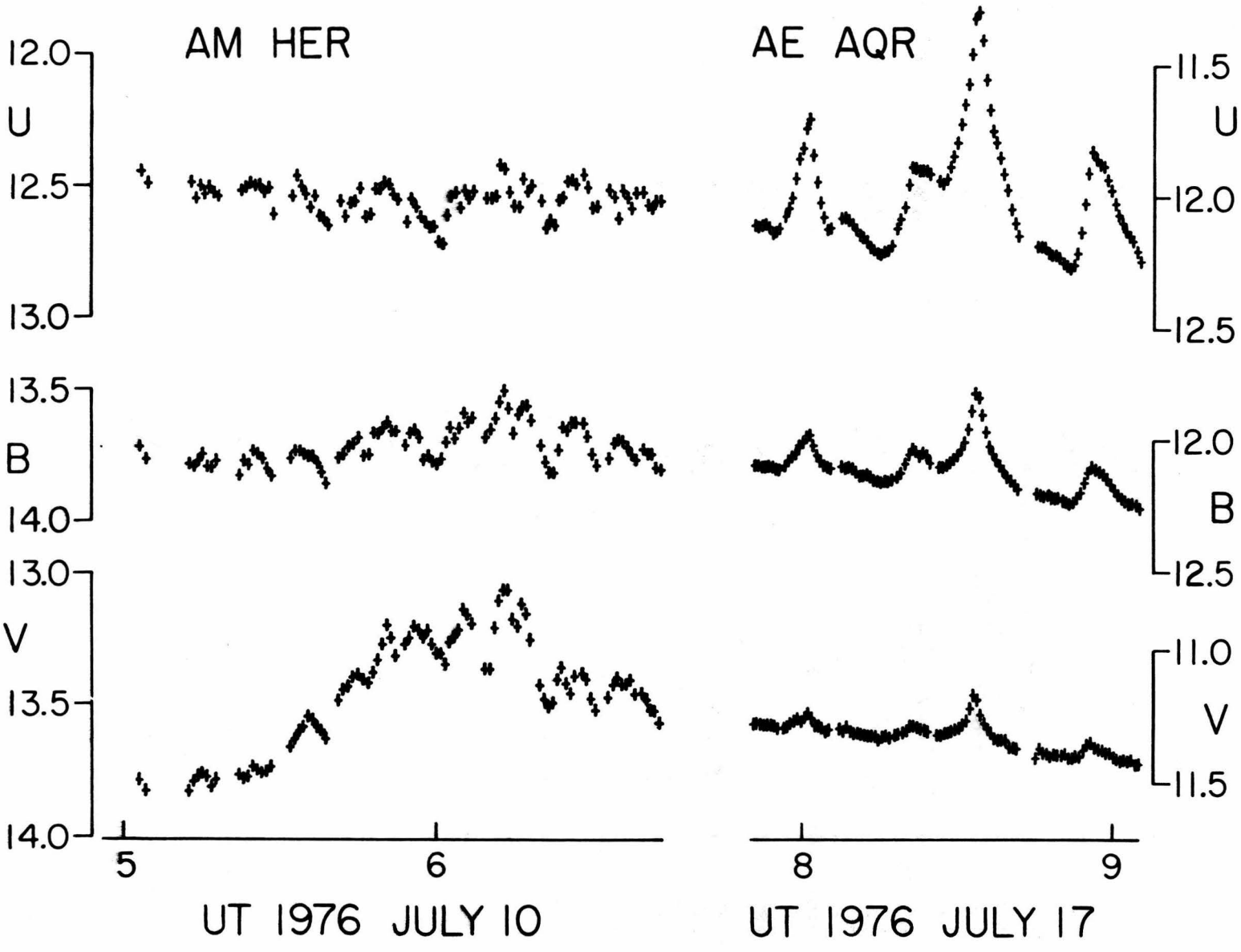
AM HER
AE AQR
12.0
U
12.5
13.0
13.5
B
14.0
13.0
V
13.5
14.0
11.5
U
12.0
12.5
12.0
B
12.5
11.0
V
11.5
5
6
8
9
UT 1976 JULY 10
UT 1976 JULY 17

Figure 5

The intrinsic color of the excess flux emitted during the flares is often very red, ranging up to B-V = 1.2. AE Aqr and SS Cyg, common cataclysmic variables which show rapid flaring activity (i.e., flickering), were measured as a comparison. They showed average flare colors of B-V of -0.1 and 0.0,respectively. Besides being intrinsically red, the flares tended to be redder than the total light of the system, which was never observed to be redder than B-V = 0.6. It is difficult to pick out such flares in the B-V light curve because of the relatively small amplitude, $\sim$ 0.2 mag, of the flares, and the intrinsic scatter of the color curve.

A catalog was made of 38 flares which appeared on inspection (independently by the two authors) to show well-defined peaks and baselines, so that the color of the light emitted in the flare could be determined. The one sigma error in $(B-V)_{flare}$, determined by the scatter between two independent measurements of the color of the flares, was less than 0.15 mag. The catalogued flares were much less common during the primary minimum than outside it. Of the 38 flares, only 8 fell within the primary minimum (between ϕ = 0.36 P and 0.76 P). Those flares which are present at the primary minimum tend to be bluer (with respect to the baseline color) than average. Of 12 well-defined flares in the 1976 June - July data which were intrinsically more than 0.2 mag redder in B-V than the total light of the star, only one fell within phase 0.36 to 0.76. The fast flickering behavior is thus distinguished by an unusual component of very red flare activity which avoids the primary minimum.

IV. INTERPRETATION OF THE LIGHT CURVE

Any physical model of the AM Her system should explain the periodic variability prominent in the V and R bands. In the following section we would like to discuss possible mechanisms for this modulation. In order to do so, it is first necessary to understand the source of V and R flux.

There are several indications that the source of the circular polarization in the AM Her system is also the major contributor to the flux in the visual and red region: (1) Both the secondary and primary photometric minima coincide with standstills in the circular polarization curve of Tapia (1977). The standstills probably correspond to attenuation of the circular polarization source. (2) The red flares which distinguish this system tend not to occur at the primary minimum, which is the major polarization standstill. (3) There is a striking similarity between the red color of the flares, the color (B-V $\sim$ 1 1/4, V-R $\sim$ 1) of the light which is absent at the minima (as evidenced by the departure to the blue of B-V and V-R indices at these phases), and the color dependence of the circular polarization (Tapia 1977; Stockman 1977; Michalsky, Stokes and Stokes 1977). It follows therefore that the behavior of the visual and red light curve is to be explained at least in part by the modulation of the flux from the same source that is responsible for the circular polarization.

The flux at wavelengths less than 4500 Å shows little polarization (Stockman 1977) and must be identified with a light source other than the circular polarization source. That the two sources are powered by the same mechanism is suggested by the identical rise of the U and V magnitudes of AM Her from 1976 May through November. The variation of U-V color

through the binary cycle, however, indicates that the two sources must have different locations in the system. The scatter in the U-V color curve decreases by a factor of ~ 2 at primary minimum. This indicates that the portion of the V flux uncorrelated with the ultraviolet source decreases markedly during the primary minimum. The lack of correlation of the U flux with that in the V band is also demonstrated by the scatter in phase of the shallow (0.2 - 0.4 mag) minimum in the U band with respect to the phase of the V light curve. In the last six runs of 1976 data presented, the U minimum falls successively at $\Phi \sim 0.5$, 0.9, 0.9, 0.0, 0.7, and 0.7 P. These considerations imply that the flux from AM Her consists of a blue, unpolarized component, which is relatively constant, and a red, partially polarized component which shows primary and secondary minima. We discuss below possible mechanisms for that modulation.

a) Heating Effect?

The periodic variation of radial velocity observed in the emission lines has been interpreted to mean that AM Her is a binary system (Cowley and Crampton 1977; Priedhorsky 1977). We assume that AM Her is a semi-detached, close binary system which, although showing significant differences (e.g., Cowley 1976), closely mimics cataclysmic variable (CV)-type stars. It exhibits mass transfer with subsequent mass accretion as the primary powering source for the system. The secondary mass losing component thus fills its critical equipotential surface. We assume that the primary star is a magnetic degenerate dwarf (Tapia 1977 ; Swank *et al.* 1977). The facing

side of the secondary might be heated by the primary so that the changing aspect of that hot side through the binary cycle causes the observed modulation.

If the secondary fills its Roche lobe and does not deviate drastically in structure from the single, late-type main sequence stars, then its mass $M_2 \approx 0.4\ M_\odot$ on the basis of the relationship between orbital period and the mass of the secondary (Faulkner 1971; Robinson 1976; Ritter 1976). From the mass - radius relationship for main sequence stars, $r_2 \sim 0.4\ R_\odot = 2.8 \times 10^{10}$ cm. Similar conclusions have been reached via slightly different arguments by Cowley and Crampton (1977) and Stockman et al. (1977). Given that the red star has $M_2 = 0.4\ M_\odot$ and that the mass of the primary is in the range 0.4 - 1.4 $M_\odot$, i.e., between less than a half of the average primary's mass for typical CV's (Robinson 1976) and the Chandrasekhar limit for moderately rotating white dwarfs, it follows from Kepler's law that the component separation a is in the range $7.0 - 9.1 \times 10^{10}$ cm. Warner (1976) derives the orbital period - luminosity relation for the secondary in CV's

$$M_{V,2} \simeq -12.5 \log P\ (\text{hours}) + 17.5$$

which implies for AM Her $M_{V,2} \simeq 11.4$. If one reasons as Chanmugam and Wagner (1977) that the brightness of AM Her at minimum, $V \sim 15$, corresponds to $\langle M_V \rangle = +7.5$ as for dwarf novae at minimum (Kraft and Luyten 1965), then the distance is $d \sim 300$ pc. For $d \gtrsim 100$ pc, $m_{V,2} > 16.4$ mag so that the secondary star is not intrinsically a major source of light even at minimum.

The secondary subtends a fraction of solid angle viewed from the primary of $0.020 < \frac{\Omega s}{4\pi} < 0.035$ for $0.3 < q < 1.0$ ($q = M_2/M_1$). If the flux from the X-ray source, circular polarization source, and any possible disk is not beamed, the fraction of that flux which can be intercepted and reradiated by the secondary is not greater than ~ 4 percent. In 1976 November, we observe that f_{max} (0.3-0.8 μm) $\sim 1.6 \times 10^{-10}$ ergs cm^{-2} sec^{-1}. When the system was at a similar optical magnitude in 1975 October (Berg and Duthie 1977), the observed system luminosity was dominated by a 2-60 keV flux of 7.6×10^{-10} ergs cm^{-2} sec^{-1} (Swank et al. 1977). Reprocessed X-rays can thus explain only $\lesssim$ 20 percent of the observed optical luminosity. It should be noted that no heating effect has ever been observed in any other CV, including the soft X-ray source SS Cyg.

If the excess optical flux at maximum comes from a heated stellar photosphere, one might expect to see an absorption line spectrum, as in the case of HZ Her. However, high dispersion spectroscopy taken in 1976 October shows no evidence for the absorption line spectrum of a cool star (Greenstein 1977).

The color of the flux absent at the primary minimum (B-V $\gtrsim$ 1 1/4) indicates that, if the minimum results from an aspect effect, the "hot" side of the secondary is actually rather cool, of spectral class K5 or later. A star of uniform spectral class K5 which provides the flux absent at primary minimum would have $r_2 \sim 1.1\ R_\odot\ (\frac{d}{300\ pc})$, which for $d > 100$ pc would be larger than the size of the secondary expected from the orbital period - mass - radius relationship. This calculated radius must be considered a lower limit, since, as in the case of HZ Herculis, the "hot" side would extend over less than a hemisphere of the star (Oke 1976). The substantial flickering seen in the red component of the flux may also argue against a heating-aspect effect.

b) Stellar Eclipses?

Neither the primary nor the secondary minimum of the AM Her system is easily identified with an eclipse by the secondary of another component of the system. The primary minimum is very broad, with a full width at half maximum (FWHM) in B-V of $\Delta\Phi = 0.37\ P \pm .01$ and a corresponding full width $\Delta\Phi = 0.51\ P \pm .02$. One finds (Kopal 1959) that even for a contact binary system at inclination $i = 90^{o}$, the maximum possible eclipse duration is 0.32 P. This conclusion is valid for almost any value of q. Chanan, Middleditch, and Nelson (1976) show that for any $q < 100$, the maximum full width of an eclipse $\Delta\Phi < 0.37\ P$. For the range of q and a determined above, the maximum full width at half maximum of an eclipse by the secondary of an object centered at the primary is

$$0.09\ P < \Delta\Phi_{max} < 0.12\ P.$$

Over the same range of parameters, the maximum full width of an eclipse by the secondary of a disk filling the Roche lobe of the primary is:

$$\Delta\Phi_{max} = 0.205\ P \pm .005.$$

The secondary minimum is also unlikely to be an eclipse phenomenon. The disappearance of the secondary in V and B-V after 1976 October, and the chaotic color activity at its bottom argue against an eclipse origin. Onset of the secondary seems also to wander in phase. The secondary is quite wide, with a FWHM of $\Delta\Phi = 0.26\ P \pm .01$ and a full width of $0.33\ P \pm .01$.

We conclude that an eclipse by the secondary star of the primary or inner disk around the primary may be dismissed from any appreciable role in the light curve of the AM Her system. Since there is thus no clear relation between the phase of conjunction and photometric phase, it is difficult to establish the relative position of various components of the system, including the region of the emission line formation.

c) Hot Spot Effects?

The equivalence between the 3.1^h polarization period of AM Her, which manifests the rotation period of the magnetic white dwarf, and the binary period indicated by the emission line radial velocity variation indicates that the white dwarf is locked into synchronous rotation with the orbital period. Accretion of mass onto the white dwarf would quickly spin up the white dwarf unless there exists an opposing torque to maintain synchronism.

The matter transferred from the secondary in cataclysmic binaries typically forms an accretion disk about the primary. The strong magnetic field required to produce the circular polarization in AM Her will certainly exclude a disk from the region closest to the white dwarf. The inner boundary of a disk, at which point matter must go into synchronous rotation with the white dwarf, will be found at the distance r_A where the pressure of the magnetic field is comparable to the ram pressure of the matter circulating in the disk (see, for instance, Lamb, Pethick, and Pines 1973):

$$\rho v(r_A)^2 \sim \frac{B^2(r_A)}{8\pi} \quad .$$

We assume a dipole field with a polar value at the white dwarf of 2×10^8 gauss in order to produce the observed circular polarization. For Keplerian velocities, $v_{disk} = \left(\frac{GM_1}{r_A}\right)^{1/2}$,

$$r_A = 8.1 \times 10^9 \ (M_1/M_\odot)^{-1/5} \ (\rho_8)^{-1/5} \ (r_9/0.7)^{6/5} \ \text{cm}$$

where ρ_8 is the density of the disk and $r_9 = 0.7$ is a typical radius for a 1 $M_\odot$ white dwarf.

Stockman et al. (1977) conclude from the observed Hα/Hβ line ratios and the lack of Stark blending of H13 and H14 that the density of the emission line region falls in the range $1.6 \times 10^{-11} < \rho < 3 \times 10^{-10}$ g cm^{-3}. It is characteristic of "normal" CV's that the emission lines are formed in a "chromosphere" above the disk of density $\sim 1.6 \times 10^{-12}$ g cm^{-3} Warner (1976). The chromosphere is much more tenuous than the optically thick disk, which is possibly at least as dense as 10^{-8} g cm^{-3}. r_A is quite insensitive to ρ. It is thus entirely possible that a disk similar to these in other cataclysmic variables exists in the AM Her system with a minimum radius of about ten times the white dwarf radius. This disk may contribute substantially to the flux in the blue and ultraviolet. Although the disk will exclude the magnetic field in the equatorial plane of the system, it may be possible for magnetic flux to escape at the poles and lock the rotation of the white dwarf to that of the secondary star.

In CV's the light curve is often dominated by a hot spot caused by the collision of the stream of matter transferred from the cool star with the accretion disk about the primary. The changing aspect of the spot with binary phase can cause a large "hump" in the light curve. The very red color of the excess flux associated with the maximum in the V and R bands in the AM Her system is unlike the color of the hot spot in any CV. It is possible, however, that the periodic variation of the ultraviolet flux has a hot spot origin.

We would next like to consider the possibility that a thickened region of the disk at a hot spot periodically eclipses the primary to cause one or another of the minima in visual and red light. In order to obscure the white dwarf region for the full duration of even the secondary eclipse,

the hot "spot" must extend over 120° of the disk circumference. Hot spots in other CV's are much more localized, the largest in Z Cha (Warner 1974) extending only 20° around the disk. A hot spot of that angular extent located at r_H from the primary must have area $A > 2\ (\frac{120^{\circ}}{360^{\circ}})\ 2\pi\ r_H\ (\cos i\ r_H)$. An upper limit to i is set by the requirement that the secondary not eclipse the primary and the disk immediately around it. It is necessary that $i < i_{max}$, where $68^{\circ} < i_{max} < 73^{\circ}$ for $0.3 < q < 1.0$ and $r_2 = 0.4\ R_{\odot}$.

If the hot spot were located near the edge of the primary critical equipotential lobe, had optical depth $\tau \gtrsim 1$ (required to cause an eclipse), and had a typical hot spot temperature of $3 \times 10^4\ ^{\circ}K$, it would have a bolometric luminosity $L > 8 \times 10^{34}$ ergs sec^{-1} for $0.3 < q < 1.0$. The luminosity of such a spot would be greater than the luminosity of the system at frequencies less than 1 keV (Stockman et al. 1977) if $d < 1000$ pc. There is, in fact, no evidence in the light curve for a hump in the U or B bands at either minimum as would be expected at the conjunction of a hot spot. The very regular width and shape of the primary minimum in B-V argues against it being obscuration by something as potentially variable as a hot spot.

d) A Possible Model

It has been shown above that the source of most of the red flux may be the same as that for the circularly polarized radiation, which must originate in the immediate vicinity of the white dwarf primary. Since we have not explained the 3.1^h modulation of the red flux by the effect of other components of the system, we look for a source of modulation intrinsic to the primary.

As described in Chapter III, the secondary and primary minima differ because of the presence of an X-ray minimum at the secondary in the 1976 May data. We conclude that the secondary and primary minima are qualitatively different. The secondary involves a conjunction of the X-ray and circularly polarized optical sources, while at the primary the two sources are not in line.

Stockman et al. (1977) suggest that cyclotron radiation from AM Her is produced in an accretion column close to the surface of the white dwarf, while the soft X-rays are produced higher in the column. Optically thin cyclotron radiation must occur at wavelength $\lambda_c = \frac{2\pi c}{\omega_c} = \frac{2\pi c^2 m_e}{eB}$ where ω_c is the cyclotron angular frequency. The presence of circular polarization at 4500 Å (Stockman 1977; Michalsky, Stokes, and Stokes 1977) implies a polar field $B_{max} \sim 2.5 \times 10^8$ gauss. For a dipole field centered at the middle of the white dwarf, the field at 0.2 r_{wd} above the surface has fallen (as r^{-3}) to 1.45×10^8 gauss, so that λ_c is 7400 Å. Cyclotron radiation in the optical band from AM Her is thus limited to a thin cap over the pole of the white dwarf. It seems entirely likely that such a low-lying source may be eclipsed by the body of the white dwarf (Fig. 6). It is also possible to produce very wide eclipses in this fashion. The greater height above the surface of emission at longer wavelengths leads to a qualitative prediction that the primary minimum will be shorter at longer wavelengths. This effect may be discerned in the V and R light curves of Figures 1 and 2, and in the V, I, and 8600 Å data of Olson (1977).

If the cyclotron source was divided between two opposite poles, there would never be more than a partial eclipse of the whole cyclotron region by the white dwarf. However, a displacement of the dipole toward

Figure 6

Geometrical model of the X-ray and circularly polarized optical emission regions near the degenerate dwarf in the AM Her system. $\vec{\mu}$ is the dipole moment of the dwarf, which may be displaced from the center of that star.

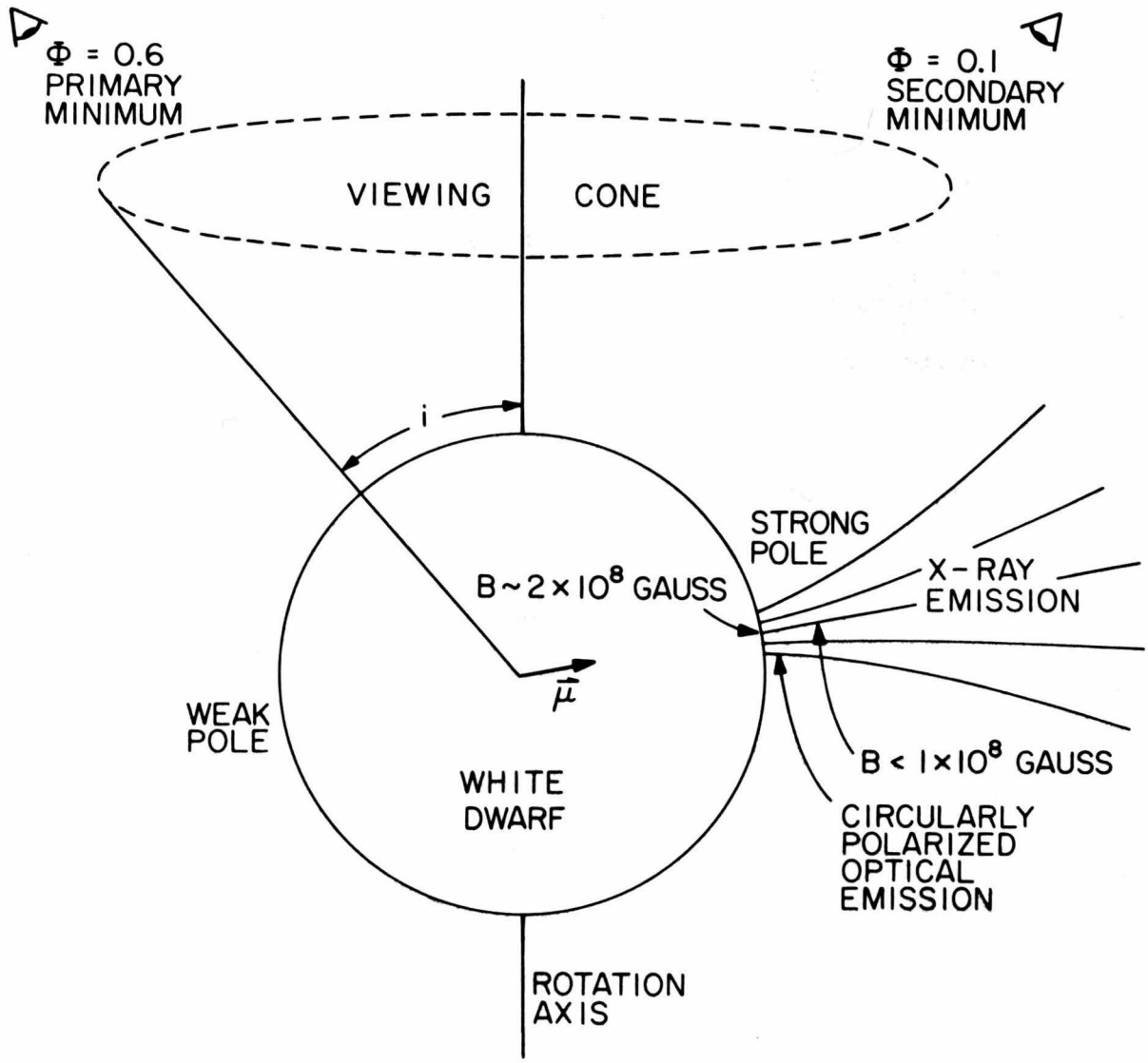
Φ = 0.6
PRIMARY
MINIMUM
Φ = 0.1
SECONDARY
MINIMUM
VIEWING
CONE
i
STRONG
POLE
B ~ 2 × 10⁸ GAUSS
X-RAY
EMISSION
WEAK
POLE
WHITE
DWARF
B < 1 × 10⁸ GAUSS
CIRCULARLY
POLARIZED
OPTICAL
EMISSION
ROTATION
AXIS

Figure 6

one pole might limit the cyclotron source to one pole. For a displacement of 0.2 r_{wd}, $\lambda_{c\ min}$ = 4500 Å at the strong pole implies $\lambda_{c\ min}$ = 1.44 μm, well out of the optical band, at the weaker pole.

The primary minimum is thus the point at which the polar cap is most distant from the sub-earth point. At 0.50 P later, the cap and accretion column are closest to the sub-earth point so that the X-ray source and cyclotron source may be nearly in line. Self-absorption when the column is viewed lengthwise could cause the secondary minimum in the X-ray and circularly polarized optical flux. The activity in B-V at the secondary minimum indeed suggests obscuration by a variable, partially transparent object. The disappearance of the secondary minimum would require that the column became optically thin after 1976 October. The higher temperature of the X-rays observed in 1976 November (Hearn, Richardson and Clark 1977) also suggests a thinning of the column.

The primary and secondary minima should correspond to circular polarization minima and maxima (except for the occultation of the polarization source) as the angle between the viewing direction and the magnetic field reaches extrema at these times. It is difficult to measure the exact position of circular polarization minimum and maximum because of the standstills at both times. The polarization maximum ($\Phi = \sim 0.15$ P) is clearly at the expected phase. Though a polarization minimum is observed at $\Phi \sim 0.8$ P, the polarization standstill at $\Phi = 0.55$ P may conceal a true minimum at a phase as early as $\Phi \sim 0.6$ P.

In the model above, the phase relation between primary minimum and binary conjunction depends only on the polar direction of the white dwarf magnetic field. As that direction is not known, the relation between

photometric phase and emission line radial velocities, which represent motion in gas streams and/or disk outside the white dwarf magnetosphere, is arbitrary. Radial velocity observations (Priedhorsky 1977; Crampton and Cowley 1977) thus do not significantly constrain this model.

V. CONCLUSION

We observe no contribution to the visual and red light curve of AM Her by the secondary or hot spot. We have ruled out eclipses by either of these components as the origin of the primary or secondary minima. Indeed, it would be very unlikely for a system component as distant from the primary as a hot spot or secondary to graze the primary at just the right angle so as to occult the circularly polarized radiation but not the soft X-ray source (both of which must be located very close to the primary) during the primary minimum. Sufficient X-ray flux to drive the light curve via a heating effect has not been observed. However, the flux of AM Her above 60 keV is not yet known, and beaming of the X-ray flux may be possible.

Optical flux from the AM Her system seems to consist of at least two components, one of which is probably associated with the circular polarization source and is dominant in the V and R bands. Simultaneous photometric and polarimetric observations to confirm this association would be valuable. The other component, dominant at bluer wavelengths, may be associated with an accretion disk. The magnetospheric radius in the AM Her system to be expected from the estimated magnetic field strength and reasonable disk densities is well within the primary critical equipotential lobe, so that the existence of an accretion disk is possible. The near-constancy of U-V color during the increase in brightness of AM Her from

1976 May to November indicates that the blue and red components have the same power source. It is possible that they are both modulated by changes in the mass accretion rate.

We suggest that the red component of optical flux originates in a region of strong magnetic field in the immediate vicinity of the white dwarf. Because of the major role of the magnetic field in the emission process, and the clocking of the 3.1^{h} behavior of AM Her by the rotation of a degenerate object, we identify the source of red flux in the AM Her system as a slow optical pulsar.

REFERENCES

Allen, C. W. 1973, Astrophysical Quantities, Athlone Press, London, p. 97.

Arons, J. and Rothschild, R. 1975, GSFC Document X-661-75-230.

Berg, R. A. 1975, Bull. A.A.S., 7, 512.

Berg, R. A. 1976, presentation at Ann Arbor Symposium, 1976 October 29.

Berg, R. A. and Duthie, J. G. 1977, Ap. J., 211, 859.

Birsa, F. B., Glasser, C. A., Ziegler, M. M. 1972, 1.5 to 38 keV X-ray Experiment System for High Altitude Sounding Rockets, NASA preprint X-661-72-80.

Bisnovatyi-Kogan, G. S. and Blinnikov, S. I. 1976, Sov. Astron. (Letters), 2, 191.

Bleach, R. D., Boldt, E. A., Holt, S. S., Schwartz, Q. A., and Serlemitsos, P. J. 1972, Ap. J., 171, 51.

Boldt, E., Holt, S., Rothschild, R., and Serlemitsos, P. 1975, Proc. Int. Conf. X-Rays in Space, ed. D. Venketesan (University of Calgary).

Bond, H. E. and Tifft, W. G. 1974, Pub. A.S.P., 86, 981.

Bradt, H. and Matilsky, T. 1975, in Symposium on X-Ray Binaries, NASA SP-389, p. 317.

Bregman, J., Butler, D., Kemper, E., Koski, A., Kraft, R. P., and Stone, R. P. S. 1973, Ap. J. (Letters), 185, L117.

Brisken, A. F. 1973, thesis, University of Maryland.

Brown, R. L., and Gould, R. J. 1970, Phys. Rev. D., 1, 2252.

Canizares, C. R. 1976, Ap. J. (Letters), 207, L101.

Canizares, C. and Oda, M. 1977, Ap. J. (Letters), 214, L119.

Chanan, G. A., Middleditch, J., and Nelson, J. E. 1976, Ap. J., 208, 512.

Chanmugam, G. and Wagner, R. L. 1977, Ap. J. (Letters), 213, L13.

Coe, M. J., Engel, A. R., and Quenby, J. J. 1976, Nature, 259, 544.

Cowley, A. P. 1976, Eighth Texas Symposium on Relativistic Astrophysics, in press.

Cowley, A. P., and Crampton, D. 1975, Ap. J. (Letters), 201, L65.

Cowley, A. P., and Crampton, D. 1977, Ap. J. (Letters), 212, L121.

Cowley, A., Crampton, D., Szkody, P., and Brownlee, D. 1976, IAU Circ., No. 2984.

Crampton, D., and Cowley, A. P. 1977, preprint.

Cruddace, R., Bowyer, S., Lampton, M., Mack, J., and Margon, B. 1972, Ap. J., 174, 529.

Culhane, J. L., Mason, K. O., Sanford, P. W., and White, N. E. 1975, in Symposium on X-Ray Binaries, NASA SP-389, p. 1.

Eardley, D. M., and Lightman, A. P. 1976, Nature, 262, 196.

Elsner, R. F., and Lamb, F. K. 1976, Nature, 262, 356.

Faulkner, J. 1971, Ap. J. (Letters), 170, L99.

Garmire, G. P., and Ryter, C. E. 1975, Astrophysical Letters, 16, 121.

Giacconi, R., Gursky, H., Paolini, F., and Rossi, B. 1962, Phys. Rev. Letters, 9, 439.

Giacconi, R., Gursky, H., and Van Speybroeck, L. P. 1968, Annual Reviews of Astronomy and Astrophysics, 6, 373.

Giacconi, R., Murray, S., Gursky, H., Kellogg, E., Schreier, E., Matilsky, T., Koch, D., and Tananbaum, H. 1974, Ap. J. Supplement 237, 27, 37.

Gorenstein, P. 1975, Ap. J., 198, 95.

Gorenstein, P. 1976, Astrophysics and Space Science, 42, 189.

Gorenstein, P., Giacconi, R., and Gursky, H. 1967, Ap. J. (Letters), 150, L85.

Greenstein, J. L. 1977, private communication.

Gursky, H., Gorenstein, P., Kerr, F. J., and Grayzeck, E. J. 1971, Ap. J. (Letters), 167, L15.

Hatchett, S., Buff, J., and McCray, R. 1976, Ap. J., 206, 847.

Hearn, D. R. 1977, private communication.

Hearn, D. R., and Richardson, J. A. 1977, Ap. J. (Letters), 213, L115.

Hearn, D. R., Richardson, J. A., and Clark, G. W. 1976, Ap. J. (Letters), 210, L23.

Hearn, D. R., Richarson, J. A., and Clark, G. W. 1977, private communication.

Heise, J., Brinkman, A. C., Schrijver, J., Mewe, R., Bogende, A. den, Gronenschild, E., Parsignault, D., Grindlay, J., Schnopper, H., Schreier, E., and Gursky, H. 1975, Nature, 256, 107.

Holt, S. S., Boldt, E. A., Rothschild, R. E., Saba, J. L. R., and Serlemitsos, P. J. 1974, Ap. J. (Letters), 190, L109.

Holt, S. S., Boldt, E. A., Serlemitsos, P. J., and Kaluzienski, L. J. 1976, Ap. J. (Letters), 205, L143.

Illarionov, A. F., and Sunyaev, R. A. 1972, Soviet Astronomy-AJ, 16, 45.

Kopal, Z. 1959, Close Binary Stars (New York: Wiley), Ch. III.

Kraft, R. P., and Luyten, W. J. 1965, Ap. J., 142, 1041.

Lamb, F. K., Pethick, C. J., and Pines, D. 1973, Ap. J., 184, 271.

Lampton, M., Margon, B., and Bowyer, S. 1976, Ap. J., 208, 177.

Li, F. K., and Clark, G. W. 1974, Ap. J. (Letters), 191, L27.

Long, K. S. 1975, thesis, California Institute of Technology.

Long, K. S., Agrawal, P. C., and Garmire, G. P. 1975, Ap. J. (Letters), 197, L57.

Maraschi, L., Treves, A., and van den Heuvel, E. P. J. 1977, Ap. J., 216, 819.

Margon, B., Bowyer, S., and Stone, R. P. S. 1973, Ap. J. (Letters), 185, L113.

Matteson, J. L., Mushotsky, R. F., Paciesas, W. S., and Laros, J. G. 1975, in Symposium on X-Ray Binaries, NASA SP-389, p. 407.

Meinunger, L. 1960, Mitteilunger über veränderliche Sterne (Sonneberg), No. 523.

Michalsky, J. J., Stokes, G. M., and Stokes, R. A. 1977, preprint.

Moore, W. E. 1975, thesis, California Institute of Technology.

Novikov, I. E., and Thorne, K. S. 1973, in Black Holes, Les Houches, 1973, ed. C. DeWitt and B. DeWitt (New York: Gordon and Breach).

Oda, M., Doi, K., Ogawara, Y., Takagishi, K., and Wada, M. 1976, Ap. Space Sci.,42, 223.

Oda, M., Gorenstein, P., Gursky, H., Kellogg, E., Schreier, E., Tananbaum, H., and Giacconi, R. 1971, Ap. J. (Letters), 166, L1.

Oda, M., Takagishi, K., Matsuoka, M., Miyamoto, S., and Ogawara, Y. 1974, Publ. Astron. Soc. Japan, 26, 303.

Oke, J. B. 1976, Ap. J., 209, 547.

Olson, E. C. 1977, Ap. J., 215, 166.

Parsignault, D. R., Grindlay, J. E., Schnopper, H., Schreier, E. J., and Gursky, H. 1975, in Symposium on X-Ray Binaries, NASA SP-389, p. 429.

Peimbert, M., Spinrad, H., Taylor, B. J., and Johnson, H. M. 1968, Ap. J. (Letters), 151, L93.

Piran, T. 1977, M.N.R.A.S., 180, 45.

Price, R. H., and Liang, E. P. T. 1975, preprint.

Priedhorsky, W. C. 1977, Ap. J. (Letters), 212, L117.

Rappaport, S., Bradt, H. V., and Mayer, W. 1971, Nature, 229, 40.

Rappaport, S., Zauman, W., Doxsey, R., and Mayer, W. 1971, Ap. J. (Letters), 169, L93.

Richardson, J. A., and Priedhorsky, W. C. 1977, in preparation.

Ritter, H. 1976, M.N.R.A.S., 175, 279.

Robinson, E. L. 1976, Ap. J., 203, 485.

Rothschild, R. E., Boldt, E. A., Holt, S. S., and Serlemitsos, P. J. 1974, Ap. J. (Letters), 189, L13.

Rothschild, R. E., Boldt, E. A., Holt, S. S., and Serlemitsos, P. J. 1977, Ap. J., 213, 818.

Ryter, C., Cesarsky, C. J. and Audouze, J. 1975, Ap. J., 198, 103.

Sandage, A. R. 1973, Ap. J., 183, 711.

Schreier, E., Gursky, H., Kellogg, E., Tananbaum, H., and Giacconi, R. 1971, Ap. J., 170, L21.

Schreier, E., Levinson, R., Gursky, H., Kellogg, E., Tananbaum, H., and Giacconi, R. 1972, Ap. J. (Letters), 172, L79.

Seward, F. D., Burginyon, G. H., Grader, R. J., Hill, R. W., and Palmieri, T. M. 1972, Ap. J., 178, 131.

Shapiro, S. L., Lightman, A. P., and Eardley, D. M. 1976, Ap. J., 204, 187.

Shrewsberry, D., Budney, T., Riley, D., and Schuler, B. 1973, AAIA 3rd Sounding Rocket Technology Conference, AAIA No. 73-288.

Shulman, S., Friedman, H., Fritz, G., Henry, R. C., and Yentis, D. J. 1975, Ap. J. (Letters), 199, L101.

Stevens, J. C. 1973, thesis, California Institute of Technology.

Stevens, J. C., Garmire, G. P., and Riegler, G. R. 1972, Ap. J. (Letters), 175, L73.

Stockman, H. S. 1977, private communication.

Stockman, H. S., Schmidt, G. D., Angel, J. R. P., Liebert, J., Tapia, S., and Beaver, E. A. 1977, preprint.

Sutherland, P. G., Weisskopf, M. C., and Kahn, S. M. 1977, preprint.

Swank, J., Lampton, M., Boldt, E., Holt, S., and Serlemitsos, P. 1977, Ap. J. (Letters), 216, L71.

Szkody, P., and Brownlee, D. E. 1977, Ap. J. (Letters), 212, L113.

Tapia, S. 1976, IAU Circ., No. 2987.

Tapia, S. 1977, Ap. J. (Letters), 212, L125.

Terrell, N. J. 1972, Ap. J. (Letters), 174, L35.

Thorne, K. S., and Price, R. H. 1975, Ap. J. (Letters), 195, L101.

Warner, B. 1974, M.N.R.A.S., 168, 235.

Warner, B. 1976, in Structure and Evolution of Close Binary Systems, IAU Symposium No. 73, P. Eggleton et al., eds., p. 85.

Weisskopf, M. C., Kahn, S. M., and Sutherland, P. G. 1975, Ap. J. (Letters), 199, L147.

Wu, C., van Duinen, R. J., and Hammerschlag-Hensberge, G. 1975, in Symposium on X-Ray Binaries, NASA SP-389, p. 529.

APPENDIX A

EXPERIMENT DESCRIPTION

I. INTRODUCTION

Some of the data which are the subject of this dissertation were obtained from a sounding rocket payload consisting of mechanically collimated large area proportional counter X-ray detectors. The low energy detector (LED) was sensitive to X-rays in the range 0.2 to 3.5 keV, while the medium energy detector (MED) was sensitive from 1.0 to 24 keV. Both detectors were prototypical of their namesakes on the HEAO-A2 satellite experiment. The payload was modified from a previous configuration in order to convert the LED to thin window operation (requiring active gas regulation) and to reduce the payload mass. The payload was originally built by the Goddard Space Flight Center X-ray group and flown five times (NASA sounding rockets 13.007-13.010 and 26.037) previous to the 1976 May 11, 11:00 UT launch of Nike-Aerobee 26.038 described herein.

The payload was launched by a solid fuel Nike (booster)-liquid fuel Aerobee 200 (sustainer) combination to a peak altitude of 175 km. Proportional counter data were obtained for 198 seconds above 130 km. Below 130 km atmospheric absorption to the zenith is greater than 5% at both 0.25 and 1.0 keV. All data used were obtained at altitudes greater than 130 km. Booster separation occurred at booster burnout, approximately one-half mile above the launch site at a velocity of one thousand miles per hour, three seconds after launch. The rest of the rocket, including

the spent sustainer motor and tanks, parachute section, attitude control system (ACS), experiment, and telemetry section (TM) remained intact after sustainer burnout through the observation until atmospheric reentry. The experiment, TM, and ACS were parachuted to the ground within fifteen minutes after launch, and recovered intact the next morning.

The flow of information from cosmic X-rays incident above the atmosphere to coded data on magnetic tape at the ground station was as follows:

1) Mechanical collimators limited the response of the detector package to a 3° x 3° (FWHM) triangular field of view which was pointed by motion of the entire payload.

2) An X-ray which successfully passed the collimator had an (energy-dependent) probability of transmission through a thin plastic detector window and photoelectric absorption in the counter gas. The cloud of electrons produced by the X-ray drifted towards a high voltage wire anode and underwent avalanche multiplication in the electric field near the anode.

3) The charge pulse on the proportional counter anode was counted and pulse height analyzed. Scalar and pulse height information was coded in a PCM digital format and transmitted to the ground station at a rate of 100 kilobits/second.

The sub-systems which conprised the experiment will be described in detail below.

II. POINTING, ASPECT, AND COLLIMATION

Experiment pointing was determined by the attitude of the entire rocket assembly. Attitude was controlled by a STRAP-IV attitude control system (Shrewsberry et al. 1973), which was the responsibility of Mr. Tom Collinson, NASA Sounding Rocket Division, Code 745.1. Briefly, the orientation of a three-axis gyro system was updated after sustainer burnout by star tracker observations of two bright stars (for this flight, α Lyr and γ Cyg). The rocket was torqued by cold-gas jets for slewing motions and for station-keeping on a target. It is possible, with a 3σ degree of confidence, to point within 0.5° in each axis of an invisible (to the star-tracker) X-ray target, after the update star observations.

Post-flight determination of experiment aspect was made from star field photographs. A Nikon-F 35-mm camera with motor drive was mounted on the body of each detector. As the drift during each pointed observation was expected to be small, only a limited number of photographs were required to check the direction of each target. Because camera-firing noise had appeared in the detector data in previous experiments, only three aspect exposures were taken, one during the exposure on Cyg X-2, and two during the exposure on Cyg X-1.

Star positions on the film were measured in a coordinate system based on the sprocket holes. In order to determine the direction of the detector response in that coordinate system, collimator calibrations had been made with respect to a machined flat on the surface of each collimator. Upon integration of the experiment and ACS star tracker at

White Sands, the front surface of the star tracker, perpendicular to the star tracker response, was shimmed to the mean direction of the two collimator flats by means of spirit level measurements accurate to 2'. A theodolite sighting was made of a distant landmark, then the theodolite was flipped 180° to sight on a flat mirror placed on the front surface of the star tracker. The payload was moved so that the beam from the theodolite reflected upon itself, with an estimated error from mirror non-flatness and the theodolite flip of 1-2'. With the experiment aligned so that the star tracker axis pointed towards the landmark, calibration photographs were taken with both aspect cameras.

Star positions were measured directly from the negatives by means of a microscope and an X-Y table which moved the negatives through the microscope field of view, to form a primitive but effective measuring microscope. Positions were reduced to a coordinate system originating on the star-tracker axis. The direction in right ascension and declination of the origin was determined by the method of Brisken (1973): the direction of the origin was calculated for each pair of stars measured, and the final star tracker direction and error were estimated from the mean and standard deviation of the direction determined from each pair of stars. The star-tracker direction for each exposure is thus known to an accuracy of 4' (1σ error). Since the full width at half maximum of the collimator response is 3°, aspect induced errors in effective detector area are thus less than 2.5% of the peak effective area.

Collimation of the proportional counter response was achieved by passive mechanical "egg-crate" collimators. Though the idea of

construction of an "egg-crate" collimator by intermeshing slats is not new, slats made by a photo-etching process allowed construction of an "egg-crate" collimator with a narrower field of view than previously possible. Figure 1 shows a section of the collimator.

Slat collimators were chosen over an etched grid design (Stevens 1973) for the following reasons: (1) A slat collimator has the mechanical strength to support the window on its back side. Etched grid collimators require auxiliary slat collimators for window support. (2) The minimum absorption length presented to rejected X-rays in an etched grid design is the grid thickness d, while for a slat collimator the minimum path is $d/2\theta$, where d is the slat thickness and θ is the full width at half maximum of the collimator response (see Figure 1). It is thus possible, for a given collimator material, to build a slat collimator useful for higher energy, more penetrating X-rays, than a grid collimator. (3) Manufacture of the slats was estimated to cost about one-half as much as the required number of grids.

Since it would be difficult to work with slat material thinner than 0.010", it was necessary for the collimator to be deep in order to have satisfactory transmission. For a given slat thickness d and FWHM response θ, in the small angle approximation $\tan \theta = \theta$,

$$s = \theta L,$$

while maximum transmission

$$T_{max} = \left(\frac{s}{s+d}\right)^2$$

Figure 1

Section of a slat collimator, perspective view (not to scale). The dimensions L, d, and s set the scale and field of view of the collimator. The window side of the collimator is to the top. Note that the slats which support the window on their unnotched edge are raised 0.010" above the cross slats. The dashed track is the path of minimum absorption length for rejected X-rays. The notched corners at the bottom hold the collimator in its housing.

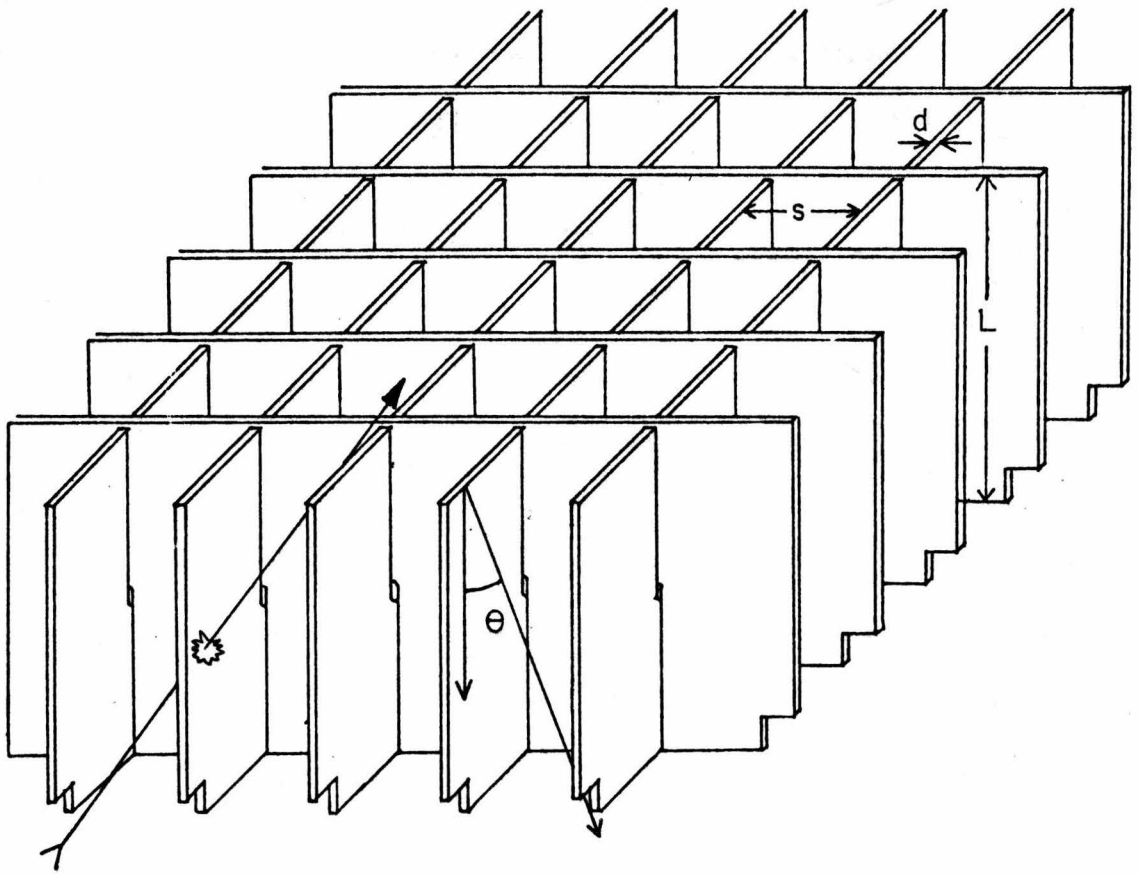

Figure 1

where L is the collimator depth and s is the slat separation. Thus

$$T_{max} = \left(\frac{1}{1 + d/\theta L} \right)^2$$

for d = 0.010", θ = 3°, and $T_{max} > 0.9$, we require L > 3.5". It was decided to build the collimators to a depth of 3", which was the maximum that would fit within the payload skin. It should be noted that the maximum transmission calculated is reduced by any irregularity in the slats that increases the effective value of d.

Slots of length L/2 must be cut into the slats of an egg-crate collimator so that the pieces will fit together. A limit to the depth of a slat collimator is thus set by machine shop practice. Slots of width 0.014" can be cut by a slotting saw to depth no greater than 0.5" before flexure by the narrow saw becomes a problem. It was decided to construct the slats by a photo-etching technique. The slats were made by United Western Enterprises Photo Fab Division at a total cost of $3000 for two 17 x 49 cm collimators. Assembly of the slat collimators was complicated by the flexibility of the long slat teeth. It was necessary to epoxy the collimator pieces together for rigidity. Special teflon jigs were constructed to hold the slat teeth in position as the collimator was assembled. Each slat tooth had to be individually pulled into position in the jig during assembly. Each slot was painted with epoxy, then wiped so that epoxy remained only in the slits, before it was placed in position. A slow-setting epoxy was required, as a collimator panel consisting of 58 short slats crossed with 39 long slats had to be assembled at one sitting. The epoxy chosen was 10 parts by

weight Epocast 212 mixed with 1 part by weight Furane 927 hardener, which set in 24 hours at 60° C. Each panel of 17 x 24 cm required more than eight hours work by three people for assembly.

Even with the assembly jigs, a large number of teeth ended up out of position or bent, reducing the collimator transmission. Another problem, potentially more serious, was the poor bonding of the slow setting epoxy used, especially with the beryllium-copper slats used for the MED collimator. Much better results could be obtained with the Resiweld 7004 A and B epoxy used for typical laboratory work, but the Resiweld had a pot life of only a few hours, and set too quickly for the collimator assembly. Collimator teeth tended to break loose from their epoxied positions. It was necessary to repeatedly clean the collimators of loose epoxy chips that had flaked away. Although the loose teeth and epoxy chips seemed threatening, no window damage was encountered during vibration testing or flight.

Collimator response was calibrated by measuring light transmission with the setup shown in Figure 2. A parallel beam of light produced by a 20" telescope was incident on the collimator. An eight-inch telescope behind the collimator was masked to accept light only from the collimator section under test. The transmitted beam was focused to a point, which was isolated by an aperture and measured by a photomultiplier. Light which reflected from the collimator slats was focused away from the aperture.

Each collimator was measured in four sections. Scans of transmission vs. angle (see Figure 3) were made by turning the collimator on a

Figure 2

Collimator calibration setup. Light from the laser is focused by the large (20") telescope into a parallel beam. The beam is masked so that only the light passing through the collimator is focused by the smaller (8") telescope and detected by the photomultiplier. Collimator response as a function of angle is scanned by turning the rotating table.

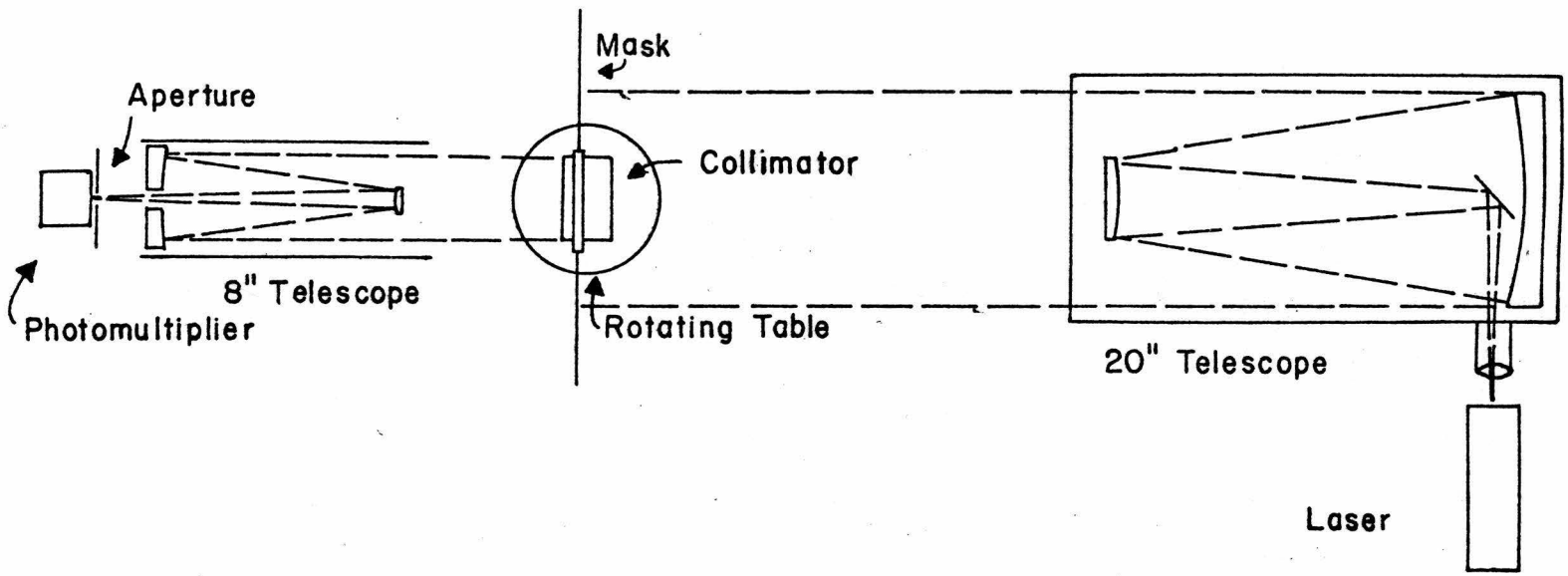
Mask
Aperture
Collimator
8" Telescope
Photomultiplier
Rotating Table
20" Telescope
Laser

Figure 2

Figure 3

Transmission versus angle $\Delta\theta$ for a typical collimator panel. The direction of maximum response defines $\Delta\theta = 0$. The line is the best fit to the linear region of the response function.

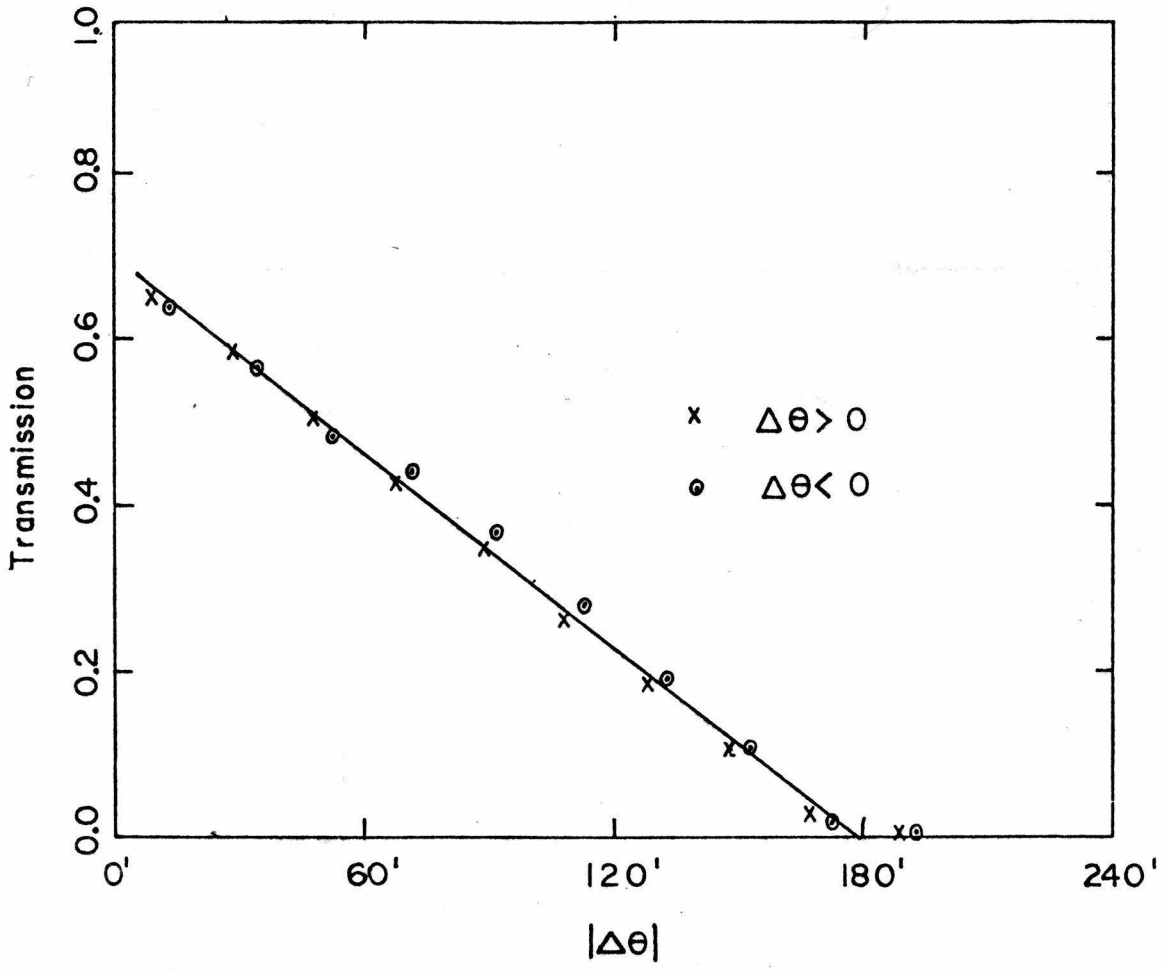

Figure 3

rotating table. As expected, a triangular response of 3° FWHM was obtained. Rounding at the top of the response is due to misalignment of collimator slats.

Calibration of the direction of peak transmission was done by placing a mirror on the machined flats at the front of the collimator. The test beam was reflected by the mirror back towards its source. The collimator was rotated a measured amount so that the beam reflected exactly on itself. The amount of rotation required was the difference between the direction of the machined flat and the peak response.

Peak collimator transmission was measured by maximizing collimator throughput, then removing the collimator from the beam. Average peak transmission for the eight collimator sections measured was 0.68. Tests of X-ray transmission of selected sections confirmed this result. The peak transmission was substantially lower than the theoretical maximum transmission of 0.88. The deficiency of transmission is ascribed to misaligned collimator teeth and excess epoxy on the sides of the tubes.

The effective detector areas below were determined from collimator calibrations and aspect data for the two source exposures. ACS data indicated that there was no drift during each pointing. This was confirmed by the identical directions of the two aspect frames taken during the Cyg X-1 exposure.

Effective area, Cyg X-2 exposure:

LED: 387 ± 16 cm^2

MED: 376 ± 25 cm^2.

Effective area, Cyg X-1 exposure:

LED: 429 ± 14 cm^2

MED: 500 ± 20 cm^2.

III. PROPORTIONAL COUNTER: GAS CONTROL SYSTEM AND WINDOWS

The two proportional counter detectors, although very similar internally, showed different energy responses because of different configurations of counting gas and window material. Figure 4 shows the LED in cross-section.

Since a proportional counter detects every photon absorbed in the counting gas, the counter efficiency

$$\varepsilon(E) = (T_{window}(E))\ (1-T_{gas}(E)),$$

where T_{window}, T_{gas} are the energy dependent X-ray transmission of the window and gas layer. The transmission T of a layer of material $T = e^{\sigma n \ell}$, where σ is the cross-section per atom to absorption, n is the density of the material in atoms per unit volume, and ℓ is the thickness of the material presented to the X-rays. Detector response is thus predicated upon the choice of window and gas thickness and material. The LED used propane counting gas at a pressure of 20 cm Hg, while the HED used P-10 counting gas (90% argon and 10% methane) at 83.6 cm Hg. The choice of the window material for each detector was a compromise between window strength and X-ray transmission. Each window was required to support the counting gas pressure across a square 0.42 cm on a side,

Figure 4

Cross-section of the low energy detector (LED). The collimator limits the detector field of view to 3° FWHM. The bottom and side anode cells form a guard layer in anticoincidence with the active layers. The polypropylene detector window is epoxied onto the Z-frame with its carbonized layer facing into the counter, in order to form a ground plane for the first anode layer.

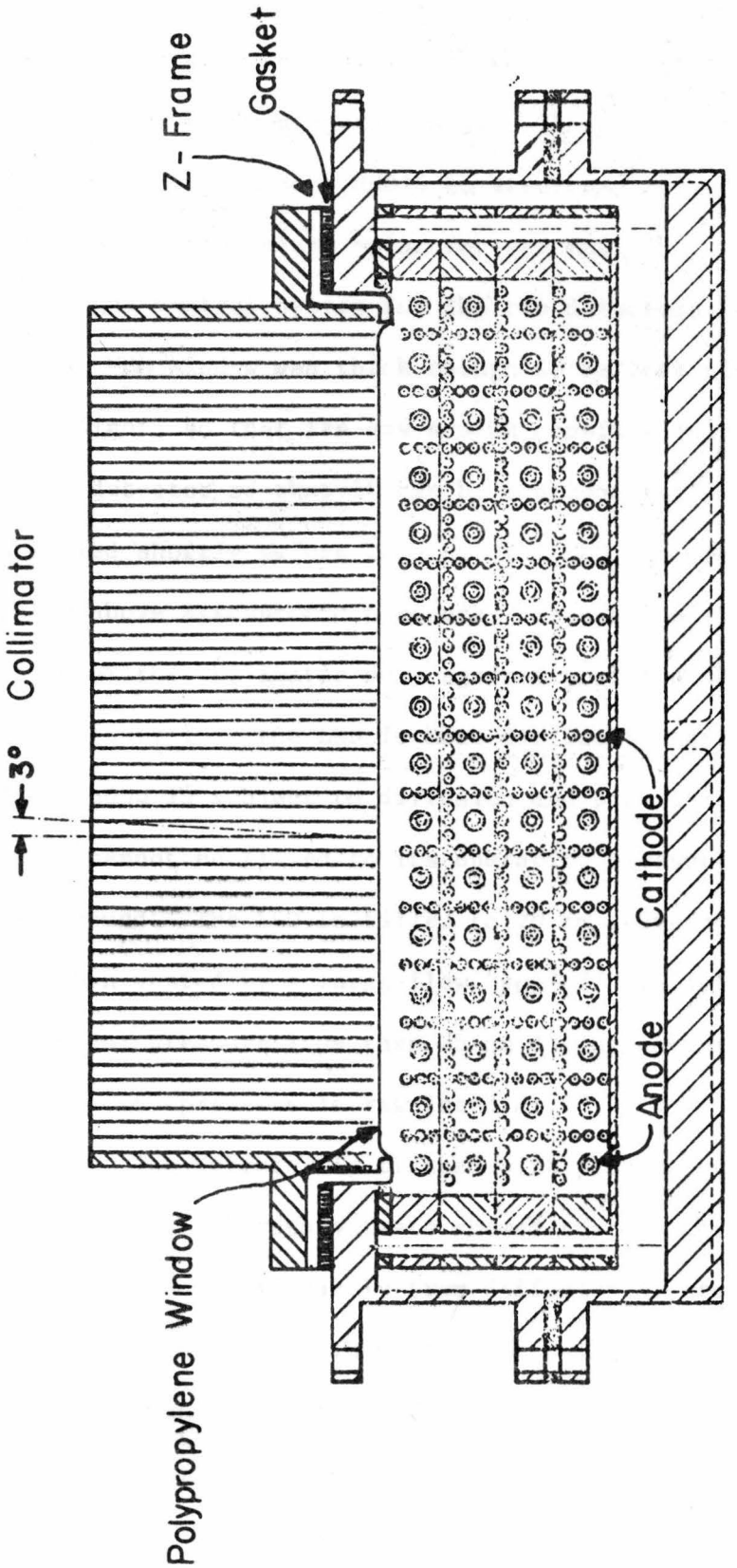

Low Energy Detector (LED)

Figure 4

the collimator grid spacing, while showing an acceptable X-ray transmission in the desired energy range. These considerations led to the choice of carbon-coated 0.00015 cm stretched polypropylene for the LED and 0.00062 cm aluminized Mylar for the MED.

The gas control system for the two detectors is shown in Figure 5. The Mylar MED window was thick enough to be leak tight for the duration of the flight, so that its gas system consists only of two valves to open the detector so that it can be continuously purged in the tower, then sealed shortly before launch. The MED was pressurized to 83.6 cm, slightly above atmospheric pressure, because the window is supported by the back of the collimator only against positive detector pressure.

Gas control of the LED is more difficult because the thin polypropylene window is subject to diffusion and pinhole leaks, and because the detector cannot be filled to its operating pressure of 20 cm absolute on the ground. The LED is filled to 20 cm above ambient in the tower, and is then vented by a large-flow "pop-off" relief valve to maintain a differential pressure less than 25 cm during ascent. During the experiment, detector pressure is regulated at 20.0 cm by a Hoke mechanical regulator. The detector is flushed with propane until two minutes before launch. Laboratory tests showed that detector performance did not deteriorate significantly from diffusion of atmospheric water vapor and oxygen through the thin window for several minutes after purging stopped. It was thus decided not to flush the detector in flight, as had been done with previous Caltech proportional counter payloads (Stevens 1973, Moore 1975, Long 1975). The low vapor pressure of propane

Figure 5

Schematic diagram of the gas control system for the LED and MED.

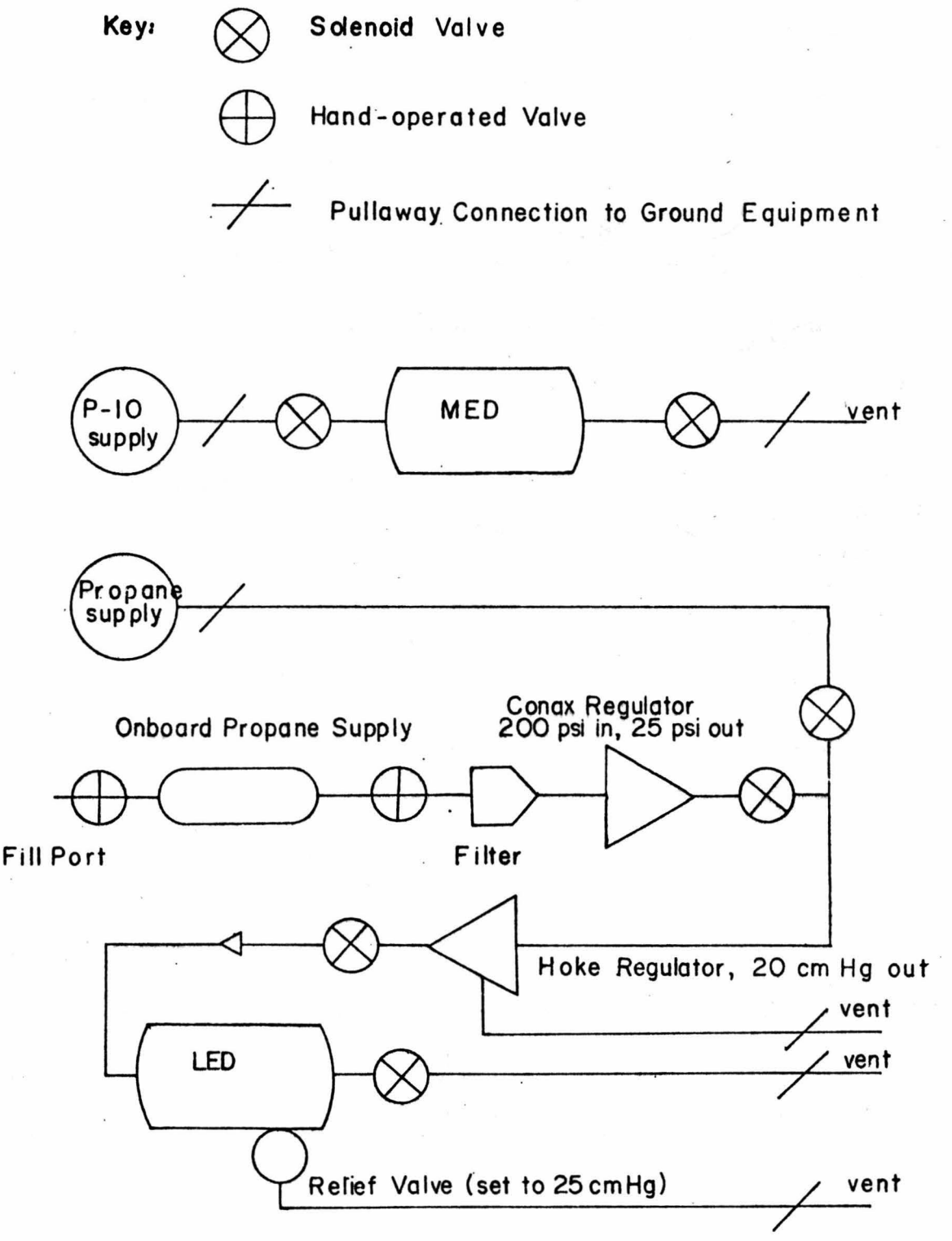
Key:
Solenoid Valve
Hand-operated Valve
Pullaway Connection to Ground Equipment
P-10 supply
MED
vent
Propane supply
Onboard Propane Supply
Conax Regulator
200 psi in, 25 psi out
Fill Port
Filter
Hoke Regulator, 20 cm Hg out
vent
LED
vent
Relief Valve (set to 25 cmHg)
vent

Figure 5

allows its storage in liquid form. A small onboard tank carried 250 g of propane for pressure regulation and refilling the detector during reentry.

"Z-frames" were constructed to allow window replacement from the front of the detector simply by removing the collimator. In previous flights in a sealed configuration, when no window changes were anticipated, the windows were mounted internally. Window replacement required removal of the detector from the payload and almost complete detector disassembly. Since we planned to install flight windows for both detectors at the launch site just days before the launch, window frames that could be mounted to the front of the detector were desired (seen in cross-section in Figure 4). Previous detectors in Caltech payloads had been designed so that windows could be mounted on flat aluminum frames, but the constraint that the new frames fit between the existing collimator and the detector body required a three-dimensional frame with a vaguely Z-shaped edge cross-section. It was decided that the most economical method of manufacture was to press the frames from flat aluminum stock. This task was contracted to the California Hydroforming Company, El Monte. The cost for the frames was $158 each for an order of 12 (one of which was actually used in flight), plus the machine shop charges for trim and hole pattern at Caltech. A considerable saving was had over similar Z-frames for the HEAO-A2 LEDs, each of which was machined out of a single piece of aluminum at a cost of about a thousand dollars.

Mylar aluminized on one side, of thickness 0.00062 cm, is commercially available and needed only to be bonded to the Z-frames. Both Mylar and polypropylene windows were epoxied to the frames with an epoxy consisting of Shell Epon resin 828 and curing agent V-40. The Mylar was mounted on the frame so that the aluminized side faced the detector. It was necessary to paint the edge of the window in places with Aquadag graphite suspension to ensure electrical contact between the aluminum layer and the Z-frame. The aluminized layer thus formed the ground plane for the top layer of detector anodes.

Polypropylene windows were stretched from commercially available 0.0025 cm sheet. The window side facing the detector was carbon coated to form a ground plane. Stretching and coating techniques have been discussed by Stevens (1973), Moore (1975), and Long (1975).

Window transmission was calibrated by measuring the transmission of Po-210 alpha-particle fluoresced K X-rays of boron (185 eV), carbon (282 eV), oxygen (523 eV), fluorine (677 eV), and magnesium (1260 eV) for the polypropylene window. K lines of carbon, magnesium, aluminum (1496 eV), and silicon (1753 eV) were used to calibrate the Mylar windows. Transmission was measured over a series of long strips covering the entire window. The Mylar transmission data were well fit by a uniform Mylar thickness of 868 $\mu g/cm^2$. Polypropylene windows used in previous Caltech sounding rocket experiments did not show the transmission expected from a layer of uniform thickness, and were fit by a "two-thickness" model (Stevens 1973, Moore 1975, Long 1975). Considerable progress in the art

of window stretching, motivated particularly by the production of windows for the HEAO A-2 experiment, has occurred since that time. Since no changes in window stretching technique had occurred, it appears that the improvement of window quality is the result of practice in the production process. Transmission of the polypropylene LED window was fit quite well by a uniform thickness model (Figure 6), except for a slight deviation at the oxygen line, which was shown to be the result of contamination of that line in the test source by carbon X-rays (Tuohy, private communication). Figure 7 shows the net quantum efficiency of the two detectors, including window transmission and counter gas absorption.

The interaction of X-rays with the counter gas, and subsequent charge amplification to produce a charge pulse on the anode, has been reviewed by Giacconi et al. (1968).

IV. PROPORTIONAL COUNTER: PULSE AMPLIFICATION AND PROCESSING

The event processing subsequent to the deposition of charge on an anode wire in this experiment has been described in detail by Birsa, Glasser, and Ziegler (1972). Only a brief summary of that process will be presented here.

The detectors are wired so as to divide the counting gas into cells of 1.27 cm square cross-section which run the length (50 cm) of the counter (see Figure 4). Each cell is formed by a central anode wire and ground plane wires. The LED consists of three layers and a fourth guard layer on the bottom and sides, while the MED has four active

Figure 6

X-ray transmission of carbon-coated polypropylene window used in flight as a function of X-ray energy. The curve shows the expected transmission for a pure polypropylene window of surface density 132.7 $\mu g\ cm^{-2}$. The statistical errors in the measured points are smaller than the plotted symbols.

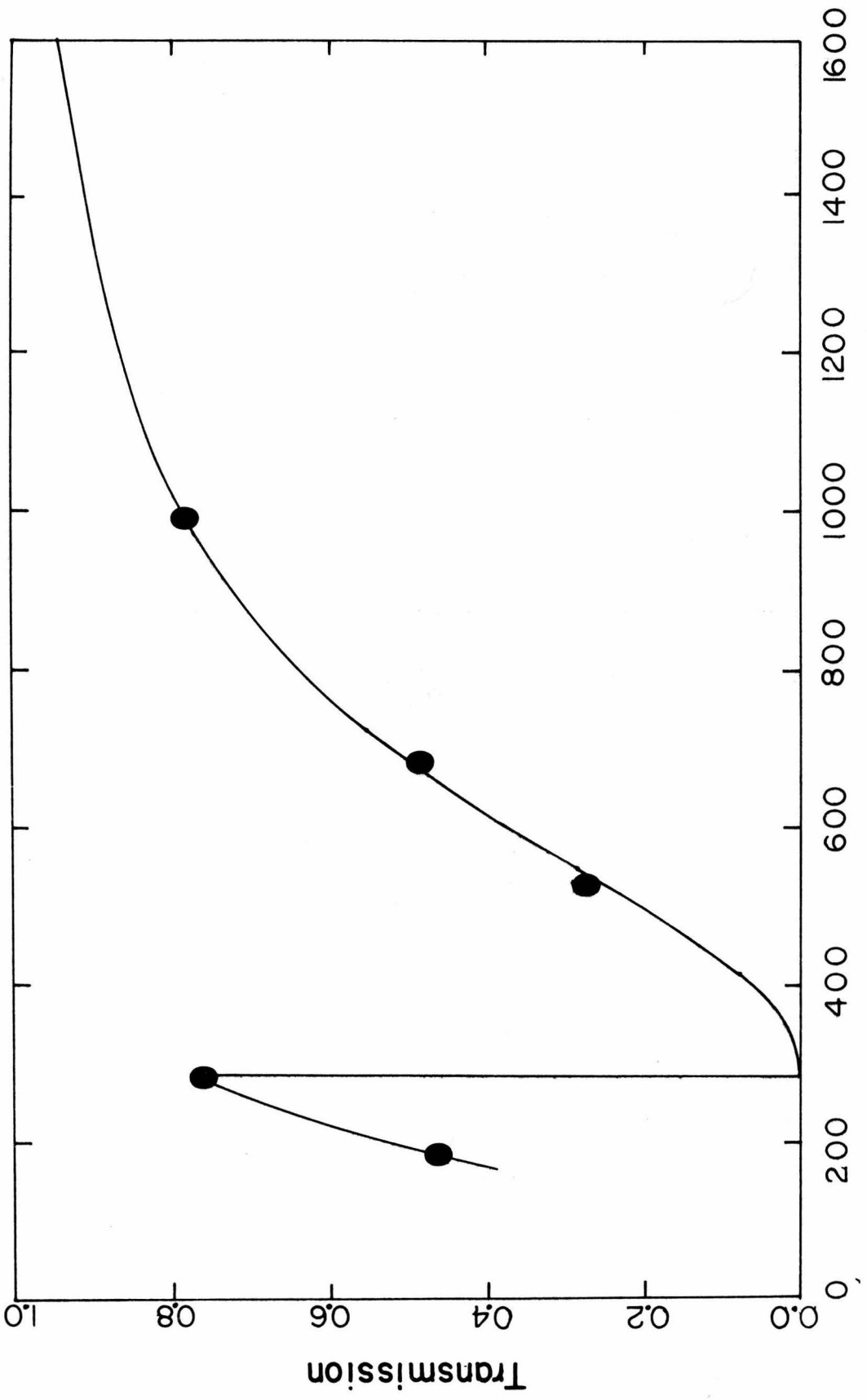
Transmission
0.0
0.2
0.4
0.6
0.8
1.0
0
200
400
600
800
1000
1200
1400
1600
Energy (eV)

Figure 6

Figure 7

Net efficiency of the LED and MED as a function of energy.

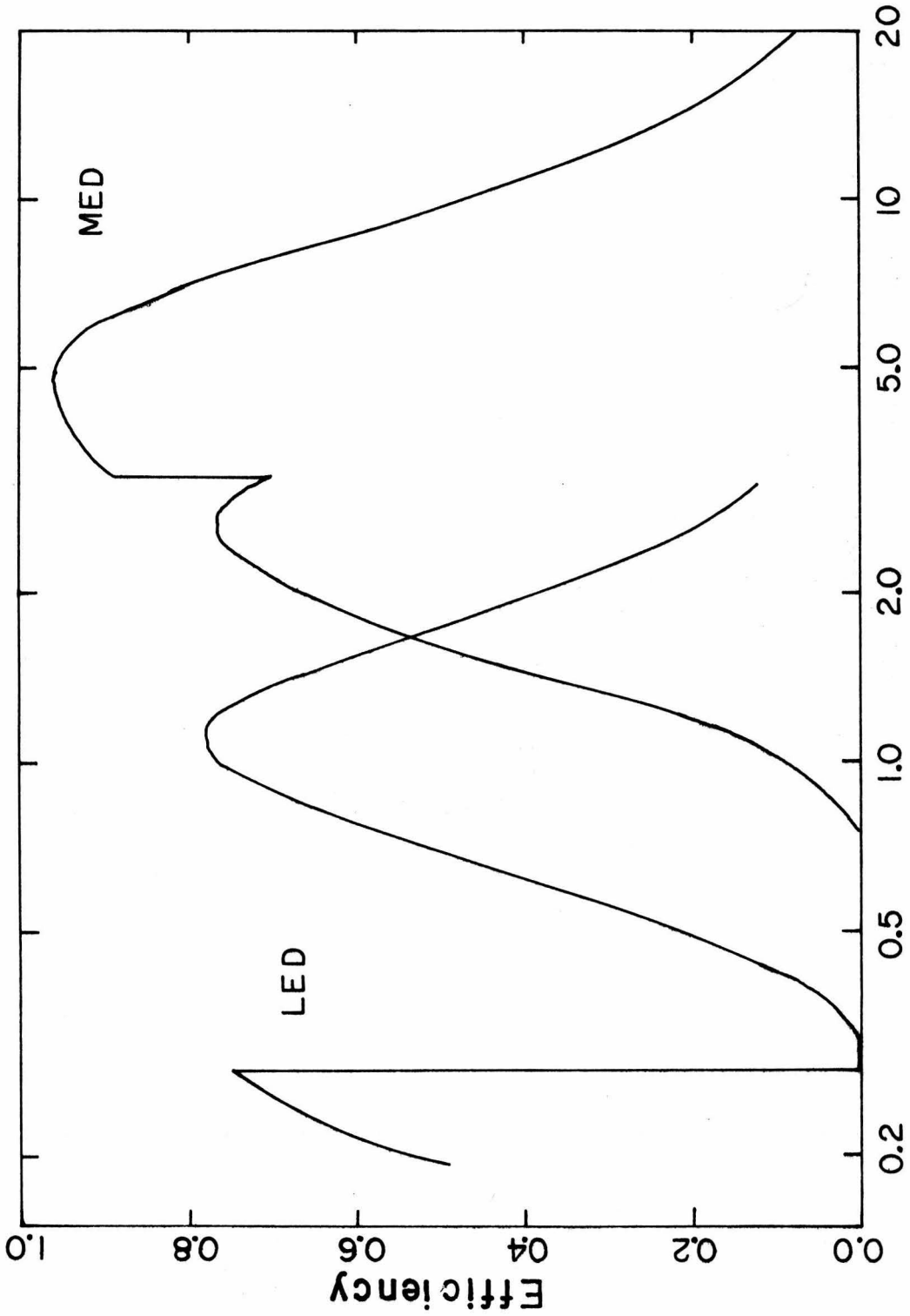
MED
LED
Efficiency
0.0
0.2
0.4
0.6
0.8
1.0
0.2
0.5
1.0
2.0
5.0
10
20
Energy (keV)

Figure 7

layers and a guard layer. Events occurring in an active layer are rejected if there is a coincident event in the guard layer or in another active layer of the detector. This is to reject charged particles, which leave a long ionization path traversing several cells. The "marked bit" discrimination of previous flights of this payload, which identified events coincident in horizontally adjacent anode cells, was disabled for this flight. It had been shown previously to make no significant improvement in the detector background (Rothschild, private communication). For an event to be accepted as a valid X-ray event, it must pass low and high level discriminator thresholds.

The rocket PCM-FM transmitter is continuously modulated with a repeated format consisting of 64 frames of 16-bit words. The bit rate is 100 kHz. The first valid X-ray event occurring during a word is pulse hieght analyzed into one of 128 energy channels. Telemetered information about that X-ray event consists of 7 bits of pulse height information and 3 bits of layer and detector information. Subsequent X-ray events are scaled only, 5 bits of scaler information being also transmitted every word.

The scaler data provided very high time resolution information about a source. Dead time for each event was less than 10 μsec, so that data loss for Cyg X-1 and Cyg X-2 was typically less than 1%. Scaler data were transmitted for each 160 μsec bin. Pulse height analyzed (PHA) data could be transmitted for only one event every 160 μsec, and also had a fixed duty cycle only about 90% of that of the scaler. The scaler summed events from all the layers of both

detectors, so that even the energy information in an event from the different energy responses of the two detectors was lost. Counts from the diffuse X-ray background in the lowest energy channels of the LED could be easily excluded from the PHA data after the flight, on the basis of the energy information. That flux produced a substantial background (about 200 cts sec^{-1}) in the scaler data.

Since no explicit temporal structure faster than the shot noise variation was detected, the limitations of the scaler data were not serious. PHA data were used for all analyses except for the search for millisecond bursts and the fast autocorrelations. Dead time corrections for the PHA data, calculated for each data set from the ratio of the scaler to PHA counts, were of order 20-25%.

V. IN-FLIGHT EXPERIMENT CALIBRATION

Verification of instrument performance was obtained by radioactive X-ray sources, mounted in the experiment doors, which were observed during ascent and reentry. These data serve to demonstrate the response of the proportional counters to monoenergetic X-rays.

Figure 8 shows pulse height analysis data for 15 second integrations of calibration data from each detector. Both show peaks which are satisfactorally fit by a gaussian energy response to mono-energetic X-rays. Pre-flight calibration had confirmed that the channel number of the peak was indeed proportional to X-ray energy E, and that resolution broadening was proportional to $E^{0.5}$, as expected for proportional counters.

Figure 8

a) Pulse height data from a 15 second integration of LED calibration source. The calibration line was the 1.50 keV $K_{\alpha\beta}$ line of aluminum, produced by fluorescence in Al foil by Po-210 α-particles. The observed line is fit by a gaussian with full width at half maximum of 32.7%.

b) Similar pulse height calibration data for the MED. The calibration sources were an Al $K_{\alpha\beta}$ source, as in the LED, and a radioactive Fe-55 source that produced the 5.98 keV $K_{\alpha\beta}$ line of manganese. Both peaks are fit by gaussians.

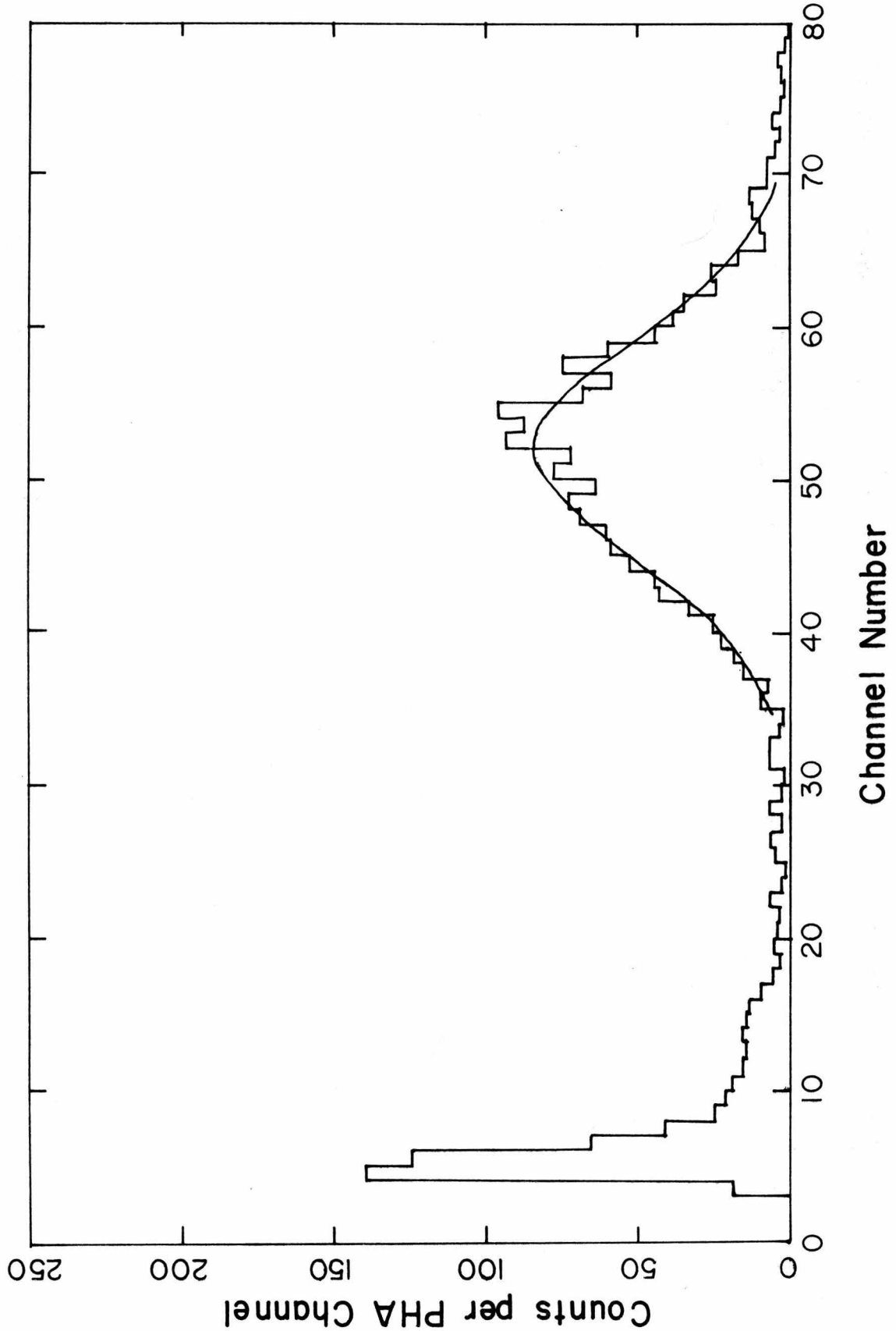
Counts per PHA Channel
0
50
100
150
200
250
0
10
20
30
40
50
60
70
80
Channel Number

Figure 8a

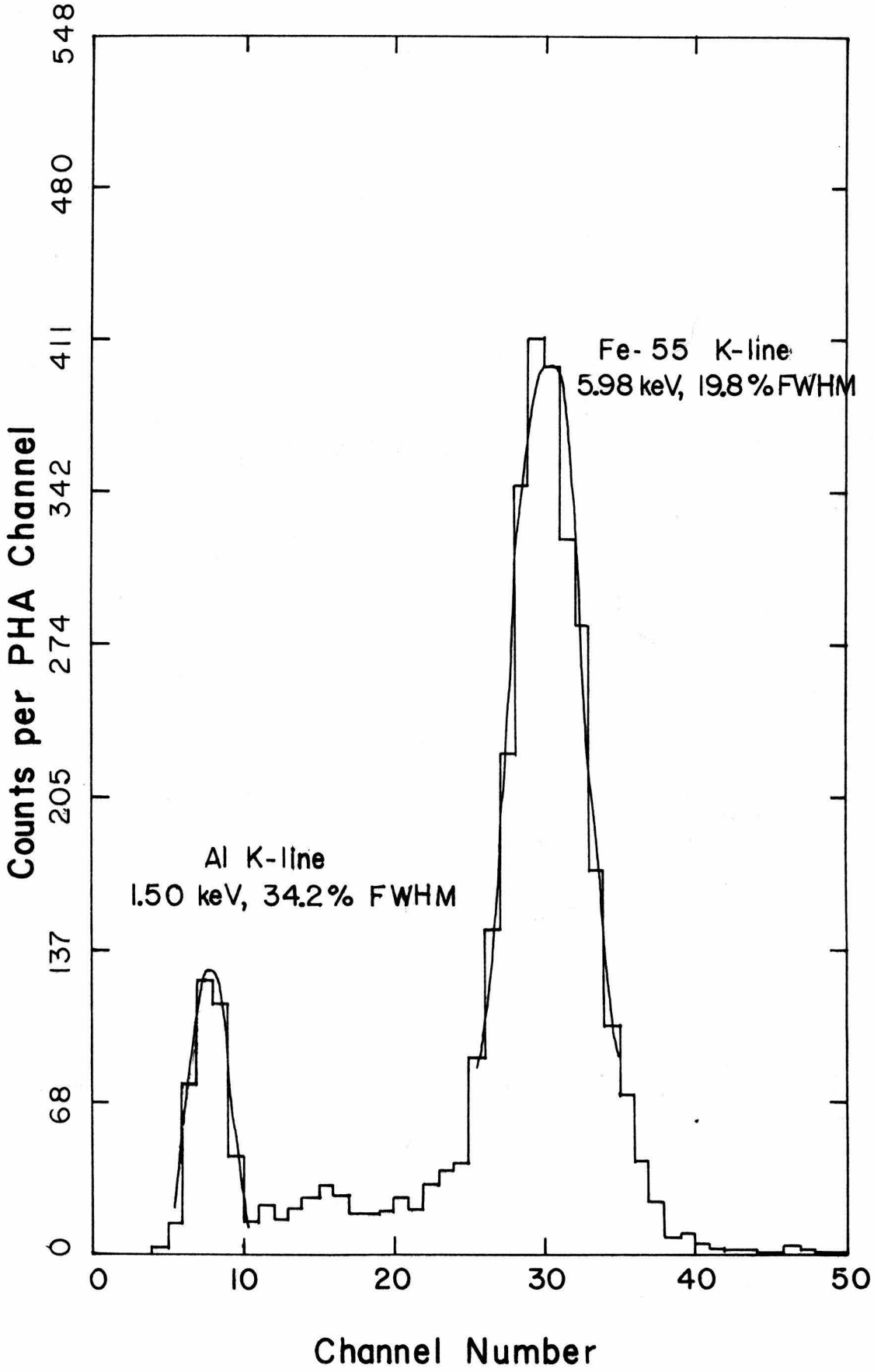
Counts per PHA Channel
0
68
137
205
274
342
411
480
548
Fe-55 K-line
5.98 keV, 19.8% FWHM
Al K-line
1.50 keV, 34.2% FWHM
0
10
20
30
40
50
Channel Number

Figure 8b

Two major irregularities were evident in the calibration and experimental data:

1) The counting rate in layer 2 of the MED shows repeated sharp drops and slow recovery (time of whole event about 1 second), which appears identical to the detector behavior seen when high voltage breakdown was experienced in laboratory tests. The change in counting rate indicates the loss of gain and slow recovery resultant from the decrease in anode voltage caused by breakdown somewhere in the high voltage network. This behavior commenced approximately 282 seconds after launch. All data after that time were rejected from further analysis. Data taken before the commencement of breakdown are believed to be clean because (a) the search for millisecond bursts turned up many 1-millisecond bins with anomalously large numbers of counts after T+282 seconds, but none before that time, and (b) dips in the layer 2 counting rate show up clearly as bursts in the anti-coincidence rate, none of which are seen before T+282 seconds.

2) The gain of the LED increased by more than 50% between the ascent and descent calibrations. LED pressure transducer data show that the detector pressure was rapidly decreasing through the ascent calibrations and settled shortly after the end of those calibrations. This pressure anomaly may have been the result of a possible constriction in the flexible tubing connecting the LED and its pressure regulator, which could slow the backbleeding of the detector down to the set pressure. Since, in the operating region, detector gain goes as approximately the inverse seventh power of the pressure, the LED pressure

readings, accurate to ± 0.5 cm Hg, are not accurate enough to calibrate the detector gain. However, a limit can be set on the rate of change of the gain during the time span of the source observations and final calibration of $d(\ln G)/dt \leq 0.0008/\text{sec}$. The counting rate of the low energy diffuse background is a steep function of energy, so that the counting rate in certain channels of the LED is a function of gain. A change in the gain of $d(\ln G)/dt = -0.0011 \pm 0.0002\ \text{sec}^{-1}$ could be deduced from the change in the counting rate in LED layer 1, channels 6-10. The gain during source observations from T+161 sec to the first reentry calibration at T+346 sec is thus known to about ± 10%. Fast changes in the counting rate in broad energy bins, which are the subject of temporal studies, were thus little affected by the gain shift. Spectral fitting of the LED data was more difficult, as changes in gain of a few percent resulted in shifts of best-fit spectral parameters by amounts substantially greater than counting statistic errors. Lower energy detector spectra were thus used only in conjunction with MED data. In the spectral reduction, the power law index and normalization determined by the MED were held fixed, and the low-energy absorption and gain were treated as free parameters.

APPENDIX B

THE CORRELATION PROGRAM SUPERCOR

I. INTRODUCTION

Additional observations of Cyg X-1 would be valuable in refining the results of Chapter 1 of this thesis. In particular, cross-correlations of the energy-resolved X-ray flux may confirm the time lag suggested by data from the sounding rockets 13.010, 26.037, and 26.038. Further data will also refine values for the auto-correlation and time-skewness functions to yield more information about shot shapes and time-symmetry. Since the GSFC-Caltech-Berkeley-JPL HEAO-A2 experiment promises to deliver such data, this appendix was written to document the correlation program used to analyze the rocket data. It is hoped to thus facilitate analysis of the satellite data.

SUPERCOR (a listing of the program is included as Exhibit 1) is a program to calculate auto-correlations, cross-correlations, and time-skewness functions (jointly referred to below as "correlation functions") of real and simulated data. In addition, parameters λ, τ, h and f (see below) for a model of exponential shot pulses can be determined from a data set. Correlation functions of a series of data sets can be calculated and averaged to determine a mean correlation function. The program is written in FORTRAN for the Caltech IBM 370 computer.

II. CORRELATION FUNCTIONS

Several different correlation functions have been useful in the data analysis reported in Chapter 1. Sutherland, Weisskopf, and Kahn (1977)(henceforth SWK) define the "partially unbiased autocorrelation function:

$$\tilde{\rho}_u = \frac{\tilde{R}_u}{\tilde{R}_u}, \tag{1}$$

$$\tilde{R}_u = \frac{1}{N} \sum_{i=1+u}^{N} (s_i - \bar{s})(s_{i-u} - \bar{s}) + \frac{(N-u)}{N^2(N-1)} \sum_{i=1}^{N} (s_i - \bar{s})^2.$$

For a shot model assuming exponential pulses of the form $I(t) = he^{-t/\tau_o}$ $(t > 0)$, the shot decay time τ can be calculated by fitting the calculated autocorrelation points ρ_u to equation (2) of Chapter 1. The data sets used in the analysis of the rocket observations were long enough, $N = 205$, that the second correction term on the right hand side of (1) was small. For that reason, a simpler formula was used to calculate cross-correlations. The parameter to be extracted from cross-correlation data was not the shape of the decay from maximum, but the position of the peak of the cross-correlation. If the cross-correlation peaked at some $\tau \neq 0$, a time delay between flux at different energies within a shot would be indicated. The cross-correlation was thus defined:

$$\rho_u = \frac{R_u}{R_o} \tag{2}$$

$$R_u = \frac{1}{N-1-|u|} \sum_{\max(1,1+u)}^{\min(N,N+u)} (s_{i,LO} - \bar{s}_{LO})(s_{i-u,HI} - \bar{s}_{HI})$$

An autocorrelation is calculated if $s_{i,HI} = s_{i,LO}$, in which case $R_u = R_{-u}$. In the limit of large data set length N, and small bin size T such that $T/\tau_o << 1$, the autocorrelation (2) can be corrected for counting statistics to yield an unbiased estimate of the autocorrelation of the original signal. The correction for statistical noise in the u = 0 term is:

$$\rho_u' = \rho_u \left(\frac{R_o}{R_o - \langle s \rangle} \right) \tag{3}$$

The time-skewness function is calculated to estimate the function

$$TS(\tau) = \int_{\infty}^{\infty} [f(t)f^2(t-\tau) - f^2(t)f(t-\tau)]\, dt \tag{4}$$

where f is the instantaneous photon flux at the source. It is calculated in an unnormalized form:

$$TS(u) = \sum_{i=1+u}^{N} (s_i\, s_{i-u}^2 - s_i^2\, s_{i-u}) \tag{5}$$

The expected value of TS(u) can be calculated from the parameters of a shot-noise model. Since TS(u) is antisymmetric about u = 0, it can be useful in the determination of a sense of the time asymmetry of the shots.

If an exponential shot noise model is assumed, shot parameters λ, τ_o, h, and f (see Equation 7, Chapter 1) can be determined from the autocorrelation, mean counting rate, variance, and third moment of the observed signal.

III. THE PROGRAM SUPERCOR

The program SUPERCOR in its present configuration reads from punched cards a data set on which a correlation function is to be performed. Control parameters which determine the mode of correlation function to be calculated from the data set, input and output, etc., are also read from cards. We describe below the format of the input data and the program routings determined by them.

The first data card contains a number of flags which set the mode of the calculation, and control plotting and averaging functions (READ statement 32, FORMAT statement 202). KERNEL is a seven-digit random number to prime the random number generator. It is required if simulated data are to be generated. ICONV controls the mode of the correlation function. If ICONV = 1, the raw auto- or cross-correlation function of equation (2) is calculated and, if an autocorrelation, corrected for the counting statistical contribution to the zeroeth term by equation (3). ICONV = 2 orders the calculation of the "partially unbiased" autocorrelation of equation (1). Correction for counting statistics is done on the averaged autocorrelation only in the subroutine CORAVG. If ICONV = 3, an unnormalized time-skewness function [equation (4)] is calculated. ICONV = 4 calculates no correlation function and returns only the value M_3 of the third moment of the data set.

IWRT = 1 commands output of each input data point before and after correction for the mean. IPLOT, if set to 1, orders production of a plot of the correlation function for each individual data set. IPUNCH

has nothing to do with punched cards, but if set to 1 activates the subroutine CORAVG to average the correlation functions calculated for each data set input or generated by the program. CHNKEY is a linear array of length 7 used to assign data read from input channel J to the internal data location XSCAL(I, CHNKEY(J)). ISHOT, if set to 1, calls the calculation of the shot noise parameters λ, τ_o, h, and f.

The second data card (READ statement 33, FORMAT statement 501) contains the background level for each energy channel 1-5 of the internal data array XSCAL and an estimated correction factor ZETA used to calculate the unbiased autocorrelation (see Section VI).

A flag ITEST on the third card (FORMAT statement 200), if less than zero, calls for the generation of simulated data with shot noise parameters read from that card (READ statement 34, FORMAT statement 201) (see Section V). If ITEST $\geq$ 0, as will be the case for an input data card (READ statement 3, FORMAT statement 100), the third card is treated as the first in a series of input cards which supply counting rate data for temporal bins I = 1 to IMAX. The counting rates for each of the seven input data channels are added into the internal data set XSCAL so that counts from the J^{th} input data channel on card I are added into XSCAL(I, CHNKEY(J)). XSCAL(I,5) is defined as the sum of XSCAL(I,1-4). A blank card terminates the data set and sets IMAX to the number of data cards previously read. One card calling for the generation of a simulated data set is thus equivalent to a series of cards containing a real data set including a final blank card.

If a real data set has been read, the first card following the data set specifies the bin numbers JLO and JHI and a title to identify

plotted output (READ statement 35, FORMAT statement 108). XSCAL(I,JLO) and XSCAL(I,JHI) correspond to $s_{i,LO}$ and $s_{i,HI}$ of equations (1) and (2). If JLO = JHI, an autocorrelation or time-skewness calculation is performed on the data in XSCAL(1-IMAX, JLO). If JLO $\neq$ JHI and ICONV has been set to the appropriate value 2, a cross-correlation is performed between XSCAL(1-IMAX, JLO) and XSCAL(1-IMAX, JHI). Successive cards may specify new values of JLO and JHI to call another correlation function. A card with JLO = 0 calls the reading of a new data set, while JLO < 0 resets the program to read a new first card (FORMAT 202) but does not reset the data summed in CORAVG.

When artificial data have been generated, JLO and JHI are set internally and only one correlation function is calculated. JLO = 1, JHI = 2 if ICONV = 1, and JLO = JHI = 1 for ICONV $\geq$ 2. Artificial data generated in "LO" and "HI" channels are stored in XSCAL(1-IMAX, 1 and 2) respectively.

IV. THE AVERAGING SUBROUTINE CORAVG

Any estimate of the correlation function of a train of data from a single data set of binned counts is subject to errors from both shot and photon statistics. The method used to estimate the error of a correlation function was to break the data set into several smaller sets, and examine the variation of the correlation function as calculated for each of the smaller data sets. The long exposure on Cyg X-1 of flight 26.038 was thus broken into four 20.99 second data sets for analysis.

The subroutine CORAVG sums each correlation function calculated during the program to form means and errors of the mean for each point of the correlation function:

$$\bar{\rho}_u = \frac{1}{M} \sum_{i=1}^{M} \rho_{u,i}$$

$$\sigma_u = M^{-1/2} \left[\frac{1}{(M-1)} \sum_{i=1}^{M} (\rho_{u,i} - \rho_u)^2 \right]^{1/2} , \qquad (6)$$

where M correlation functions have been calculated from a like number of data sets and $\rho_{u,i}$ is the u^{th} term of the correlation function calculated from the i^{th} data set. The program allows $M \leq 10$. In its current configuration, CORAVG is useful only when a single correlation function is performed on a series of sets from the same data stream in a single running of the program. Plotting and punching of the average correlation function are controlled by internal subroutine variables IPUNCH and IPLOT, which are set by a DATA statement.

Autocorrelations are roughly corrected for statistical effects in the u = 0 term by applying equation (3). The variance R_0 and mean counting rate s used are averaged over the M data sets. Since all calculations of delay times are based on the ratio of terms ρ_u with $u \geq 1$, this correction is not critical as it is applied to all terms $u \neq 0$. Uncorrected autocorrelations requested by ICONV = 1 are corrected for counting statistics in the main program. They cannot be averaged by CORAVG, as the correction would then be applied twice.

V. THE DATA SIMULATION SUBROUTINE FAKEDT

It was felt useful to include a subroutine to simulate a signal consisting of random shots with a falling exponential shape. The data handling constraints of the rocket electronics are simulated in this subroutine. In particular, only one count per 160 μsec bin can be generated (see Appendix A).

The artificial data are summed into 0.1024 second bins, as were the real data analyzed in Chapter 1. The following input parameters characterize the artificial data stream: TAULO, TAUHI, TAUOTH are the decay time of a shot in the energy bands LO [to be summed into XSCAL(1-IMAX,1)], HI [XSCAL(1-IMAX,2)], and OTH(er), which is used only for its anti-coincidence effects on LO and HI. Shots appear in the three energy bands with a peak counting rate HLO, HHI, and HOTH counts sec^{-1}. The shots occur on top of a constant flux per band CLO, CHI, and COTH counts sec^{-1}. A constant background rate BACKGD in a band outside LO, HI, and OTH is also significant only for its anti-coincidence effects. Shots occur at a random rate LAMBDA sec^{-1}. The leading edge of a shot in the HI band lags the start of the same shot in the LO and OTH bands by DT seconds. NFAKE determines the number of 0.1024 second bins of artificial data to be generated. The KERNEL input to the random number generator is regenerated each time it is used, so only one value must be input at the start of the program.

VI. CALCULATION OF EXPONENTIAL SHOT PARAMETERS (ISHOT = 1)

SWK show that, for an assumed exponential shot signal characterized by λ shots sec^{-1} of peak flux h counts sec^{-1}, falling exponentially from the peak with decay time τ_o sec and comprising a fraction f of the time-averaged flux, all four shot parameters can be recovered by analysis of the data stream.

The shot decay time τ_o is determined by a least squares fit of the auto-correlation defined by equation (1) to the form of equation (2), Chapter 1. This least squares fit is performed in the subroutine MKWFIT. The intrinsic mean rate s, variance V_s, and third moment M_{3s} of the counting rate can be used to calculate the other three shot parameters (see equation (7), Chapter 1). However, the measured moments of the data must first be corrected for experimental effects.

The measured moments of the counting rate are defined:

$$\langle S \rangle = \frac{1}{N} \sum_{i=1}^{N} s_i$$

$$V = \frac{1}{N} \sum_{i=1}^{N} (s - \langle s \rangle)^2 \qquad (7)$$

$$M_3 = \frac{1}{N} \sum_{i=1}^{N} (s - \langle s \rangle)^3 .$$

These measured moments can be biased by the effects of finite bin width, counting statistics, and finite data train length (SWK). For bin width 0.1 second and characteristic shot decay time 1 second, binning effects

are not important. The average counting rate $\langle s \rangle$ is not biased by the latter two effects. V and M_3 may be corrected for counting statistics in a straightforward manner:

$$V_s = V - \langle s \rangle$$

$$M_{3s} = M_3 - 3V_s - \langle s \rangle \qquad \text{(SWK)}. \tag{8}$$

The variance V has a bias due to correlations in the shot process which cannot be removed without the assumption of a specific shot model. Fortunately, the correction term is small for the data sets analyzed herein. The correction term ξ (zeta) defined by SWK such that $V_{corrected} = (\frac{N}{N-1}) \frac{1}{1-\xi} R_0$ can be calculated as a function of τ_o if we assume exponential shots. For $\tau_o = 1$ sec, ξ is of order 5%, so that it was included as a fixed correction factor ZETA into the program. The scatter in determination of M_3 from data set to data set was so large that data set length corrections were negligible.

The shot parameters λ, τ_o, h, and f were calculated separately for each data set. Values from the several data sets can be read from the printout and averaged to determine the mean and error of each parameter. No provision exists in the program to do this averaging.

Exhibit 1

The Program SUPERCOR

```
C 'SUPERCOR' IS A PROGRAM TO DO AUTO- AND CROSS-CORRELATIONS OF CYG X-1.
C DELAY TAU IS IN UNITS OF 0.1024 S.  TAU>0 IMPLIES THAT THE LOW ENERGY DATA
C LAGS HIGH ENERGY DATA.  DATA IS IN XSCAL(820,5)= (TIME; 1=0.6-1.5 KV,
C 2=1.5-3.0 KV, 3=3.0-6.0 KV, 4=>6.0 KV, 5=>3.0 KV.)
      INTEGER COUNTS(7)
      INTEGER CHNKEY(7),O
      REAL M3,M3S,LAMTAU,LAM,LAMBDA
      DIMENSION XMEAN(5),XSCAL(820,5),TITLE(6),XLO(820),XHI(820)
      DIMENSION R(201),BCKD(5),RIN(48)
      EQUIVALENCE (R(102),RIN(1))
      EQUIVALENCE (XSCAL(1,1),XLO(1)), (XSCAL(1,2),XHI(1))
      CALL REREAD(5)
   32 READ (5,202) KERNEL,ICONV,IWRT,IPLOT,IPUNCH,CHNKEY,ISHOT
  202 FORMAT (I2,12I2)
      WRITE (6,299) KERNEL,ICONV,IWRT,IPLOT,IPUNCH,CHNKEY,ISHOT
  299 FORMAT (' KERNEL=',I2,' ICONV=',I2,' IWRT=',I2,' IPLOT=',I2,
     * ' IPUNCH=',I2,' CHNKEY=',7I2,' ISHOT=',I2)
   33 READ (5,501) BCKD, ZETA
      WRITE (6,501) BCKD,ZETA
  501 FORMAT (6F10.3)
C IWRT=1  WRITE INPUT DATA, XSCAL
C ICONV= 0 BRINKMAN NORM; ICONV=1 BP NORM
C ICONV=2 WEISSKOPF (1977) NORM
C ICONV=3 CALCULATE TIME-SKEWNESS=
C           1/N* SUM OF (X(T)*X(T-TAU)**2-X(T)**2*X(T-TAU))
C ICONV=4 CALCULATE M3 ONLY.  IPLOT, IPUNCH ARE AUTOMATICALLY 0.
C IPLOT=0 NO PLOTS
C IPUNCH=1 AVERAGE ALL CORRELATION FUNCTIONS AT END OF PROGRAM.
C ISHOT=1 CALCULATE SHOT-NOISE PARAMS FOR EACH DATA SET.  USE ICONV=2.
C      DATA FOR BCKD, ZETA MUST BE ENTERED (OTHERWISE THEY ARE NOT USED.)
   13 DO 14 I=1,820
      DO 14 J=1,5
   14 XSCAL(I,J)=0.
      I=1
      READ (5,200,END=99) ITEST
  200 FORMAT (I6)
      CALL XBACK
      IF (ITEST.GE.0) GO TO 3
   34 READ (5,201) TAULO,TAUHI,TAUOTH,HLO,HHI,HOTH,CLO,CHI,COTH,BACKGD,
     * LAMBDA,DT,NFAKE
      CALL          FAKEDT(TAULO,TAUHI,TAUOTH,HLO,HHI,HOTH,CLO,CHI,COTH,
     * BACKGD,LAMBDA,DT,NFAKE,XLO,XHI,KERNEL)
  201 FORMAT (10X,12F5.2,I5)
      IMAX=NFAKE
      GO TO 30
    3 READ (5,100) COUNTS
  100 FORMAT (6X,7I4)
      IF (COUNTS(3).EQ.0.AND.COUNTS(4).EQ.0) GO TO 1
      DO 2 J=1,7
    2 XSCAL(I,CHNKEY(J))= XSCAL(I,CHNKEY(J))+ COUNTS(J)
      XSCAL(I,5)= XSCAL(I,4)+ XSCAL(I,3) +XSCAL(I,2)+ XSCAL(I,1)
      I=I+1
      GO TO 3
    1 IMAX=I-1
   30 WRITE (6,101) IMAX
  101 FORMAT (' NO OF BINS=',I4)
      DO 6 J=1,5
      XMEAN(J)=0.
      DO 7 I=1,IMAX
    7 XMEAN(J)= XMEAN(J)+ XSCAL(I,J)
      XMEAN(J)= XMEAN(J)/IMAX
    6 WRITE (6,104) J,XMEAN(J)
  104 FORMAT (' J=',I3,' XMEAN(J)=',F12.5)
```

```
      DO 4 I=1,IMAX
      IF (IWRT.GT.C)
     *WRITE (6,102) (XSCAL(I,J),J=1,5)
  102 FORMAT (1X,5F10.4)
  103 FORMAT (6X,5F10.4)
      DO 5 J=1,5
      XSQRT=SQRT(XSCAL(I,J))
      IF (XSQRT.LT.C.5) XSQRT=1.
      IF (ICONV.GE.1) XSQRT=1.
    5 XSCAL(I,J)= (XSCAL(I,J)-XMEAN(J))/XSQRT
      IF (IWRT.GT.0)
     *WRITE (6,103) (XSCAL(I,J),J=1,5)
    4 CONTINUE
   12 JLO=1
      JHI=2
   35 IF (ITEST.GE.0) READ (5,108,END=99) JLO,JHI,TITLE
      IF (ITEST.GE.0) GO TO 21
      IF (ICONV.GE.2) JHI=1
      CALL OUTCOR(TITLE,NCLT)
      WRITE (6,203) TAULO,TAUHI
  203 FORMAT ('TAU=',F4.1,' S',2X,'TAU=',F4.1,' S  ')
      CALL OUTCOR
   21 WRITE (6,105) JLO,JHI,TITLE
      IF (JLO.EQ.-1) GO TO 32
      IF (JLO.EQ.0) GO TO 12
  108 FORMAT (2I2,6A4)
  105 FORMAT (//' JLO=',I2,' JHI=',I2,2X,6A4)
      M3=0.
      DO 31 IM3=1,IMAX
   31 M3= M3+ XSCAL(IM3,JLO)**3
      M3=M3/IMAX
      WRITE (6,301) M3
  301 FORMAT (' M3= ',E14.8)
      IF (ICONV.EQ.4) GO TO 22
      DO 8 KRCOT=53,149
      K=KRCOT-101
      R(KRCOT)=0.
      IF (JLO.EQ.JHI.AND.K.LT.0.AND.ICONV.NE.3) GO TO 10
      NORM=IMAX-1-IABS(K)
      IF (ICONV.GE.2) NORM=IMAX
      ILOWER=1+K
      IF (K.LT.0) ILOWER=1
      IUPPER=IMAX+K
      IF (K.GE.0) IUPPER=IMAX
      IF (ICONV.NE.3) GO TO 1234
C CALCULATE TIME-SKEWNESS
      DO 20 I=ILOWER,IUPPER
   20 R(KROOT)= R(KROOT)+ XSCAL(I,JLO)*XSCAL(I-K,JLO)**2-
     * XSCAL(I,JLO)**2*XSCAL(I-K,JLO)
      GO TO 19
 1234 DO 9 I=ILOWER,IUPPER
    9 R(KROOT)= R(KROOT)+ XSCAL(I,JLO)* XSCAL(I-K,JHI)
   19 R(KROOT)= R(KROOT)/NORM
   10 CONTINUE
    8 CONTINUE
      IF (ICONV.NE.2) GO TO 17
      DO 18 K=102,149
      U=K-101
   18 R(K)= R(K)+ (IMAX-U)*R(101)/(IMAX-1)/IMAX
   17 XNORM=R(101)
      IF (ICONV.EQ.3) XNORM=2000.
      WRITE (6,106) XNORM
  106 FORMAT (' NORMALIZED R(TAU=0)=',F12.5)
```

```
      DO 11 K=53,149
   11 R(K)= R(K)/XNORM
C CORRECT AUTO-CORRELATIONS FOR POISSON NOISE IN ZERO TERM.
      IF (JLO.NE.JHI) GO TO 15
      IF (ICONV.GE.2) GO TO 15
      CORR=XNORM/(XNORM-XMEAN(JLO))
      WRITE (6,402) CORR
  402 FORMAT (' CORR=',F10.5)
      DO 16 K=102,149
   16 R(K)= R(K)*CORR
   15 CONTINUE
      WRITE (6,107) R
  107 FORMAT (1X,10F10.5)
      IF (ISHOT.EQ.0) GO TO 2346
      CALL MKWFIT (PIN,IMAX,20,X,TAU)
      XMEANO= XMEAN(JLO)-BCKD(JLO)
      VS= XNORM*(IMAX/(IMAX-1.0))*(1./(1.-ZETA))-XMEAN(JLO)
      M3S= M3- 3.*VS- XMEAN(JLO)
      HT23= M3S/VS
      HT= 1.5*HT23
      H= HT/0.1024
      LAMTAU= 2.*VS/HT**2
      CT= XMEAN(JLO)-HT*LAMTAU
      CTO =CT-BCKD(JLO)
      F=1.-CTO/XMEANO
      HTAU=H*TAU
      LAM=LAMTAU/TAU
      WRITE (6,502) XNORM,XMEAN(JLO),XMEANO,VS,M3,M3S,HT,LAMTAU,CT,CTO,
     1 F,HTAU,LAM,TAU
  502 FORMAT ('    RO      XMEAN   XMEANO     VS       M3       M3S      HT
     1LAMTAU     CT       CTO       F      HTAU    LAMBDA     TAU'/' ',14F8.3)
 2346 IF (IPLNCH.EQ.0) GO TO 2345
      CALL CORAVG (JLO,JHI,XMEAN(JLO),XNORM,TITLE,R)
 2345 IF (IPLOT.EQ.0) GO TO 22
      CALL BOX (JLO,JHI,TITLE,R)
   22 IF (ITEST.LT.0) GO TO 13
      GO TO 12
   99 IF (IPLNCH.NE.0) CALL PLOTUP
      STOP
      END
      SUBROUTINE BOX (ILO,IHI,TITLE,R)
      DIMENSION TITLE(6),R(201)
      Z=2
      IF (ILO.EQ.IHI) Z=1
      CALL VLABEL (0.,0.,-Z,Z, 10.,10,'RHO',3,1,'(F4.1)',4)
      CALL VLABEL( 0.,5.,-100.,100.,10.,10,'TAU (0.1024 S)',14,0,'(F5.0)
     *',4)
      IF (ILO.EQ.IHI) GO TO 1
      CALL SYSSYM (7.5,9.,0.14,'CROSS-CORRELATION',17,0.)
      CALL SYSSYM (7.5,8.8,0.14,'LO CHANNEL=',11,0.)
      CALL SYSSYM (9.0,8.8,0.14,TITLE(1),12,0.)
      CALL SYSSYM(7.5,8.6,0.14,'HI CHANNEL=',11,0.)
      CALL SYSSYM (9.0,8.6,0.14,TITLE(4),12,0.)
      CALL SYSSYM (7.5,8.4,0.14,'TAU>0= LO CHANNEL LAGS',22,0.)
      GO TO 2
    1 CALL SYSSYM (7.5,9.0,0.14,'AUTOCORRELATION',15,0.)
      CALL SYSSYM (8.0,8.8,0.14,TITLE(1),12,0.)
      CALL SYSSYM (8.0,8.6,0.14,TITLE(4),12,0.)
    2 CALL SYSPLT (-0.025,5.,3)
      DO 3 I=1,201
      X=5.+ (I-101)/20.
      X1= X-0.025
      X2= X+0.025
```

```
      Y= (5./Z)*R(I)+5.
      CALL SYSPLT(X1,Y,2)
      CALL SYSPLT (X2,Y,2)
    3 CONTINUE
      CALL SYSEND(1,1)
      RETURN
      END
       SUBROUTINE FAKEDT(TAULO,TAUHI,TAUOTH,HLO,HHI,HOTH,CLO,CHI,COTH,
     * BACKGD,LAMBDA,DT,NBINS,XLO,XHI,KERNEL)
C       THIS IS A SUBROUTINE TO SIMULATE DATA OF EXPONENTIAL SHOT PULSES--
C       DESIGNED TO BE A SUBROUTINE OF SUPERCOR.
C       SHOT CHARACTERISTICS:
C TAULO AND TAUHI= EXPONENTIAL DECAY TIME OF PULSES IN LO AND HI ENERGY
C       CHANNELS.
C HLO AND HHI= PEAK COUNTING RATE (COUNTS/SEC) AT MAXIMUM OF SHOT.
C CLO,CHI= CONSTANT COUNTING RATE IN LO AND HI CHANNELS.
C BACKGD= CONSTANT COUNTING RATE (/SECOND) IN OTHER ENERGY CHANNELS.
C LAMBDA= SHOT RATE /SEC.
C DT= DELAY BY WHICH HI ENERGY SHOT FOLLOWS LOW ENERGY SHOT.
C NBINS= NUMBER OF BINS (0.1024 S) OF ARTIFICIAL DATA TO GENERATE.
C NLO,NHI(10000)= ARRAYS FOR ARTIFICIALLY GENERATED DATA.
C KERNEL= KERNEL FOR RANDOM NUMBER GENERATOR.
C
C ISW(1-6) CONTROL DIAGNOSTIC PRINTOUTS.
C       ISW(1)=1 WRITE ALL PARAMETERS.
C       ISW(2)=1 WRITE JSHOT(1-JMAX)
C ISW(3)=1 WRITEHI
C ISW(3)=1 WRITE HLO,HHI,PTOT FOR FIRST 100 SMALL BINS
C ISW(4)=1 WRITE NLO(K),NHI(K) FOR FIRST 100 SMALL BINS
C ISW(5)=1 WRITE NLO,NHI(1-NBINS)
C SMALL BINS ARE 0.01024 S = 64*0.00016) S.
      REAL LAMBDA
      DIMENSION XLO(    1),XHI(    1),JSHOT(20000),ISW(6)
      DATA ISW/1,1,0,0,1,0/
      P= 0.01024*LAMBDA
      IP=0.2147484810*P
      NT=DT/0.01024
      XTAUHI=TAUHI/0.01024
      XTAULO=TAULO/0.01024
      XTAUO=TAUOTH/0.01024
      BBACK=BACKGD*0.000160
      NSBINS=10*NBINS
C NSBINS= NUMBER OF 0.01024 S BINS
C NSBINS= NUMBER OF 0.000160 S BINS.
      DO 1 I=1,20000
    1 JSHOT(I)=0
      J=0
      TAUMX= AMAX1(TAULO,TAUHI)
      NPRE=10*TAUMX/0.01024
      IF (ISW(1).NE.0)
     * WRITE (6,101) TAULO,TAUHI,HLO,HHI,CLO,CHI,BACKGD,LAMBDA,DT,P,
     * XTAULO,XTAUHI,BBACK,TAUMX,NBINS,KERNEL,IP,NT,NSBINS,NPRE
     * ,TAUOTH,HOTH,COTH,XTAUO
  101 FORMAT (' TAULO=',F6.2,' TAUHI=',F6.2,' HLO=',F7.1,  ' HHI=',F7.1,
     1 ' CLO=',F7.1,' CHI=',F7.1,' BACKGD=',F7.1/' LAMBDA=',F6.2,' DT=',
     2 F8.4,' P=',F8.4,  ' XTAULO=',F8.2,' XTAUHI=',F8.2,' BBACK=',F8.4,
     3 ' TAUMX=',F6.2/' NBINS=',I4,' KERNEL=',I10,' IP=',I10,' NT=',I6,
     4 ' NSBINS=', I6,' NPRE=',I8/' TAUOTH=',F6.2,' HOTH=',F7.1,' COTH='
     5 ,F7.1,' XTAUO=',F6.2)
      DO 3 I=1,NPRE
      KERNEL= NRAND(KERNEL)
      IF (KERNEL.GT.IP) GO TO 3
      J=J+1
```

```
      JSHOT(J)= I-NPRE
    3 CONTINUE
      DO 2 I=1,NSBINS
      KERNEL=NRAND(KERNEL)
      IF (KERNEL.GT.IP) GO TO 2
      J=J+1
      JSHOT(J)=I
    2 CONTINUE
      JMAX=J
C JSHOT(1-JMAX)= SMALL BIN NOS. OF START OF SHOTS.
C NOTE APPROXIMATION THAT ONLY ONE SHOT IS ALLOWED TO START IN EACH
C 0.000160 S BIN.
      JMIN=1
      IF (ISW(2).NE.0)
     *WRITE (6,102) (JSHOT(I),I=1,JMAX)
  102 FORMAT (15I8)
      DO 6 K=1,NBINS
      IMAX=10*K
      IMIN=IMAX-9
      XLO(K)=0.
      XHI(K)=0.
      DO 6 I=IMIN,IMAX
      RHI=CHI/6250.
      RLO=CLO/6250.
      ROTHER= COTH/6250.
      IF (ISW(4).NE.0.AND.I.LE.101)
     * WRITE (6,104) K,XLO(K),XHI(K)
  104 FORMAT (I4,2F6.0)
      DO 7 J =JMIN,JMAX
      IF ((I-JSHOT(J)).GT.NPRE) GO TO 8
      IF (I.LT.JSHOT(J)) GO TO 9
      RLO=RLO +HLO/6250.*EXP((JSHOT(J)-I)/XTALLO)
      ROTHER= ROTHER+ HOTH/6250.* EXP((JSHOT(J)-I)/XTAUO)
      IF (I.LT.(JSHOT(J)+NT)) GO TO 7
      RHI= RHI+ HHI/625C. *EXP((JSHOT(J)+NT-I)/XTAUHI)
      GO TO 7
    8 JMIN=J+1
    7 CONTINUE
    9 CONTINUE
C RLO,RHI ARE AVERAGE NUMBER OF COUNTS IN A 0.CC0160 S BIN IN EACH ENERGY
      RTOT=RLC+RHI+RBACK+ROTHER
      IF (I.LE.100.AND.ISW(3).NE.0)
     * WRITE (6,103) RLO,RHI,ROTHER,RTOT
  103 FORMAT (4F10.5)
      LP=0.2147484E10*EXP(-RTOT)
      MP=RLC/RTOT* 0.2147484E10
      NP= (RLC+RHI)/RTOT* 0.2147484E10
C IF (KERNEL.LE.NP) THERE ARE NO COUNTS IN THE SMALL (0.00016C S) BIN.
C       OTHERWISE, THERE ARE ONE OR MORE COUNTS, ONE OF WHICH IS
C       ANALYZED.
      MLC=0
      MHI=0
      DO 12 M=1,64
      KERNEL=NRAND(KERNEL)
      IF (KERNEL.LE.LP) GO TO 12
      KERNEL=NRAND(KERNEL)
      IF (KERNEL.GT.NP) GO TO 12
      IF (KERNEL.GT.MP) GO TO 13
      MLO=MLO+1
      GO TO 12
   13 MHI=MHI+1
   12 CONTINUE
      XLC(K)= XLO(K)+MLC
```

```
      XHI(K)= XHI(K)+WHI
    6 CONTINUE
      IF (ISW(5).EQ.0) RETURN
      WRITE (6,105) (XLO(I),I=1,NBINS)
      WRITE (6,105) (XHI(I),I=1,NBINS)
  105 FORMAT (24F5.0)
      RETURN
      END
      SUBROUTINE CORAVG (JLO,JHI,XMEAN,XNORM,TITLE,RIN)
      DIMENSION R(97,12),RATE(11),VAR(11),TITLE(6),RIN(201)
      DATA I,IPLOT,IPUNCH/0,1,0/
C MODE=2= CROSS-CORRELATION, MODE=1= AUTO/CORRELATION.
      I=I+1
      RATE(I)= XMEAN
      VAR(I)= XNORM
      DO 2 J=1,97
    2 R(J,I)= RIN(J+52)
      RETURN
      ENTRY PLOTUP
      IMAX=I
      MODE=1
      IF (JLO.NE.JHI) MODE=2
      DO 4 I=1,97
      DO 4 K=11,12
    4 R(I,K)=0.
      RATE(11)=0.
      VAR(11)=0.
      DO 3 I=1,IMAX
      RATE(11)=RATE(11)+ RATE(I)
      VAR(11)= VAR(11)+VAR(I)
      DO 3 J=1,97
    3 R(J,11)= R(J,11)+ R(J,I)
      RATE(11)= RATE(11)/IMAX
      VAR(11)= VAR(11)/IMAX
      DO14 J=1,97
   14 R(J,11)= R(J,11)/IMAX
      DO 6 J=1,97
      DO 5 I=1,IMAX
    5 R(J,12)= R(J,12)+ (R(J,I)-R(J,11))**2
      R(J,12)= R(J,12)/(IMAX-1)
      R(J,12)= SQRT(R(J,12))
      X=IMAX
    6 R(J,12)= R(J,12)/SQRT(X)
      CORR= VAR(11)/(VAR(11)-RATE(11))
      IF (MODE.GE.2) GO TO 7777
       DO 7 J=1,97
       DO 7 K=11,12
    7 R(J,K)=R(J,K)*CORR
 7777 CONTINUE
      WRITE (6,102) TITLE,VAR(11),RATE(11),CORR
      JMIN=1
      IF (MODE.NE.2) JMIN=50
      DO 11 I=JMIN,97
      ITAU=I-49
   11 WRITE (6,103) ITAU,R(I,11),R(I,12)
  102 FORMAT (1X,6A4,' MEAN VAR=',F12.5 ,' MEAN RATE=',F12.5,' CORR=',
     1 F12.5)
  103 FORMAT (I5,2F10.5)
      IF (IPUNCH.NE.1) GO TO 4321
      WRITE (7,301) (R(I,11),I=JMIN,97),(R(I,12),I=JMIN,97)
  301 FORMAT (16F5.3)
 4321 IF (IPLOT.NE.1) GO TO 8
      CALL VLABEL (0.,0.,-0.4,1.,3.5,7,'RHO',3,1,'(F4.2)',4)
```

```
      CALL VLABEL (0.,0.,-50.,50.,10.,10,'TAU',3,0,'(F4.0)',3)
      DO 9 I=JMIN,97
      ITAU=I-49
      X=0.1*ITAU +5.0
      X1=X-0.05
      X2=X+0.05
      Y=1.0+ 2.5*R(I,11)
      DY=2.5*R(I,12)
      CALL SYSPLT (X,Y-DY,3)
      CALL SYSPLT (X,Y+DY,2)
      CALL SYSPLT (X1,Y,3)
      CALL SYSPLT (X2,Y,2)
    9 CONTINUE
      CALL SYSEND (1,1)
    8 RETURN
      END
      SUBROUTINE MKWFIT(R,N,UMAX,X,TAU)
C THIS IS A PROGRAM TO REDUCE PARTIALLY UNBIASED AUTOCORRELATION PER
C WEISSKOPF (1977) TO CALCULATE CHISQ FIT TO PREDICTED FUNCTION OF TIME LAG.
      INTEGER U,UMAX
      REAL R(48),RERR(48),PRED(48)
      DATA XO,DX,IWRT,RERR/0.02,0.005,0,48*0.1/
      REAL CHI(3)
      IEND=0
      X=XO-DX
      DO 8 I=1,3
    8 CHI(I)=10000.
    1 X=X+DX
    5 DO 2 U=1,UMAX
      CALL F(U,N,X,PREDCT)
      PRED(U)=PREDCT
    2 IF (U.NE.1) PRED(U)= PRED(U)/PRED(1)
      PRED(1)=1.
      SUM1=0.
      SUM2=0.
      SUM3=0.
      DO 3 U=1,UMAX
      SUM1=SUM1+ R(U)**2/RERR(U)**2
      SUM2=SUM2+ R(U)*PRED(U)/RERR(U)**2
    3 SUM3=SUM3+ PRED(U)**2/RERR(U)**2
      ALPHA=SUM2/SUM3
      CHISQ=SUM1-ALPHA*SUM2
      IF (IWRT.EQ.1.OR.IEND.EQ.1)
     *WRITE (6,204) X,CHISQ,ALPHA
  204 FORMAT (3F10.4)
      IF (IEND.EQ.1) GO TO 6
      CHI(1)=CHI(2)
      CHI(2)=CHI(3)
      CHI(3)=CHISQ
      IF (CHI(2).GE.CHI(3)) GO TO 1
      X=X-DX
      Z= -(CHI(3)-CHI(1))/2/(CHI(1)+CHI(3)-2*CHI(2))
      X=X+DX*Z
      TAU= 0.1024/X
      IEND=1
      GO TO 5
    6 IF (IWRT.NE.1.OR.J.NE.1) GO TO 7
      DO 4 U=1,UMAX
      PRED(U)= PRED(U)*ALPHA
      C= (R(U)-PRED(U))**2/RERR(U)**2
    4 WRITE (6,105) U,R(U),RERR(U),PRED(U),C
  105 FORMAT (I5,4F10.4)
    7 RETURN
```

```
END
SUBROUTINE F(U,N,X,PRED)
INTEGER U
EEX=EXP(-X)
G=1.-EEX
TERM3= (U-(1.-EEX**U)/G)/N/(N-U)
TERM2= -(1.+(N-U)/(N-1)/N)*(1.-1./N/G)/(N-U)
TERM1= EEX**(U-1)*G/2.
PRED=( TERM1+TERM2+TERM3)*(N-U)/N
RETURN
END
```